Chapter 2

Optical modes of dielectric spheres (Microsphere Resonators)

2.1 Introduction

The modes of a spherical dielectric particle were first investigated by Mie at the beginning of the 19^{th} century, in the context of light scattering from spherical particles. The scattering spectrum exhibited sharp features, which can be attributed to resonant circulation of optical energy within the sphere. These optical modes are confined by continuous total internal reflection at the dielectric air interface and are often referred to as 'whispering-gallery modes'. This description originated from the "problem of the whispering-gallery" which Lord Rayleigh published in 1912[35], describing the phenomenon of acoustical waves he had observed propagating around the interior gallery of the Saint Paul's Cathedral[1]. In the following sections, the resonant characteristics of spherical dielectric particles (silica microspheres), such as their field distribution, mode volume, radiation loss etc. are discussed and serve as an introduction to the terminology which is used throughout this thesis. Approximate formulas for the free-spectral range and whispering-gallery loss for the experimentally relevant wavelength and size range are given.

[1]Some author have also referred to these modes as "morphology dependent resonances" (MDRs), however this terminology has not been widely adopted.

2.2 Optical modes of a dielectric sphere

The optical modes of a spherical dielectric particle can be calculated by solving Helmholtz equation in spherical coordinates[2], which has been treated by several authors (in particular see reference [36] for a comprehensive overview). A significant simplification occurs if the sphere consists of a homogeneous dielectric, and if the optical modes reflect with grazing incidence upon the dielectric-air boundary, such that the polarization can be assumed to be constant along the optical trajectories. Under this assumption the optical modes can be solved by the scalar wave equation approximation and solutions fall into two classes, and are either electric in character (TM-case) or magnetic in character (TE-case). The field components can be expressed in terms of a single field components (E_ϕ for the TM-case or H_ϕ for the TE-case) and solutions are found by solving the scalar wave equation for either the E_ϕ or H_ϕ alone by the separation of variables approach, i.e. $E_\phi$or $H_\phi = \psi(\phi, \theta, r) = \psi_\phi(\phi)\psi_\theta(\theta)\psi_r(r)$. TE modes possess an electric field is parallel to the surface of the sphere (i.e. $E_\phi = E_r = 0$, i.e. $\vec{E}||\overrightarrow{\theta}$),whereas the TM modes possess a magnetic field which is parallel to the surface of the sphere, i.e. (i.e. $H_\phi = H_r = 0$, i.e.$\vec{H}||\overrightarrow{\theta}$). As a result, the electric field distribution of TM modes is predominantly radial in character. The introduced eigenfunctions for the radial, azimuthal and polar fields can be associated with the radial mode number (n), the polar mode number (ℓ) and the azimuthal mode number (m) as well as the polarization (p). The azimuthal eigenfunctions are given by[3]:

$$\psi_\phi = \frac{1}{\sqrt{2\pi}} \exp(\pm im\phi) \tag{2.1}$$

By introducing the polar mode number ℓ, the equation for ψ_θ is given by:

$$\frac{1}{\cos(\theta)} \frac{d}{d\theta} \left(\cos(\theta) \frac{d}{d\theta} \psi_\theta \right) - \frac{m^2}{\cos(\theta)^2} \psi_\theta + \ell(\ell+1)\psi_\theta = 0 \tag{2.2}$$

[2]Helmholtz equation $\left(\nabla^2 - k^2 n^2\right)\psi = 0$ in spherical coordinates is given by: $\frac{1}{r^2}\frac{\partial^2}{\partial r^2}(r\psi) + \frac{1}{r\sin(\theta)}\frac{\partial}{\partial r}\left(\sin(\theta)\frac{\partial}{\partial\theta}\psi\right) + \frac{1}{r^2\sin^2(\theta)}\frac{\partial^2}{\partial\phi^2}\psi - n^2k^2\psi = 0$

[3]The separation of variables approach leads to the introduction of the azimuthal and angular mode number, $\frac{1}{\psi_\phi}\frac{d^2}{d\phi^2}\psi_\phi = const \equiv -m^2$ and $\frac{r}{\psi_r}\frac{d^2}{dr^2}(r\psi_r) = const \equiv \ell(\ell+1)$.

And finally the radial field ψ_r has to obey:

$$\frac{d^2}{dr^2}\psi_r + \frac{2}{r}\frac{d}{dr}\psi_r + \left(k^2 n(r)^2 - \frac{\ell(\ell+1)}{r^2}\right)\psi_r = 0 \tag{2.3}$$

The last two equations possess analytical solutions in terms of the generalized Legendre Polynomials $P_m^\ell(\cos\theta)$ (which are commonly re-expressed as the spherical Harmonics $Y_m^\ell(\theta)$) and the Bessel functions $j_\ell(kr)$. For each polar mode number ℓ, the allowed azimuthal mode numbers are in the range of $-\ell < m < \ell$, leading to a $2\ell+1$ degeneracy of the azimuthal modes.

2.3 Intensity distribution for a microsphere WGM

The field distribution and the resonance locations are determined by matching the solutions interior and exterior to the sphere at the dielectric-air boundary[37], leading to a characteristic equation. For a microsphere this requires matching the Bessel function $j_l(ka)$ and the outgoing Hankel functions $h_l(ka)$ at the dielectric boundary. The characteristic equation for this case is given by:

$$x \cdot \frac{j_l'(ka)}{j_l(ka)} = \frac{h_l'(ka)}{h_l(ka)} \quad \text{where} \quad x = \begin{bmatrix} \frac{1}{m} \text{ for TM} \\ m \text{ for TE} \end{bmatrix} \tag{2.4}$$

The latter equation depends only on the angular mode number ℓ (reflecting the aforementioned $2\ell+1$ degeneracy, with respect to the azimuthal mode number m). Figure 2.1 shows the solution to the radial equation for the first three radial mode numbers. The radial mode number gives the number of field maxima. Outside the microsphere the fields decays exponentially (where the decay length increases as a function of the radial mode number n). The complete intensity profile of the $E_\phi-$component (i.e. TM polarization) in the (r,θ) plane is given in figure 2.2 for a microsphere of 25-μm-diameter, and was obtained by numerical modeling using a finite element PDE-eigenmode solver package (see Appendix B). The field outside the microsphere is evanescent and exhibits exponential decay which is slower for higher

order radial mode numbers.

2.4 Asymptotic solutions

A very useful formula is given in reference [38] where the approximate resonance locations are derived by asymptotic expansion of the characteristics equation in powers of $\ell^{-1/3}$. The first 4 terms in the expansion are given by:

$$\omega_{nm\ell p} = \frac{c}{n_a R}\left[\frac{\ell+\frac{1}{2}}{m} - \frac{t_n^0}{m}\left(\frac{\ell+\frac{1}{2}}{2}\right)^{1/3} + \frac{-p}{\sqrt{m^2-1}} + \left(\frac{\ell+\frac{1}{2}}{2}\right)^{-1/3}\frac{(t_n^0)^2}{20m} + O\left(\frac{\ell+\frac{1}{2}}{2}\right)^{-2/3}\right] \tag{2.5}$$

In this equation m is the relative index of refraction $m = n_a/n_s$ (n_a index of the medium outside the sphere), ℓ is the angular mode number, t_n^0 is the nth zero of the Airy function $Ai(-t_n^0) = 0$ (and corresponds to the n^{th}-order Radial mode) and p is a coefficient related to the polarization given by:

$$p = \begin{Bmatrix} 1 & \text{TE} \\ 1/m^2 & \text{TM} \end{Bmatrix}$$

The expansion can be used to relate the polar mode number ℓ to the experimentally measured free-spectral range of the cavity. The latter is defined as the distance between successive azimuthal mode numbers and is given by the expression:

$$\Delta\omega_{FSR} \equiv |\omega_{nm\ell} - \omega_{nm\ell+1}| \underset{\ell\gg 1}{\approx} \frac{c}{n_a R}\left(\frac{1}{m} - t_n^0\frac{\ell^{-2/3}}{3}\right) \tag{2.6}$$

For the microspheres considered in this thesis, the resonance wavelength is located in the 1550-nm telecommunication band and the corresponding free-spectral-range as a function of mode number is shown in 2.3 for a fundamental WGM ($n = 1, \ell = m$).

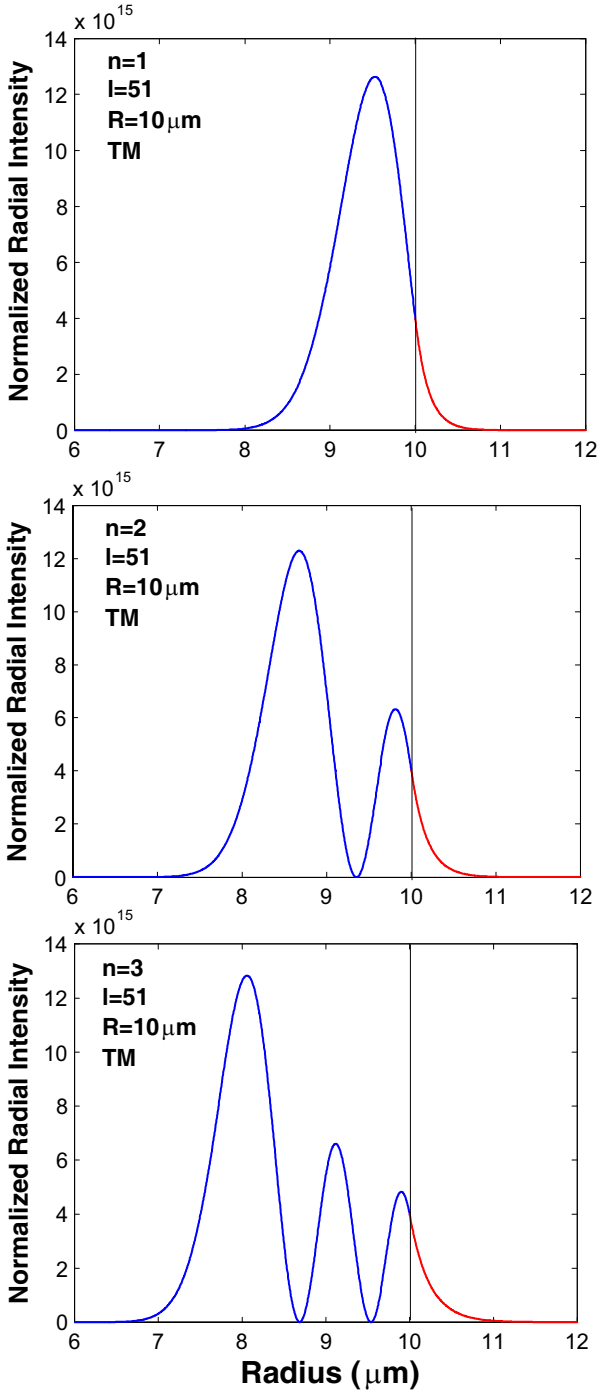

Figure 2.1: Calculated intensity distribution $|E_\phi|^2$ in the radial direction for a microsphere with principal radius 10 μm and angular mode number $\ell = 51$ ($\lambda \approx 1550$ nm) for the first three radial mode numbers ($n = 1, 2, 3$). The evanescent field is color coded in red, and exhibits a slower decay for higher order radial numbers (n).

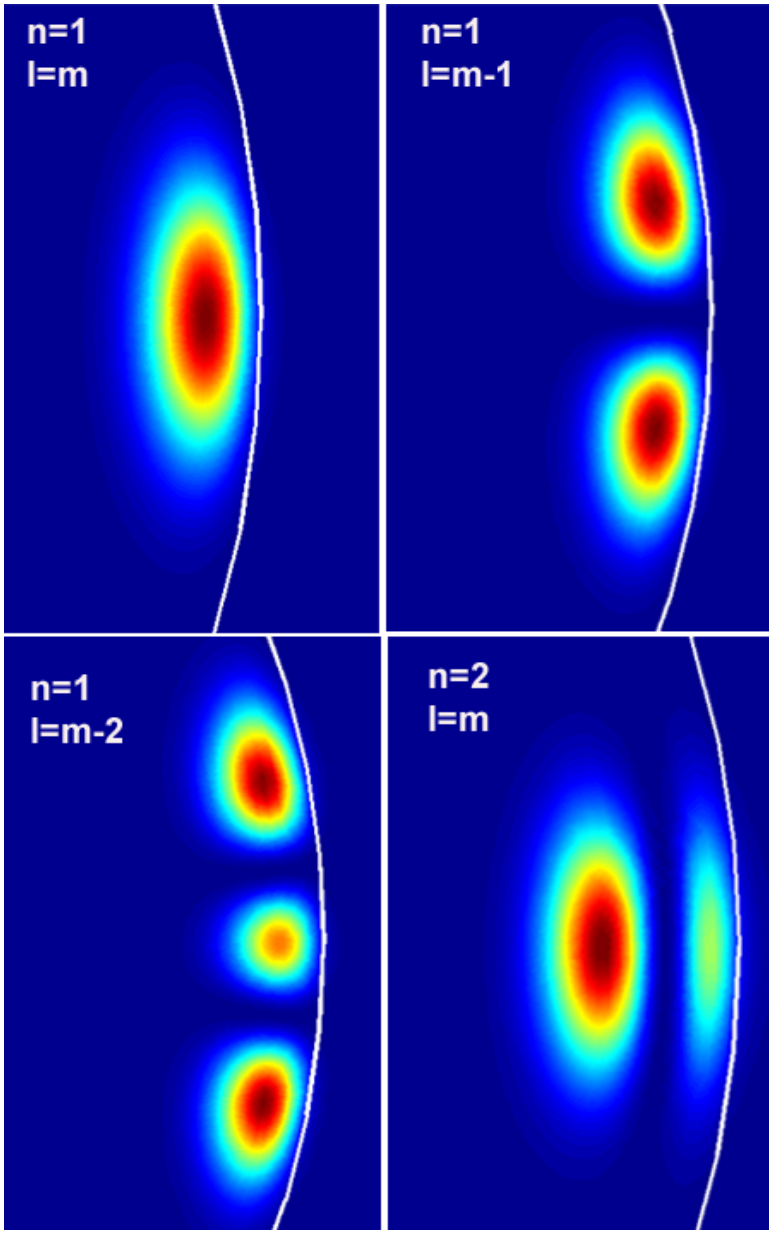

Figure 2.2: Numerical modeling of the intensity profile ($|E_\phi|^2$) of the whispering-gallery modes of a 25-$\mu m-$diameter microsphere, with polarization TM. In a perfect sphere modes with different azimuthal, but same radial and polar mode number, are frequency degenerate.

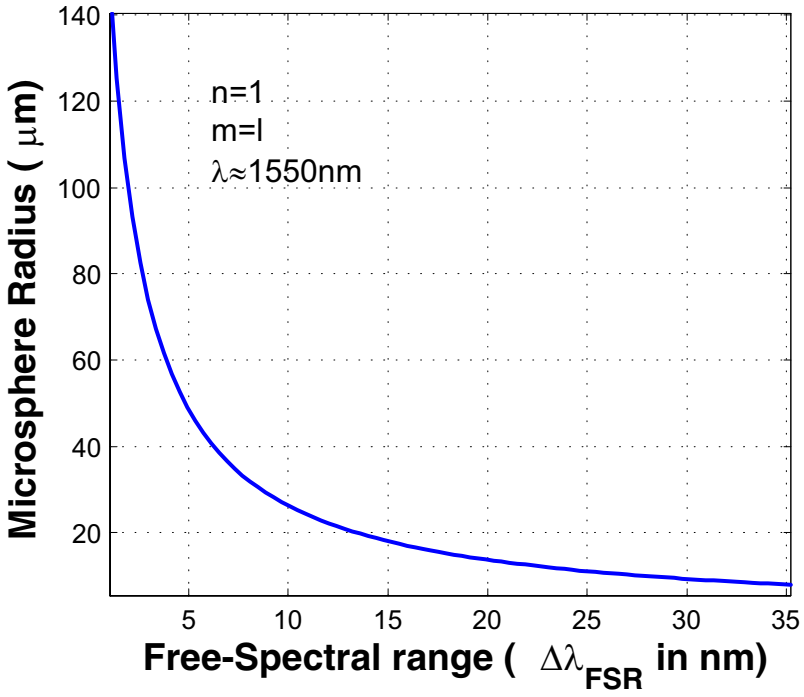

Figure 2.3: Free-spectral range $\Delta\lambda_{FSR} = |\lambda_{nm\ell} - \lambda_{nm\ell+1}|$ for a fundamental microsphere mode ($n = 1, m = l$) with an polar mode number consistent with a resonance in the 1550 nm band. The dependence is accurately described by $R[\mu m] = a \cdot 1/\Delta\lambda_{FSR}[nm] + b$, where $a = 264, b = -0.51$.

2.5 Eccentricity splitting

In an ideal sphere the optical modes possess a $2\ell + 1$ degeneracy with respect to the azimuthal mode number m. This can be understood by using classical ray optical interpretation, in which the optical modes with same ℓ, but different m, orbit around the equatorial plane by reflecting alternatingly from the lower to the upper hemisphere (and vice-versa), thereby taking different excursions away from the equator. The wave-vector associated with this trajectory is:

$$|\beta_l| = \frac{\ell(\ell+1)}{R_0}$$

and the projection onto the equatorial plane (i.e. the propagation constant) is given by:

$$|\beta_m| = \frac{m}{R_0}$$

The modes with low m take paths closer to the poles, and their longer path is compensated by a reduced number of reflections at the dielectric-air interface to complete one revolution. The so called fundamental modes, $m = \ell$ correspond to motion close to the equatorial plane (with an angle $\theta \propto \frac{1}{\sqrt{\ell}}$). Due to the invariable presence of imperfection, a microsphere will deviate from exact spherical shape, which will remove the degeneracy in path-length. If the shape deformation is weak, the new resonance frequencies can be calculated using perturbation theory. This has been treated in reference [39]. Elegant analytical results can be obtained, by treating a sphere with shape imperfections as a ellipsoid with radius $r(\theta) = r_0(1 + \frac{\epsilon}{3}(3\cos^2\theta - 1))$. Here the eccentricity ϵ is related to the polar r_p and equatorial radii r_e by $\epsilon = \frac{r_p - r_e}{R_0}$. This leads to analytically exact formulas[39] in the case of an axially symmetric shape distortion[4], as given by:

$$\frac{\Delta\omega_{ecc}}{\omega_{nml}} = -\frac{\epsilon}{6}\left(1 - 3\frac{|m|^2}{\ell^2}\right) \tag{2.7}$$

[4]It is interesting to note, that in the case of shape distortions which are not axially symmetric, the mode number m is not a "good quantum number", i.e. it will leads to eigenstates which are a linear superpositions of states with different m.

Hence the splitting between modes with successive azimuthal mode number is given by:

$$\Delta\omega_{ecc} \equiv |\omega_{nml} - \omega_{n,m+1,l}| \approx \omega_{nml} \cdot \epsilon \frac{|m| + 1/2}{\ell^2} \tag{2.8}$$

2.6 Loss mechanisms in a microsphere

Due to the presence of loss mechanisms such as material absorption, scattering losses or tunnel losses, the optical modes of a resonator are dissipative in character ("leaky") and are referred to as "quasi-modes". Quasi-modes are distinct to their loss-less counterparts (modes), and an excellent treatment on the properties of quasi-modes can be found in chapter 1 of ref. [40]. The extent to which dissipation is present in a resonant system is commonly expressed by the Quality-factor or Q-factor of the mode, which is defined by the energy storage time normalized with respect to the period of oscillation.

$$Q_0 \equiv \omega \frac{E_{stored}}{P_{diss}} = \omega\tau \tag{2.9}$$

In this equation ω is the resonance frequency, E_{stored} is the energy contained in the resonant system, and P_{diss} is the dissipated power. The above definition extends beyond the domain of electromagnetism, and is also used to characterize mechanical or electrical oscillators. Equivalently, in the case of optical microcavities the optical Q-factor describes the photon lifetime of a mode. In the case of a microsphere, the total Q-factor is comprised of several loss contributions: intrinsic material absorption, scattering losses (both intrinsic, as well as inherent to the surface of the cavity), surface absorption losses (e.g. due to the presence of adsorbed water), whispering-gallery loss (or tunnel loss) and external coupling losses to a "useful" external mode (such as a prism or a waveguide).

$$Q_{tot}^{-1} = Q_{mat}^{-1} + Q_{scatt}^{-1} + Q_{surf}^{-1} + Q_{ext}^{-1} + Q_{WGM}^{-1} \tag{2.10}$$

In the following sections the limits imposed by the different mechanisms are briefly reviewed and analyzed, for the case of silica microspheres involved in this work.

2.6.1 Intrinsic material loss

Silica has a large transparency window and exhibits low absorption losses. The minimum loss occurs at 1.55 μm, for which it has become the operating wavelength for fiber-optic telecommunications. The loss at 1.55 μm is $0.2dB/km$ and is equally comprised of absorption loss and loss due to Rayleigh scattering, which translates into an absorption limited Q of:

$$Q_0^{abs} = \frac{2\pi n_{eff}}{\lambda \alpha} \approx 2.92 \times 10^{10} \tag{2.11}$$

Absorption limited Q-factors have indeed be observed in large diameter (>200 μm) microspheres[41]. However for most of the work presented in this thesis absorption due to water, as well as surface scattering centers (as will be discussed in chapter 3) have presented a natural limitation of Q, with the highest Q-factor measured being ˜2×10^9 in the 1550 nm band.

2.6.2 Whispering gallery loss

The optical modes within a microsphere are confined by continuous total internal reflection at the dielectric cavity-air interface. However, it is a general property that total internal reflection at a curved interface is incomplete, and leads to a transmitted wave, which for the case of a resonator causes loss of optical energy[5]. This loss mechanism is called whispering-gallery loss, and is due to tunneling of the photons out of their bound states. This tunneling process, can be understood by drawing an analog to the quantum mechanical treatment of a 1-D particle in a central potential. Similarly to the latter can be achieved by formally rewriting the radial equation as an eigenvalue problem using the transformation $u(r) = \psi_r/r$ and introducing the energy

[5] A good intuitive explanation of this effect has been given in reference [42] by considering the phase velocities in a ray optical picture. For total internal reflection at a planar interface the exponentially decaying field components have a constant phase velocity $u_0 < c$ in the evanescent region. For a curved surface however, the phase velocity increase with increasing separation from the boundary i.e $u(r) = u_0 \frac{r}{R_0}$. At the point where the phase velocity exceeds the phase velocity in air ($u(r) > c$) the evanescent field becomes propagating, leading to tunnel losses.

term $E = k_0^2 n(r)^2$:

$$\frac{\partial^2}{\partial^2 r}u + \frac{\ell(\ell+1)}{r^2}u - k_0^2\left(1 - n(r)^2\right)u = k_0^2 n(r)^2 u = Eu \tag{2.12}$$

The effective potential $U_{eff}(r)$ of the particle is thus identified as:

$$U_{eff}(r) = \frac{\ell(\ell+1)}{r^2} - k_0^2(1 - n(r)^2) \tag{2.13}$$

Figure 2.4 shows a plot of the effective potential (normalized to k_0^2). The effective potential is discontinuous at the cavity-air interface, giving rise to a potential well. Furthermore the characteristic radii R_a and R_b are given by:

$$\begin{aligned} R_a &= \frac{\sqrt{\ell(\ell+1)}}{n}k_0 \\ R_b &= R_a n \end{aligned}$$

In the well region $R_a < r < R_b$ discrete bound states exist which correspond to the whispering-gallery modes. The region $r < R_a$ as well as $R_0 < r < R_b$ corresponds to a potential barrier, in which the optical modes are exponentially decaying (i.e. evanescent). The region $R_b > r$ supports a continuum of modes, which are unbound. Due to the finite height and finite width of the potential barrier in the region $R_0 < r < R_b$, the optical modes can tunnel from their bound well states into the continuum, giving rise to a tunnel-loss. The height and width of the potential barrier decreases as a function of the polar mode number ℓ, causing an increase in tunnel loss.

An approximate analytic formula for the whispering-gallery loss of a spherical, homogeneous dielectric resonator has first been derived by Weinstein [42], by expanding the characteristic equation and allowing the wave-vector to be complex. The result of this approach (extended here to include one more term in the perturbation expansion) is only valid in the limit $\ell \gg 1$.

$$Q_{WGM} = \frac{1}{2}\left(\ell + \frac{1}{2} - \beta t_q^0 - \frac{m^{1-2k}}{\sqrt{m^2-1}}\right) m^{-(1-2k)}(m^2-1)^{1/2} e^{2T_{n\ell}} \tag{2.14}$$

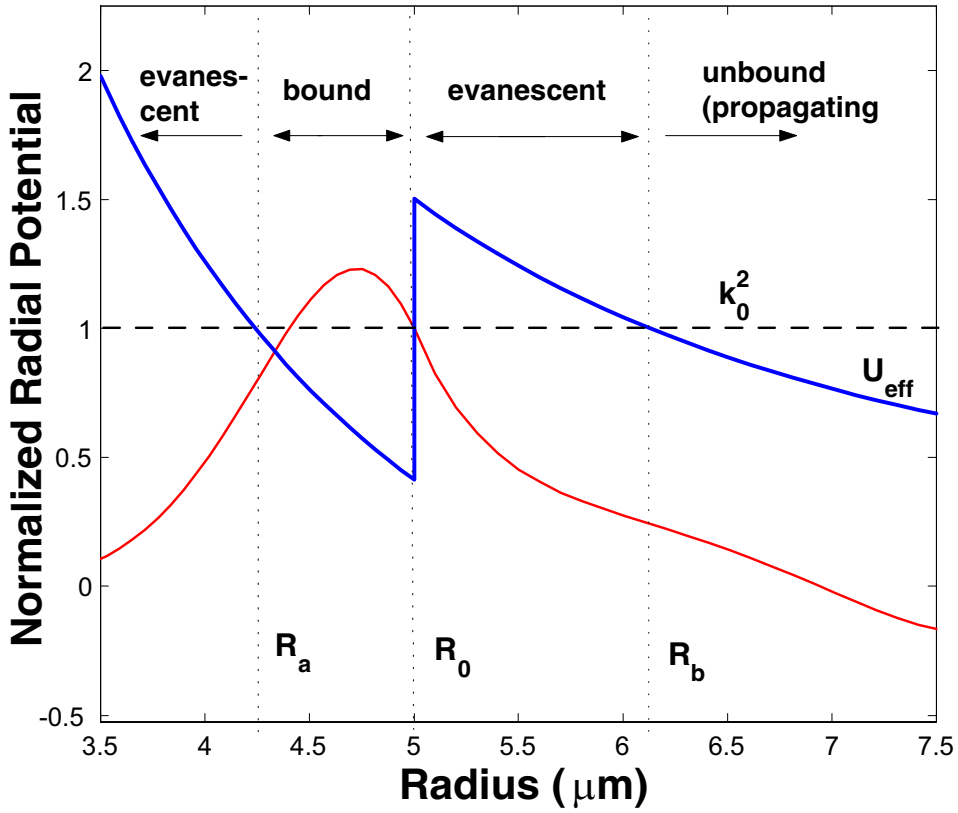

Figure 2.4: The effective radial potential for a microsphere with ($R = 10\ \mu m, l = 24$). The optical modes are bound in the region $R_a < r < R_0$, and evanescent in the region $R_0 < r < R_a$ and $R_b < r < R_0$. The tunneling from the evanescent region $R_0 < r < R_a$ into the region where the optical modes are unbound (i.e. $r > R_b$) leads to a tunnel loss, which is also referred to as "whispering gallery loss" and causes a finite Q (or line-width) of the modes.

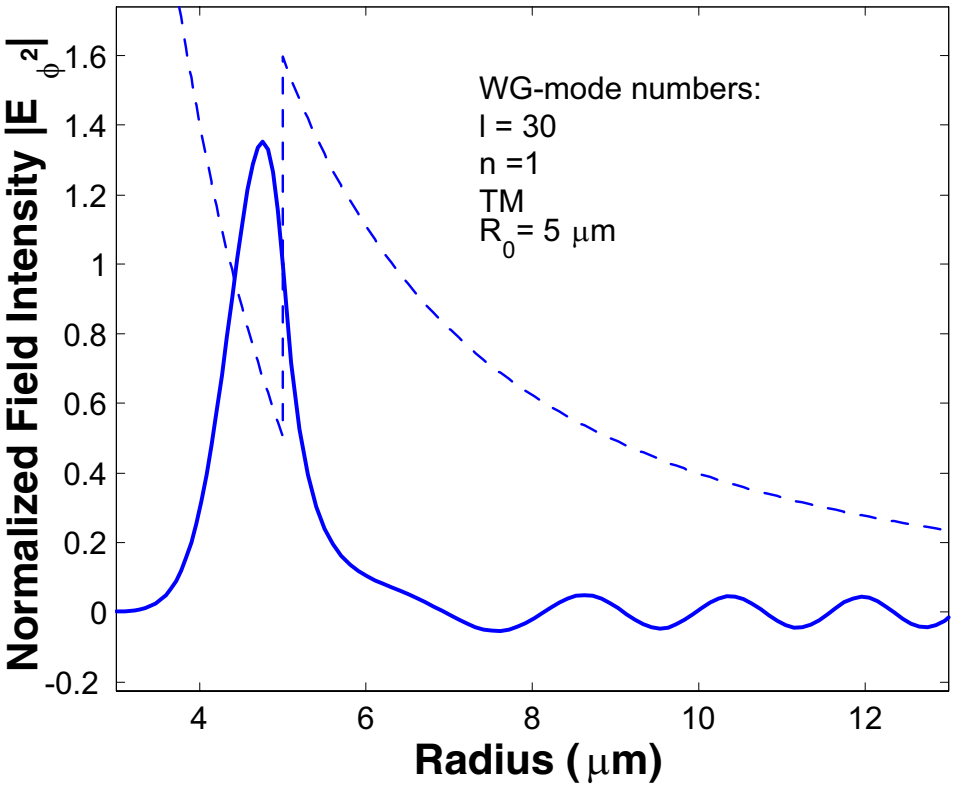

Figure 2.5: Radial intensity distribution ($|E_\phi|^2$) for a fundamental ($n = 1, \ell = m$) mode of a 5 -$\mu m-$radius microsphere with angular mode number $\ell = 30$, and TM polarization. The solution was obtained by solving the transcendental equation numerically for the imaginary part of ω. The dotted line denotes the effective radial potential, which is discontinuous at the dielectric cavity boundary.

Where m is the relative index of refraction, t_n^0 the Airy function zero and:

$$T_{n\ell} \equiv (\ell + \frac{1}{2}) \cdot \left(\cosh^{-1}(n) - \sqrt{1 - \frac{1}{m^2}} \right) + \beta_\ell t_n^0 \sqrt{1 - \frac{1}{m^2}} \qquad (2.15)$$

$$\beta_\ell \equiv \left(\frac{\ell + \frac{1}{2}}{2} \right)^{1/3}$$

The expression reveals however the important result of the exponential dependence of Quality factor on polar mode number $Q_{WGM} \propto e^{2\ell}$. Therefore the Q-factor exhibits a strong dependence on sphere diameter. For small polar mode numbers ℓ, the above expression is not precise and higher accuracy can be obtained by solving the characteristic equation numerically (iteratively). Figure 2.5 shows the "leaky" solution to the radial equation for a low-Q mode ($\ell = 30$) obtained by numerically solving eqs. 2.10. The oscillatory behavior of the field outside the sphere gives rise to tunnel loss. The Q-factor obtained by this method is plotted in figure 2.6 as a function of polar mode number ℓ, and in figure 2.7 as a function of microsphere radius for the experimentally relevant wavelength range $\lambda \approx 1550$ nm. As can be seen, a Q-value of $>10^8$ is maintained in the case of $R > 12\mu m$.

2.7 Mode volume of microspheres

In many applications, not only temporal confinement of light (i.e. the Q-factor), but also the extend to which the light is spatially confined is an important performance parameter. Several definitions of mode volume can be encountered in literature, and are discussed in this section. The most common definition of *mode volume*, is related to the definition of the energy density of the optical mode.

$$w_e(\mathbf{r}) + w_m(\mathbf{r}) = \frac{1}{2}\epsilon\tilde{\mathbf{E}}\tilde{\mathbf{E}} + \frac{1}{2\mu}\tilde{\mathbf{B}}\tilde{\mathbf{B}}$$

It is defined as the equivalent volume, the mode occupies if the energy density was distributed homogeneously throughout the mode volume, at the peak value:

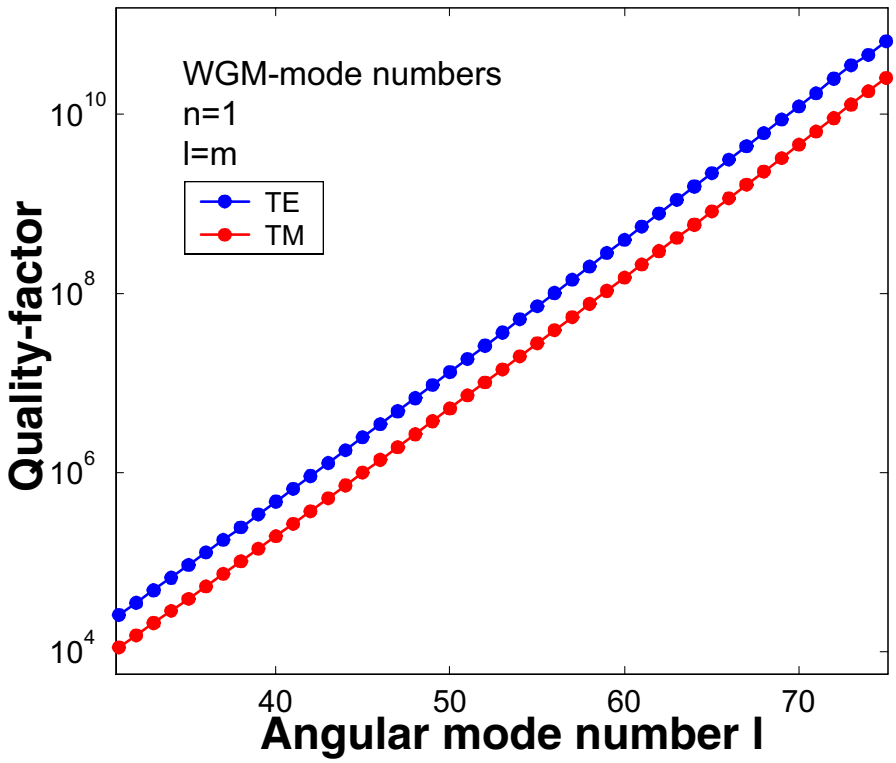

Figure 2.6: The whispering-gallery-loss limited Q for a fundamental microsphere mode (i.e. $n = 1, \ell = m$) as a function of the angular mode number (ℓ). The whispering gallery loss was obtained by solving the characteristic equation numerically, and allowing for complex eigenfrequencies $\omega = \omega_0 + i\Delta\omega/2$. (The Q-factor is correspondingly given by $Q = \omega_0/\Delta\omega$).

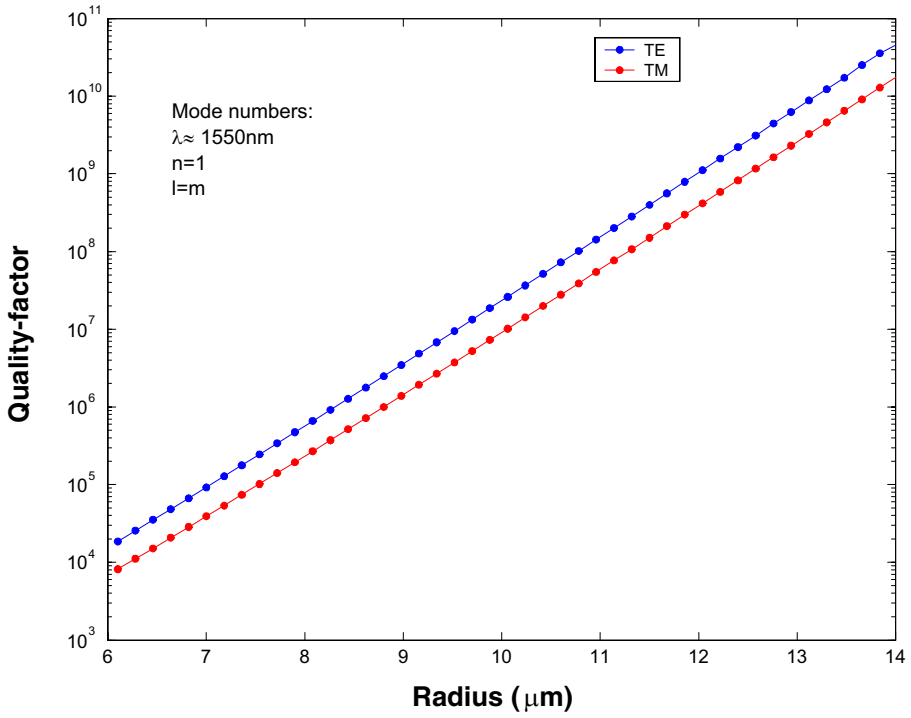

Figure 2.7: Whispering gallery loss versus microsphere radius for a polar mode number ℓ consistent with a resonance wavelength near 1550 nm, for a fundamental WGM. The TE-modes have intrinsically higher Q-factor than the TM-modes. For $R > 12$ μm Q>10^8 can be maintained.

$$V_{Mode} = \frac{\int \left(w_e(\mathbf{r}) + w_m(\mathbf{r})\right) dV}{\max(w_e(\mathbf{r}) + w_m(\mathbf{r}))} = \frac{\int \epsilon(\mathbf{r})|\vec{E}(\mathbf{r})|^2 d^3r}{\max(\epsilon(\mathbf{r})|\vec{E}(\mathbf{r})|^2)} \tag{2.16}$$

The integral is evaluated over all space, and also includes the regions where the field is evanescent[6]. Two comments are in place. First, it will be shown in chapter 5 and 6, that this definition of mode volume, differs from the definition of mode volume which will be encountered when studying nonlinear optical processes (which is called throughout this thesis *effective mode volume*, to emphasize the distinction).

Secondarily, the precise definition of mode volume is strictly speaking not rigorous. It depends on the physical problem studied (preceding comment), and as such different definitions can be found in literature. For instance, a more intuitive definition (that has been adopted by some authors) is to approximate the mode functions of a spherical WGM by an ellipse, and to evaluate the full-width-at-half-max of the radial a and azimuthal b intensity distribution yielding the mode volume $V_{mode} = R_0 \pi \frac{ab}{4}$. Comparison of this definition to 2.16 shows that the mode volume is ca. 1/3 lower in case the FWHM of the intensity distribution is evaluated. After these words of caution, definition 2.16 is used for the calculations shown in graph 2.8. It should be noted however, that independent of the mode volume definition, the numerical modeling allows comparison among different geometry parameters, and as

[6] It is noteworthy, that if one allows also for propagating components outside the dielectric cavity (i.e. finite Q) the mode volume diverges. This divergence is due the normalization problem, encountered in open systems. Due to the presence of propagating fields outside a whispering-gallery microcavity (whispering-gallery-loss, which occurs for any finite microcavity radius) the optical mode volume depends on the quantization volume chosen. This is easily seen by considering the propagating field component outside the microcavity. The electromagnetic field outside the resonator a distance R from the origin is proportional to:

$$E(R,t) \propto \frac{e^{ik(R-ct)}}{R}$$

In case of finite Q (as is the case for any whispering-gallery resonator, even in the absence of intrinsic losses due to the incomplete total internal reflection) the wave vector contains both a real and negative imaginary part (i.e. $k = k' - ik'', k'' > 0$). Therefore, the field increases outside the microcavity, as the exponential increase dominates over the slow $1/R$ dependence.

$$E(R,t) \propto \frac{e^{k''(R-ct)}}{R}$$

As a result, the mode volume, as defined in equation 2.16, diverges.

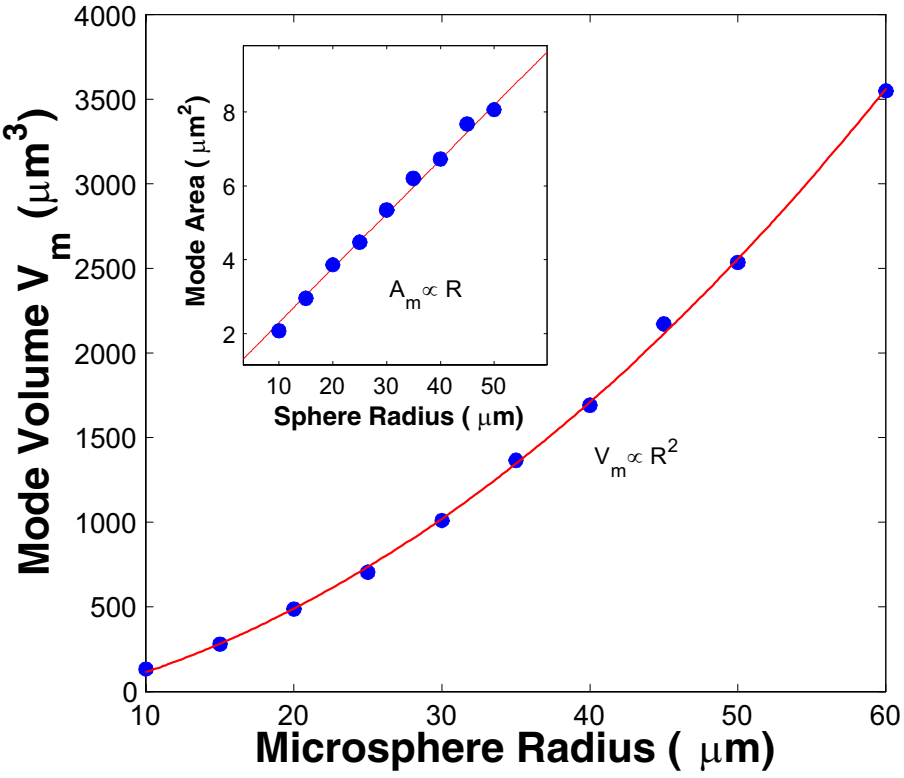

Figure 2.8: Numerically calculated mode volume V_m (using definition 2.16) for a microsphere as a function of radius. The polar mode number ℓ was adjusted such that the resonance wavelength location was close to 1550 nm. Inset: Plot of the mode area (A_m) vs. radius.

such allows comparison of the three types of cavity geometries studied in this thesis, i.e. microspheres (chapter 5,6), microtoroids (chapter 7,9,10) and microdisk cavities (chapter 8). Furthermore, figure 2.8 reveals that the mode volume of a sphere follows to a very good approximation a quadratic dependence on mode volume ($V_m \propto R^{11/12}$), whereas the effective mode area (shown in the inset) exhibits a linear dependence of sphere radius.

Chapter 3

Tapered optical fiber coupling

3.1 Introduction

In this chapter the tapered-optical fiber coupling technique is described. Tapered optical fibers were fabricated with waist diameters of typically less than 2 micron, and low loss (typically less than 5%). The tapered optical fibers allowed efficient and controlled excitation of ultra-high-Q whispering gallery modes, with negligible parasitic loss. This achievement is the prerequisite for the experiments which are described in the subsequent thesis chapters.

3.2 Evanescent coupling to microspheres using tapered optical fibers

Free-space excitation of microsphere whispering-gallery modes is extremely inefficient due different phase velocities in air and silica. Efficient excitation can be achieved using the evanescent coupling technique, which uses tunneling of evanescent field components with phase matched wave-vectors to achieve efficient coupling. A well known implementation of this method is using a total internally reflected beam within a prism. Prism coupling is well known since the 1960's and has been used to efficiently excite surface plasmon-polariton. Prism coupling has also been used to excite WGM of microspheres. Alternative methods have included eroded or side polished fibers

(D-shaped). By the bringing evanescent field region in close proximity to a silica microsphere, evanescent coupling can be achieved. A particularly suitable method has been proposed by [43][44], in which a fiber is drawn into a thin filament, and the evanescent field of the fiber is brought to overlap with the sphere. The particular advantage of this method is threefold. First, tapered optical fibers can be made with low-loss. Secondarily, tapered optical fibers allow highly efficient excitation of WGM, with negligible parasitically induced losses (such as scattering). In addition they allow not only excitation but also extraction of cavity fields through the same taper. Thirdly, the tapered optical fibers have small transverse dimensions, making them unique tools to excite WG-microcavities, with small dimensions (as will be shown in chapter 7,8).

In this section, the tapered optical fiber method is used to controllably couple light into a microsphere under phase matched condition, and allows to achieve high ideality. In addition the tapered optical fibers are ideal coupling elements to chip-based cavities, which will be investigated in chapter 7 of this thesis.

3.3 Fabrication of tapered-optical fibers

Tapered-optical fibers were fabricated by heating a SMF-28 optical fiber with a hydrogen torch. To control the flame a flow-controller (solenoid-valve with a flow meter) was used. In order to facilitate the experiments, a portable taper holder was designed, allowing taper-fabrication to be separate from the coupling setup. Figure 3.1 shows an image of the tapered fiber stage mounted onto the two motorized stages. The motorized stage is connected to the blocks (with two fiber clamps, Thorlabs) by two cylindrical posts. Crucial in the design of the stage is very low play in the movement of the optical blocks, which was achieved in the design by two cylindrical rails. Setscrews on the bottom of the blocks allowed fixing the posts, and a micrometer allowed post-tensioning of the fiber. During the pulling process, the motors we actuated simultaneously (Oriel motorized stages) and the fiber (with the cladding removed) was heated using a hydrogen torch. During fiber pulling the transmission

was monitored continuously and the taper imaged with a camera from the side (using a $\times 20$ objective). The approximate size of the taper could be inferred from measurement of the transmission, total pulling distance or by monitoring the tapered fiber using a microscope. Figure 3.2 shows a optical image tapered optical fiber. The fiber waist is clearly visible as the region exhibiting optical interference patterns (where the smallest diameter corresponds to the violet colored part on the left).

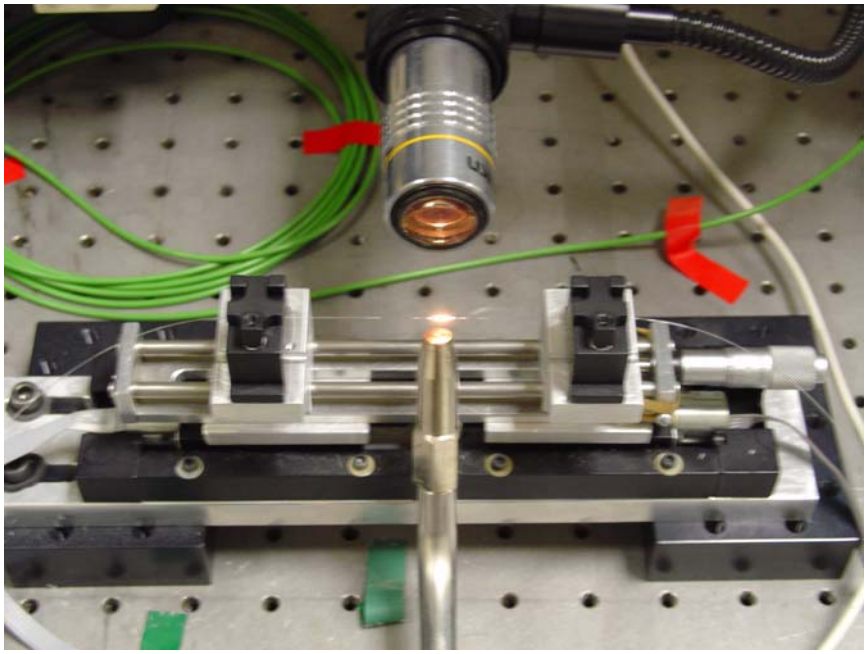

Figure 3.1: Tapered fiber pulling setup. The tapered optical fibers are held with fiber clamps which are located on a sliding block, with two rails. The whole structure is portable, and set-screws prevent movement of the blocks after pulling. The sliding blocks are attached via two posts to two motors, pulling the fiber symmetrically apart. A micrometer on the fiber pulling stage allows post-tensioning of the fiber.

In standard telecommunication fibers, light is confined by total internal reflection at the weak index contrast between the germanium doped core and the silica cladding. In a tapered optical fiber, the transverse extension of the fiber is reduced continuously, such that the optical energy residing outside the taper increases. Figure 3.3 shows the effective propagation constant of the fundamental taper mode as a function of

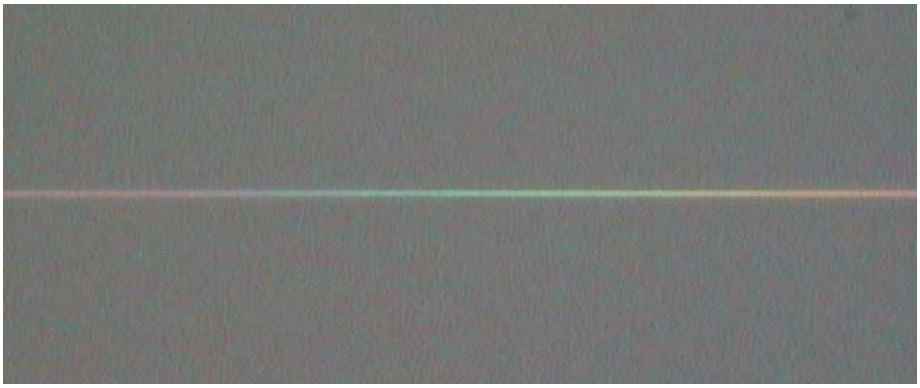

Figure 3.2: Optical micrograph of the waist region of a tapered optical fiber. The tapered fiber, which exhibits a diameter of less than 1 micron, appears colored due to interference effects. The waist diameter is decreasing from the right to the left side of the image.

taper waist diameter, and the optical energy residing outside the taper is shown in the inset.

3.3.1 Optical properties of tapered optical fibers

The optical modes of a tapered optical fiber, can be approximated by the modes of a dielectric cylinder. Particularly important in the context of taper fiber coupling is the fraction of energy which is outside the tapered fiber. It is the evanescent part of the field that can tunnel into a whispering-gallery mode cavity. Figure 3.3 shows propagation constant β_f of the fundamental tapered fiber mode, as a function of taper diameter in the experimentally relevant 1550-nm wavelength band. The results were obtained by finite element modeling using a full vectorial model. The evanescent taper field is given by the expression[37]:

$$\alpha_f = x \, \frac{K^1(x\beta_f)}{K^0(x\beta_f)}, x = \sqrt{\beta_f^2 - k_0 n_0^2}$$

Where $K^1$and K^0 are the Hankel functions of the first and second kind. It is important to note that by varying the taper thickness (which simply can be achieved by scanning along the fiber-taper) the propagation constant can be varied in a continuous fashion.

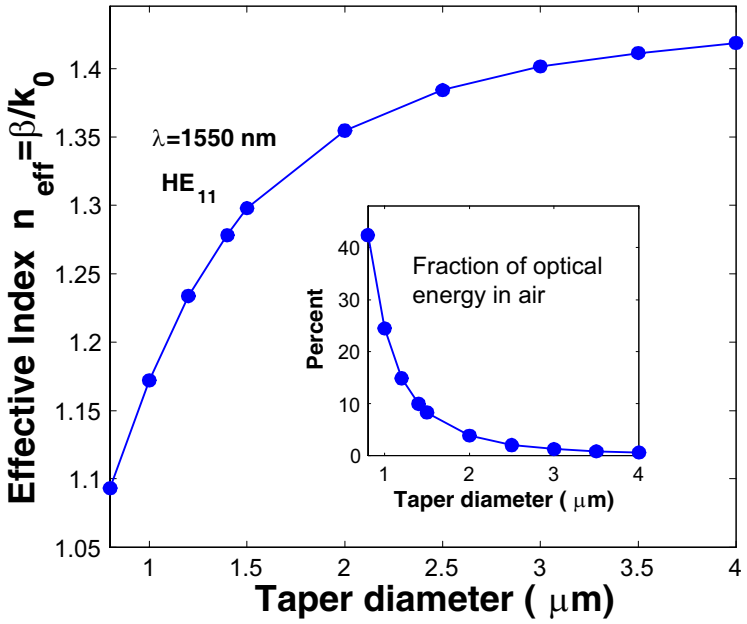

Figure 3.3: Main figure: Numerically calculated effective index n_{eff} of the fundamental HE_{11} taper mode as a function of the taper diameter (in the simulation $n = 1.44$). The fraction of electromagnetic energy that resides outside the dielectric taper region is shown in the inset.

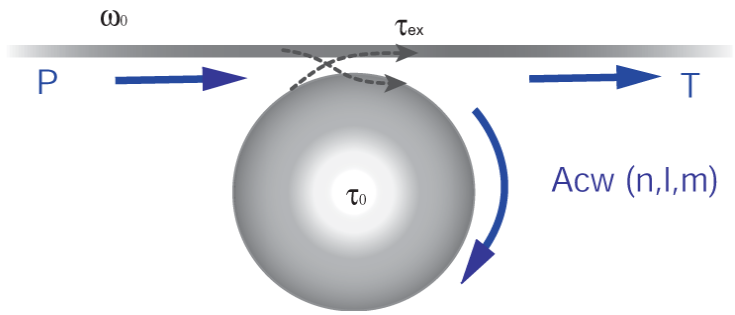

Figure 3.4: Schematic of a waveguide-coupled resonator.

This allows phase matching of the whispering- gallery modes of the cavity.

3.3.2 Mathematical description of the waveguide-resonator coupling junction

If the evanescent field of the fiber is brought in the proximity of a microcavity -such as a microsphere, microdisk or microtoroid cavity-, the fundamental optical mode will exhibit overlap of the whispering-gallery type modes of the microcavity. If the coupling is weak, and the perturbation of resonator and waveguide mode is small, the coupling can be described by the coupling-of-modes formalism[37] and in the slowly varying amplitude approximation. In case the coupling is strong, the behavior will ultimately differ and is then correctly described by a matrix model of the coupling amplitudes[45]. The two models will yield identical results as long as the slowly varying envelope approximation is valid, i.e. if the cavity field $E_c(t)$ satisfies $E_c(t+T) - E_c(t) \approx T\frac{d}{dt}E_c$, where T is the cavity round trip time. The coupling from a resonator to a waveguide is fundamentally described by three parameters, the resonant frequency ω_o, the decay rate $1/\tau_0$ of the mode due to internal cavity losses, and the cavity decay rate $1/\tau_{ex}$ due to coupling to the waveguide mode.

Following the coupling of modes approach given by H. Haus, the optical mode coupled to a whispering-gallery mode resonator can be described by the following equation[46]:

$$\frac{d}{dt}U = i\omega_o U - \left(\frac{1}{2\tau_0} + \frac{1}{2\tau_{ex}}\right) U + \kappa s \tag{3.1}$$

Here the resonator excitation is designated as U and the waveguide mode is designated as s[1].The intrinsic lifetime as denoted by τ_0 describes the total losses inherent to the optical resonator, and the coupling into the waveguide is given by τ_{ex}. In the absence of coupling to a waveguide the optical energy $E = |U|^2$ in the resonator decay exponentially with time,

$$\frac{d}{dt}|U|^2 = U\frac{d}{dt}U^* + U^*\frac{d}{dt}U = -\frac{1}{\tau_0}|U|^2 \tag{3.2}$$

And the quality factor is given by $Q_0 = \omega\tau_0$. In the presence of a waveguide such as a taper the optical energy is dissipated both within the cavity as well as due to coupling to the waveguide. In case of a loss-less resonator, and in the presence of a waveguide, the decay is entirely due to the waveguide coupling, designated by $\frac{d}{dt}|U|^2 = -\frac{1}{\tau_{ex}}|U|^2$ (τ_{ex} external lifetime). The coupling coefficient κ can related to τ_{ex} by time reversal symmetry, yielding:

$$|\kappa| = \sqrt{\frac{1}{\tau_{ex}}} \tag{3.3}$$

Furthermore the transmission past the resonator is of interest. The transmission is linear in the cavity and input fields, such that the coefficients of the relation $t = c_1 s + c_2 U$ have to be found. The coefficient c_2 can be found by considering the cavity mode in the absence of waveguide excitation ($c_1 = 0$), yielding $c_1 = \sqrt{\frac{1}{\tau_{ex}}}$. To find the relation for c_2 , power conservation can be used. i.e. the net power transfer into the cavity, must be equal to the rate of growth of the cavity field added to the rate of intrinsic dissipation.

$$|s|^2 - |t|^2 = \frac{d}{dt}|U|^2 + \left(\frac{1}{\tau_0}\right)|U|^2 \tag{3.4}$$

[1]Particular attention has to be paid to the two different normalizations used in this formalism:
$|s|^2$ = normalized to Power
$|U|^2$ =normalized to Energy

Furthermore from the equation of motion the power dissipated in the resonator is given by:

$$\frac{d}{dt}|U|^2 = -\left(\frac{1}{\tau_{ex}} + \frac{1}{\tau_0}\right)|U|^2 + \sqrt{\frac{1}{\tau_{ex}}}(Us^* + U^*s) \tag{3.5}$$

Substituting $U = \sqrt{\tau_{ex}}\,(t - c_1 s)$ into the last two equations yields:

$$\begin{aligned} |s|^2 - |t|^2 &= -\frac{1}{\tau_{ex}}|U|^2 + \sqrt{\frac{1}{\tau_{ex}}}(Us^* + U^*s) = \\ &= -\frac{1}{\tau_{ex}}\left|\sqrt{\tau_{ex}}t - c_1 s\right|^2 + (t - c_1 s)\,s^* + (t - c_1 s)^*\,s \end{aligned}$$

Comparing the equations yields $c_1 = -1$:

$$t = -s + \sqrt{\frac{1}{\tau_{ex}}}U \tag{3.6}$$

The transmission past the resonator is correspondingly given by $\Delta\omega = \omega_0 - \omega$.

$$T = \left(\frac{\tau_{ex} - \tau_0 - i\Delta\omega}{\tau_{ex} + \tau_0 + i\Delta\omega}\right)^2 \tag{3.7}$$

The transmission properties are commonly characterized by over-coupled, critically coupled and under-coupled.

- **Undercoupling:** Under-coupling refers to the case where the waveguide coupling is weak and the cavity decay rate τ_0^{-1} exceeds the cavity coupling rate τ_{ex}^{-1}. In this case the amplitude of the cavity leakage field $U/(2\tau_0)$ is much smaller the amplitude of the transmitted waveguide field. The cavity leakage field exhibits a phase shift of $\pi > \phi > 0$.

- **Over-coupling:** In the over-coupled regime the rate of cavity coupling exceeds the cavity decay rate $\left(\tau_{ex}^{-1} > \tau_0^{-1}\right)$. The amplitude of the cavity decay field in this case is larger than transmitted pump field, and reaches a value of twice the waveguide amplitude in the case of strong over-coupling.

- **Critical coupling:** Critical coupling occurs when the external lifetime is matched to the intrinsic cavity decay rate $\left(\tau_{ex}^{-1} = \tau_0^{-1}\right)$. In this case the transmission past the resonator vanishes, and complete power transfer of the optical power carried by the wave to the cavity mode occurs. The transmission vanishes due to the interference of the cavity leakage field and transmitted pump field, which exhibit equal magnitude but a relative phase shift π.

3.3.3 Cavity-buildup factor

At the critical coupling point the optical energy in the cavity reaches it's maximum, and the circulating power is given by the cavity-buildup factor, where $\Delta\lambda_{FSR}$ is the free-spectral range of the cavity:

$$\left(\frac{P_{cav}}{P_{in}}\right) = \frac{c\Delta\lambda_{FSR}}{\lambda^2}\frac{1}{\tau_{ex}}\left(\frac{1}{2\tau_0} + \frac{1}{2\tau_{ex}}\right)^{-2} = \frac{\lambda}{\pi^2 R n_{eff}} Q_{ex}\left(1 + \frac{Q_{ex}}{Q_0}\right)^{-2} \tag{3.8}$$

This shows that within in microcavity, the circulating power is significantly enhanced, and can be exploited to significantly reduce the threshold for nonlinear optical phenomena, which is presented in this thesis.

3.3.4 Experimental observation of controlled evanescent taper-fiber coupling to microsphere resonators

The different coupling regimes as discussed in the previous section could indeed be observed, by accurately controlling the taper microsphere distance. Figure 3.5 shows a microsphere coupled to a tapered-optical fiber. The coupling amplitude is determined by the spatial overlap of the whispering gallery mode with the mode of the tapered optical fiber. Efficient coupling is achieved when the propagation constant of the taper is matched to the propagation constant of the whispering gallery mode[2], and the

[2]The propagation constant of a whispering gallery mode is simply given by the relation $\beta = m/R_0$. To evaluate the coupling from the tapered optical waveguide to the whispering gallery mode resonator, the directional dependence of β has to be taken into account.

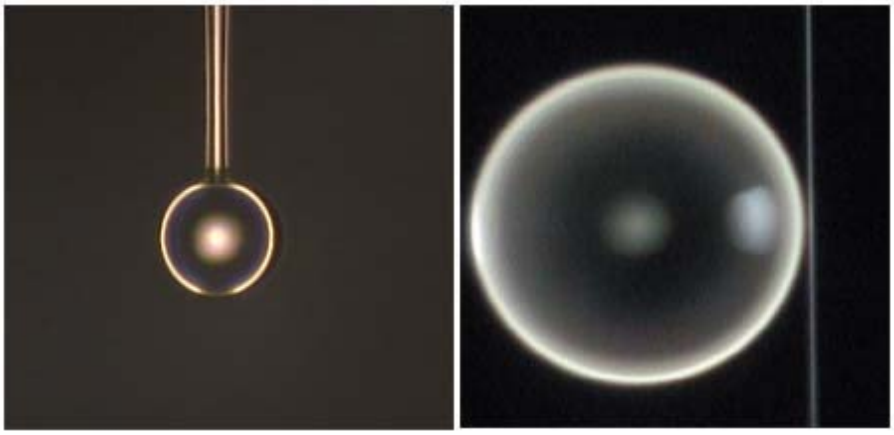

Figure 3.5: Right panel: Microsphere coupled to a tapered optical fiber. Left panel: Microsphere visible with fiber stem.

coupling strength has been theoretically analyzed in reference [37]. The propagation constant of the fiber taper can be continuously varied by scanning the taper along the waist diameter (compare figure 3.3).

The coupling properties analyzed in the last section, assumed the case of a single mode waveguide, coupled to a mode of a resonator. However, the coupling will also induce a non-resonant loss (e.g. due to scattering at the junction). In addition the tapered fibers are not single-mode (unless the diameter $< 1.2\ \mu m$) such that the resonator can couple in principle into the fundamental and higher order taper modes. These effects will become pronounced in the over-coupled regime, causing a deviation from complete recovery of the transmission. Observing the postulated transmission behavior will therefore require that the coupling into the fundamental taper mode dominates over higher order mode coupling, while the coupling amplitude κ remains small. In addition, the off-resonant loss (e.g. junction induced scattering) has to be small, which was indeed observed (compare chapter 3). The extent to which the system behaves as predicted is given by the *"Ideality"* which has been extensively investigated in reference *[26]*, and will not be treated in the author's thesis. [3]. It is

[3] A detailed analysis of the effect of higher order mode coupling has been carried out by Sean Spillane and is contained in reference [26] and his thesis.

merely noted that a more complete description of the junction includes the effect of coupling to both higher order taper and radiation modes. The extent to which higher order mode coupling is present can be expressed in terms of the junction-ideality I.

$$\frac{d}{dt}U = i\omega_o U - \left(\frac{1}{2\tau_0} + \frac{1}{2\tau_{ex}^0} + \sum_{i>0}\frac{1}{\tau_{ex}^i}\right)U + \sqrt{\frac{1}{\tau_{ex}}}s \tag{3.9}$$

$$I \equiv \frac{1/\tau_{ex}^0}{1/\tau_{ex}^0 + \sum_{i>1}\frac{1}{\tau_{ex}^i}} \tag{3.10}$$

The experimentally predicted coupling regimes under ideal assumption as in eqs. 3.7 could indeed routinely be observed. As the evanescent taper and microsphere fields decay exponentially, the external coupling κ is expected to vary exponentially i.e. $\tau_{ex}^{-1} = \tau_{ex}^{-1}(0)\exp(-x/\gamma)$, where $\tau_{ex}^{-1}(0)$ is the external coupling rate with the taper in contact with the resonator. The characteristic coupling length is determined by the overlap of sphere and taper mode, and therefore determined by the taper and microsphere evanescent field decay. The evanescent field decay of a sphere is given by[37]:

$$\alpha_s = \sqrt{\beta_l^2 - k_0 n_0^2} \text{ and } \beta_l = \frac{\ell(\ell+1)}{R_0}$$

whereas in the case of a silica tapered optical fiber[37]:

$$\alpha_f = x\,\frac{K^1(x\beta_f)}{K^0(x\beta_f)}, x = \sqrt{\beta_f^2 - k_0 n_0^2}$$

The overlap of the two fields determines the coupling coefficient, which therefore varies approximately as $\gamma \simeq (\alpha_f + \alpha_s)$ .The fiber propagation constant is found by matching the boundary condition for the fiber fields. In figure 3.3 the propagation constant for a fundamental fiber mode $\beta_f = n_{eff} \cdot k_0$, has been numerically calculated for the fundamental taper mode HE_{11} using a finite element solver.

Figure 3.11 shows the observation of different coupling regimes by variation of the taper-microsphere coupling gap. In this measurement the transmission through the taper was normalized with respect to the power transmitted in the far under-

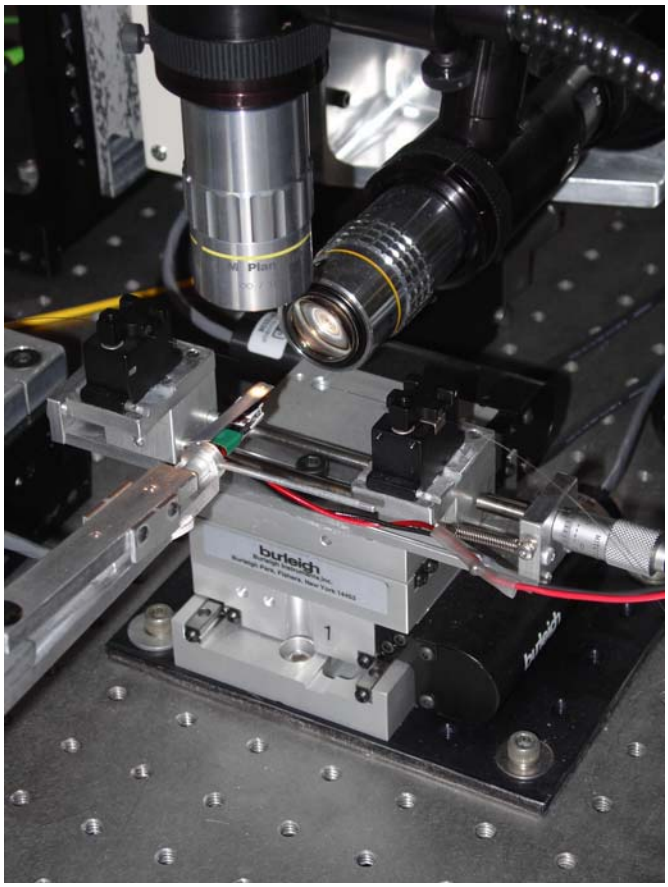

Figure 3.6: Photograph of the fiber-taper coupling setup. The fiber-taper stage is attached to a closed loop piezoelectric positioning system, which gives lateral motion in two directions (with 20 nm resolution). Visible in the front is the positioning arm, to which microspheres or planar cavities can be attached. The arm itself is attached to the third axis of the piezo-electric stage.

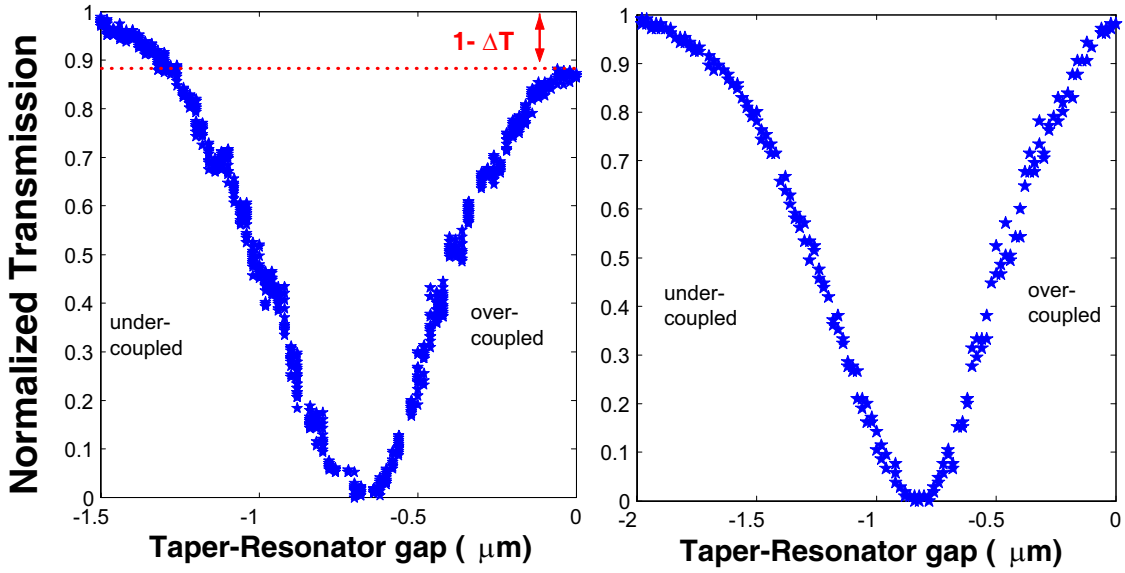

Figure 3.7: Coupling regimes for a tapered-optical-fiber resonator system. The experiments show the recorder transmission on resonance versus the coupling gap distance for two whispering-gallery resonators. The zero point corresponds to the taper being in contact with the resonator. The transmission in this experiment is normalized with respect to the taper removed from the resonator. The left panel shows the coupling curve with high ideality, whereas the left curve exhibits low ideality, as witnessed by the reduced transmission in the over-coupled regime, due to junction scattering.

coupled region. The different coupling regimes are clearly identified, and at the critical coupling extinction is large than 99%. Upon decreasing the coupling gap further, recovery of the transmitted signal is found as predicted by equation 3.7. In the right panel of figure 3.11, recovery exceeds 99%, whereas for the panel in the left the off-resonant loss has increased by 10%.

The taper coupling mechanism is in general mode selective, but as shown here also allows to excite higher azimuthal ($|m| < l$) modes. Figure 3.8 shows a tapered optical fiber coupled to a microsphere. The microsphere contained erbium (by using ion implantation), which functioned as a probe for the intensity profile of the excited whispering-gallery modes. As can be seen in the figure, the tapered optical fiber can efficiently excite fundamental and higher order azimuthal modes. It is interesting to note that the equatorial plane of the WGM is determined by the fiber stem, and

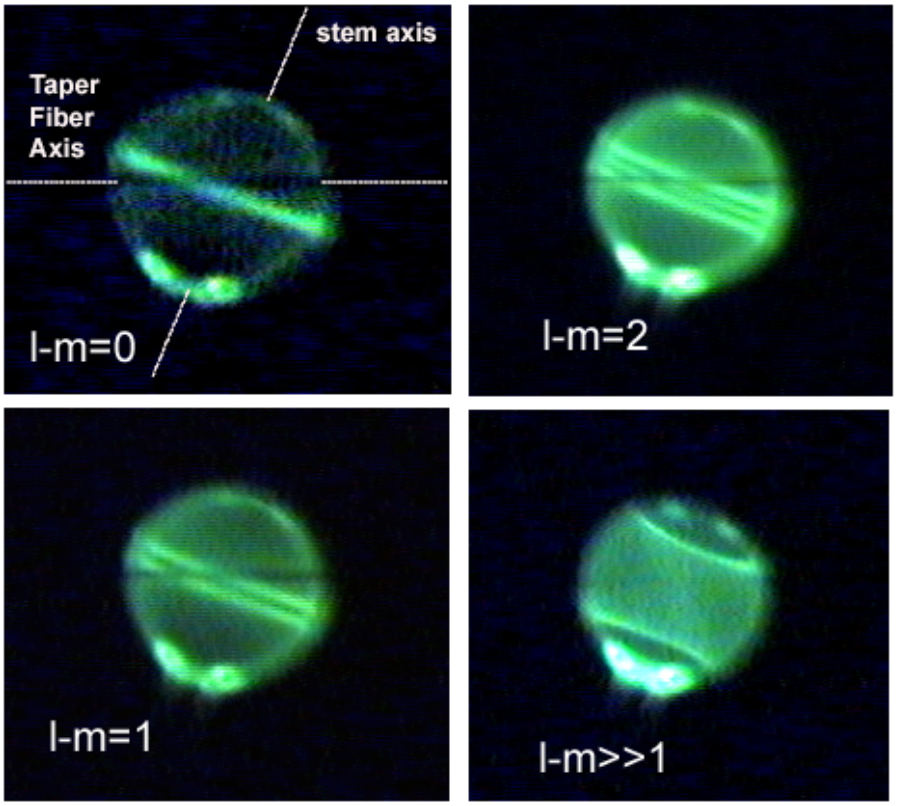

Figure 3.8: Excitation of whispering-gallery modes in a microsphere using a tapered optical fiber. The equatorial plane of the WGM is defined by the stem of the microsphere, and is angled with respect to the taper axis. The number field of maxima in the polar direction is given by $\ell - m + 1$. The optical modes are made visible in this experiment by the presence of erbium ions, implanted into the microsphere surface. The green luminescence is originating from the $^2H_{11/2}$ stark level of erbium, excited via a combination of coorporative up-conversion and excited state absorption.

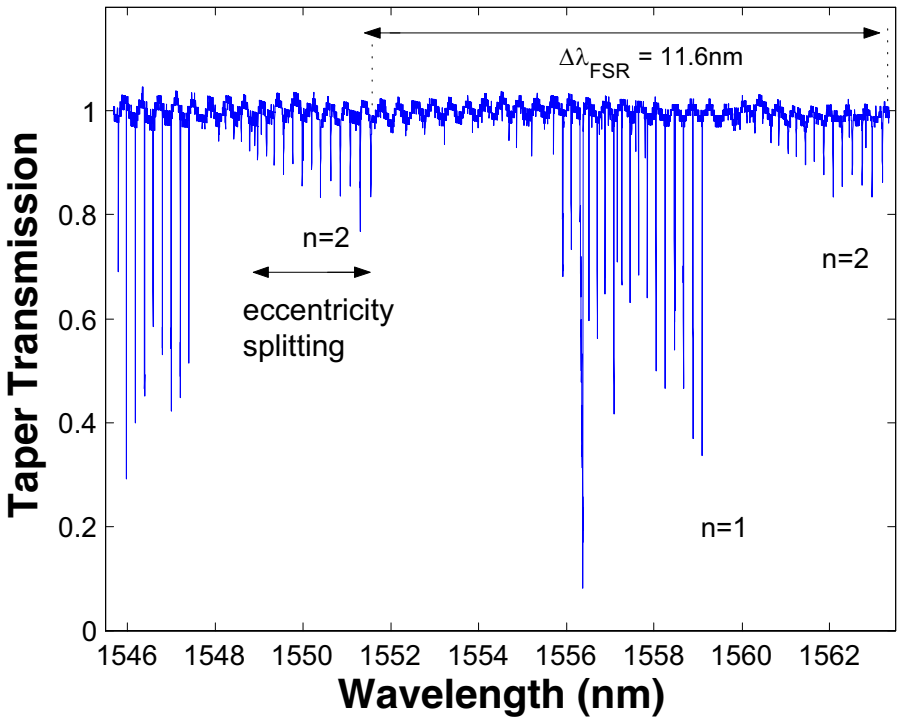

Figure 3.9: Broadband transmission spectrum of a microsphere with radius of ca. 22 μm. The eccentricity splitting of the azimuthal modes is clearly visible, which is 0.2 nm. This corresponds to an eccentricity of $\epsilon \approx 1\%$. The strongly coupled modes are identified as fundamental radial modes ($n = 1$), and the weakly coupled modes are identified as $n = 2$. Note that only ca. 20 azimuthal modes are excited with the tapered optical fiber, of the total $2\ell + 1$ eccentricity split modes ($\ell \approx 130$). The latter is due to the mode selectivity and reduced phase matching for high m-values.

is angled with respect to the taper fiber axis. This plane orientation corresponds to smallest perturbation of the optical modes due to the stem. The excitation of higher order azimuthal modes, split due to eccentricity, is also seen in the broadband transmission spectrum as seen in figure 3.9. As evident, also higher order radial modes can also be excited, based on the resonance locations inferred from equation 2.5.

3.4 Linewidth measurements and thermal effects

Since the optical Q-factor determines the threshold for nonlinear optical effects, methods to accurately quantify the Q are necessary. The optical quality factor of the whispering-gallery modes was measured in this thesis both in the time and frequency domain. For a resonator mode the energy decay is given by:

$$U(t) = U(0)e^{(i\omega_0 - \frac{1}{2\tau})t} \rightarrow U(\omega) = U(0)\frac{1}{i(\omega_0 - \omega) - \frac{1}{2\tau}} \tag{3.11}$$

In the latter, the linewidth of the resonance can be simply related to Q via $Q = \frac{\omega}{\Delta\omega}$. In the case of high-Q resonance, the transmission $T(\Delta\omega)$ only re-produces the transfer function $|U(\omega_0 - \omega)|^2$, if the cavity field has reached steady state, which occurs for times larger than the cavity storage time τ. The transfer function can therefore be conveniently measured by scanning the laser through a resonance, provided the laser is scanned with a speed $\left[\frac{nm}{s}\right]$ that satisfies the relation:

$$v[\frac{nm}{s}] << \frac{\Delta\lambda}{\tau}10^9 = \frac{2\pi c}{Q^2}10^9 \tag{3.12}$$

For a typical scan range of 60 GHz for the laser used in this work (New Focus external cavity laser), and a Q-factor of 2×10^8 this limits the scan speed of the laser to approximately 100 Hz. The resolution of the linewidth measurements is limited by the coherence time of the pump laser, which limits the Q-factor measurement to approximately 1.5×10^8(short term linewidth of 300 kHz, long term 1 MHz).

However, due to the small volume occupied by the WGM mode, and poor thermal conductivity of silica microspheres, strong thermal effects occur even at low pump

power, which are due to the temperature dependent resonance locations:

$$\frac{d}{dT}\lambda(n,R) = \lambda\frac{dn}{dT} + \lambda\frac{dR}{dT}$$

The resonance shift is primarily due to the temperature dependence of the refractive index $\frac{dn}{dT} = 1.28 \times 10^{-5} K^{-1}$, while the thermal expansion of the silica $\alpha_T = 5.5 \times 10^{-7}$ induces a much smaller shift for the cavities considered in this work $R \approx 20 - 100\mu m$. For the 1550 nm wavelength range this translates into a thermal tuning coefficient of $\frac{d\nu}{dT} = 2.5$ GHz$/K$. The thermal effects have to be taken into account carefully when measuring Q-factor. In particular heating of the cavity will lead to bistability behavior with respect to the scanning direction of the laser beam (induced by cavity heating when scanning the laser in the same direction as the wavelength shift). The thermally induced wavelength shift also leads to the appearance of oscillations in the transmission spectrum, upon scanning past a thermally broadened resonance. These oscillations are due to interference of the pump laser, with the cavity leakage field (that is frequency red-shifted due to cooling of the cavity). Therefore quality factor measurements are only a reliable measure in the case of very weak excitation, where the latter effects are not present.

3.5 Cavity ring-down measurements

The thermal broadening effects, as well as the transient effects associated with scanning over a cavity resonance constitute a systematic error in the measurement of the cavity Q-factor. In addition the linewidth measurement is coherence-limited to a Q-value of approximately 1.5×10^8. To overcome this limitation, and also the intrinsic uncertainty in the linewidth measurement, a cavity ring-down measurement setup was implemented. Cavity ring-down allows to directly record the photon lifetime in time domain. In contrast to linewidth measurement, cavity ring-down is principally insensitive to the thermal broadening and allows determination of the *loaded* Q-factor even at high pump power. In addition, the laser linewidth is not a limitation of this

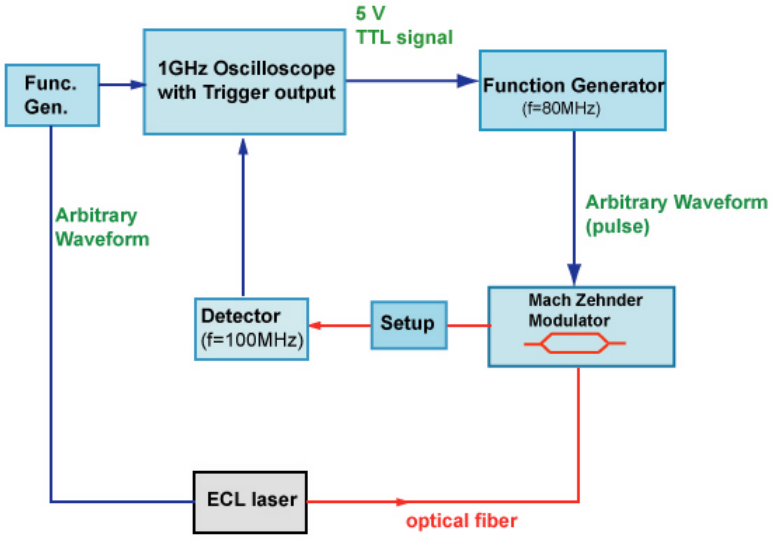

Figure 3.10: Schematic of the cavity ring-down setup to measure photon lifetimes.

method.

Important for the measurement of the cavity lifetime, is to ensure a fast gating-off of the pump laser, as well as timing the gating once the mode was fully charged at the critical point. Indispensable for these measurements and their proper timing was a 1GHz oscilloscope with external trigger capability (Tektronixs TDS 5104). The experimental setup is shows in figure 3.10. The laser was gated off using a high-speed $LiNbO_3$ Mach Zehnder modulator (UTP), which was driven by an arbitrary function generator (Agilent), which limited the gating time to approximately 8 ns. Ring-down measurements at the critical coupling point were achieved by scanning the laser simultaneously until the transmission vanished at the critical point. To ensure gating-off at the critical point the reflected signal was used for the trigger, and the trigger level set to a value close to the peak reflection. A typical ring-down measurement is shown in figure 3.11. To increase the temporal window for the trigger, ringdown measurements were performed on the thermally broadened side of the resonance. For times $t < 0$, the cavity mode has reached steady state and is following the laser due

to thermal shifting of the wavelength. At time $t = 0$, the trigger is activated, and the laser gated off with a delay Δt of 8 ns. Therefore the critical decay signal is given by:

$$|s_{RD}(t)|^2 = \left(\frac{2\tau_{ex}}{\tau_0 + \tau_{ex}}\right)^2 |s(t=0)|^2 \, e^{-(t+\Delta t)\left(\frac{1}{\tau_{crit}}\right)}$$

Figure 3.11 shows a typical decay trace obtained using the described experimental setup. The quality factor can be inferred by fitting the cavity decay field, as well by measuring the recovery of the transmission. Note that at $t = 0$ in the strongly over-coupled regime the cavity decay signal reaches values up to 4 times the input signal.

The ringdown measurement have been carried out at the critical coupling point, where the taper transmission vanishes. Operation of this point was motivated twofold. First, the critical coupling point, can be accurately identified experimentally by recording the taper transmission ($T = 0$), and is relatively stable with respect to taper fluctuations (since $\frac{dT}{dx} = 0$). Secondarily, while under-coupled ringdown measurements allow direct measurement of intrinsic Q, the cavity decay amplitude is larger at the critical point allowing for better signal-to-noise ratio upon signal detection. In addition, the ultra-high-Q modes are in nearly all cases observed as doublets, due to modal coupling. Therefore ringdown in the undercoupled regime, requires locking to one of the doublet eigenmodes, whereas at the critical point, the splitting of the two eigenmodes is masked.

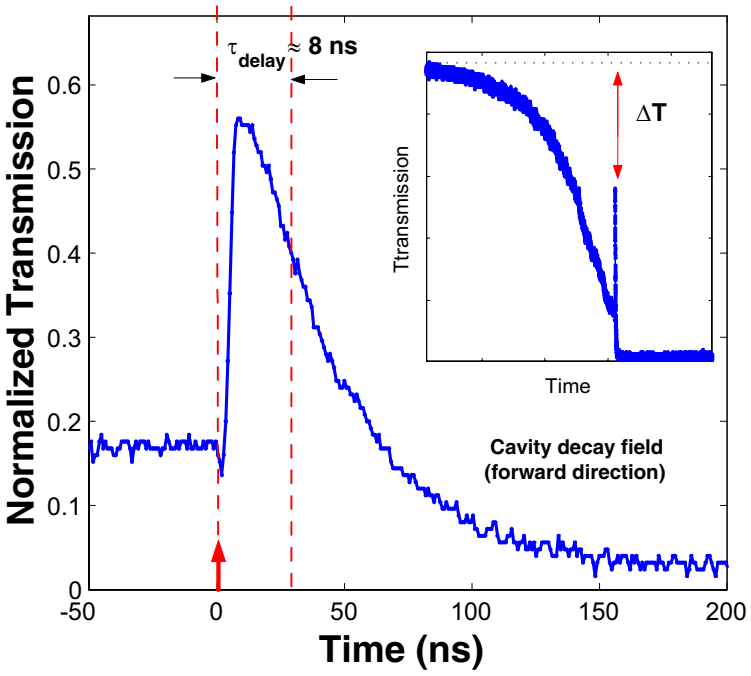

Figure 3.11: Cavity ringdown measurement trace. Main figure: The transmission past the microcavity as a function of time. For $t = 0$ the pump field is gated off, which occurs with a delay of approximately 8 ns. For $t > 8$ ns the recorded transmission is entirely due to the cavity leakage field. The inset shows the recovery of the transmission, upon gating-off the laser.

Chapter 4

Modal coupling in whispering-gallery-type resonators

4.1 Introduction[1]

The splitting of degenerate levels (which transforms energy level crossings into anti-crossings) in the presence of coupling is a very general principle in physics; the formation of energy bands in semiconductors (level repulsion) can be attributed to this principle, as well as the splitting of atomic levels in the presence of (LS) coupling. In this thesis chapter an optical analog of this effect is studied, that was encountered in whispering-gallery type resonator such as microspheres, microdisks and microtoroids, as considered in this thesis. Each mode in a whispering-gallery type resonator possesses a natural 2-fold degeneracy, in addition to degeneracies with respect to other "quantum numbers" (such as the azimuthal mode number in microspheres) resulting from the two possible directions of propagation (clockwise CW and counterclockwise CCW) [47]. Lifting of the degeneracy and coupling of the two modes can occur when a fraction of the mode energy is scattered into the oppositely oriented mode. The degeneracy can also be lifted by rotating the whispering gallery-type resonator around its symmetry axis, which causes the CCW mode and CW mode to exhibit different round trip times, and correspondingly removing the degeneracy in their resonance

[1] **This chapter has appeared in "Modal Coupling in traveling-wave resonators"** ***Optics Letters*****, 27 (19) 1669-1671, 2002.**

frequency. [2]

The consequences of degeneracy lifting by distributed scattering has been first theoretically investigated by [48]. In this chapter we experimentally confirm these predictions using high-Q ($> 10^8$) micro-sphere resonators coupled to fiber-optic taper waveguides. The long photon lifetimes of high-Q micro-sphere resonators make possible a counter-intuitive effect in which minute scattering gives rise to the regime of strong modal coupling. In this regime scattering into the oppositely oriented mode is the dominant scattering process. Resonances are significantly split and severe deviations of the critical coupling point occur. We show and observe that in certain regimes the whispering-gallery resonator can acts as a narrow bandwidth reflector, causing a strongly reflected signal and vanishing waveguide transmission. The altered coupling properties are of importance in high-Q micro-resonator based cavity QED and nonlinear optical experiments [49, 40].

4.2 Modal coupling in whispering-gallery-type resonators

In a traveling wave resonator such as a microsphere, Rayleigh scattering from surface inhomogeneities or density fluctuations will transfer power from the initially excited mode to all the confined and radiative modes of the resonator. The scattering to all modes other than the CW and CCW mode is included in the overall effective loss, given through the intrinsic lifetime τ_0. The cross coupling of modes can be described using coupled-mode theory and using the slowly varying envelope approxi-

[2] This effect is referred to as Sagnac effect, and can be used to create rotation sensors (Gyroscopes). The presence of modal coupling in these systems leads to the formation of a photonic band structure.

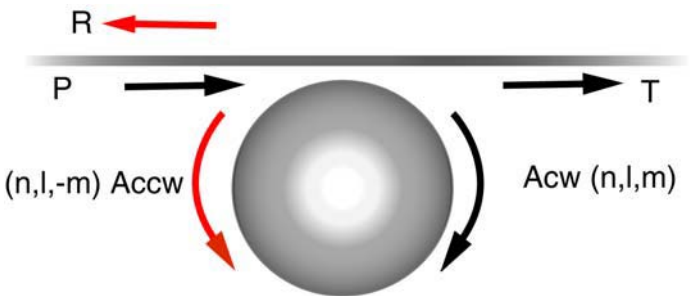

Figure 4.1: Schematic of a traveling-wave resonator coupled to a waveguide. The input power launched through the waveguide is denoted as $P = |s|^2$. The two eigenmodes of the resonator couple back into the waveguide giving rise to reflection ($R = |r|^2$) and transmission ($T = |t|^2$).

mation(equivalent to that presented in reference [48]).

$$\begin{aligned} \frac{d}{dt}a_{cw} &= i\Delta\omega \cdot a_{cw} - \left(\frac{1}{2\tau_0} + \frac{1}{2\tau_{ex}}\right) \cdot a_{cw} + \frac{1}{2\gamma_{12}} \cdot a_{ccw} + \kappa \cdot s \\ \frac{d}{dt}a_{ccw} &= i\Delta\omega \cdot a_{ccw} - \left(\frac{1}{2\tau_0} + \frac{1}{2\tau_{ex}}\right) \cdot a_{ccw} + \frac{1}{2\gamma_{21}} \cdot a_{cw} \end{aligned} \tag{4.1}$$

Here a_{cw}, a_{ccw} is the amplitude of the CCW and CW modes of the resonator and s denotes the input wave. The excitation frequency is de-tuned by $\Delta\omega$ with respect to the resonance frequency ω_0 of the initially degenerate modes, τ is the total lifetime of photons in the resonator, which is related to the quality factor by $Q = \omega \cdot \tau$. The coupling coefficient κ denotes the coupling of the input wave to the CW mode of the resonator. The relation $\kappa = \sqrt{1/\tau_{ex}}$ associates the coupling coefficient with a corresponding lifetime, where the total lifetime is given by $1/\tau = 1/\tau_{ex} + 1/\tau_0$. The mutual coupling of the CCW and CW mode is described by a (scattering) lifetime γ. Since the cross-coupling is only to redistribute energy between the CW and CCW modes, the scattering coefficients must obey the relation:

$$\begin{aligned} \frac{d}{dt}\left(|a_{cw}|^2 + |a_{ccw}|^2\right) + \left(|a_{cw}|^2 + |a_{ccw}|^2\right)\left(\frac{1}{2\tau_0} + \frac{1}{2\tau_{ex}}\right) &= 0 \\ \frac{1}{2\gamma_{12}}a_{ccw}a_{cw}^* + \frac{1}{2\gamma_{12}^*}a_{ccw}^*a_{cw} + \frac{1}{2\gamma_{21}^*}a_{cw}^*a_{ccw} + \frac{1}{2\gamma_{21}}a_{cw}a_{ccw}^* &= 0 \end{aligned} \tag{4.2}$$

This is satisfied if the cross-coupling coefficients obey:

$$\gamma_{12} + \gamma_{21}^{*} = 0 \tag{4.3}$$

Which requires that γ_{12} and γ_{21} must be imaginary i.e. setting $\gamma_{12} = -i\gamma$. Further details about the model and its validity can be found in [46].[3] The coupling of the resonator modes to the waveguide gives rise to a transmitted (t) and reflected (r) field:

$$t = -s + \sqrt{\frac{1}{\tau_{ex}}} \cdot a_{cw}; \quad r = \sqrt{\frac{1}{\tau_{ex}}} \cdot a_{ccw} \tag{4.4}$$

The state-state solution for the clockwise and counterclockwise excitation of the resonator modes are given by the expressions:

$$\begin{aligned} a_{cw} &= \kappa s \frac{i\Delta\omega + (\tau_0^{-1} + \tau_{ex}^{-1})}{-\Delta\omega^2 - \gamma^2 + (\tau_0^{-1} + \tau_{ex}^{-1})^2 + i\Delta\omega(\tau_0^{-1} + \tau_{ex}^{-1})} \\ a_{ccw} &= \kappa s \frac{-2i\gamma}{-\Delta\omega^2 - \gamma^2 + (\tau_0^{-1} + \tau_{ex}^{-1})^2 + i\Delta\omega(\tau_0^{-1} + \tau_{ex}^{-1})} \end{aligned} \tag{4.5}$$

The new eigenmodes are now symmetric and anti-symmetric superpositions[4] of the degenerate CW (n, ℓ, p, m) and CCW $(n, \ell, p, -m)$ modes centered around new eigenfrequencies $\omega = \omega_0 \pm \frac{1}{2\gamma}$ (having a linewidth of $1/\tau$).

$$\begin{aligned} u^{S} &= \frac{1}{\sqrt{2}} (a_{cw} + a_{ccw}) \\ u^{AS} &= \frac{1}{\sqrt{2}} (a_{cw} - a_{ccw}) \end{aligned} \tag{4.6}$$

It is noteworthy that in the presence of modal coupling the eigenmodes lose their purely traveling wave character, as given by the azimuthal dependence $\Psi_{\phi}^{cw,ccw} \propto \exp(\pm im\phi)$. If the two amplitude of the clockwise and counterclockwise excitation

[3] It should be noted that in this expression the quantity $|s|^2$is normalized to the power carried by the waveguide , in contrast to the resonator amplitude excitation a which is normalized such that $|a|^2$ corresponds to the Energy in the resonator mode.

[4] The new eigenmodes are spatially symmetric and anti-symmetric with respect to the symmetry plane of the waveguide-resonator system.

are equal, the eigenmodes of the system correspond to (two orthogonal) standing waves, i.e. $\{\cos(m\phi), \sin(m\phi)\}$.

Modifications to the resonator coupling physics (transmission, reflection and circulating power) can be described in terms of the normalized modal coupling parameter:

$$\textbf{Modal Coupling Parameter } \Gamma \equiv \tau_0/\gamma. \tag{4.7}$$

The normalized coupling parameter describes the extent of splitting with respect to the intrinsic cavity lifetime, and as such is a natural measure of how observable the mode splitting in the undercoupled regime is (compare figure **??**). In addition we introduce the normalized coupling coefficient to facilitate the discussion:

$$\textbf{Normalized Coupling Parameter } K \equiv \tau_0/\tau_{ex} \tag{4.8}$$

Using this definition, critical coupling corresponds to $K = 1$,over-coupling corresponds to $K < 1$ and under-coupling corresponds to $K > 1$. The Transmission ($T = |t|^2$) as a function of the previously introduced parameters and the normalized frequency detuning $\Delta\overline{\omega} \equiv \Delta\omega \cdot \tau_0$ is:

$$T(\Delta\overline{\omega}, \Gamma, K) = \left| \frac{\Gamma^2 + (1-K)(1+K) - \Delta\overline{\omega}^2 + 2i\Delta\overline{\omega}}{\Gamma^2 + (1+K)^2 + 2i\Delta\overline{\omega}} \right|^2 \tag{4.9}$$

The corresponding reflection ($R = |r|^2$) coefficient is given by:

$$R(\Delta\overline{\omega}, \Gamma, K) = \left| \frac{2\Gamma K}{\Gamma^2 + (1+K)^2 + 2i\Delta\overline{\omega}} \right|^2 \tag{4.10}$$

The doublet resonance locations for the reflection and transmission (i.e. $\frac{dR}{d\Delta\overline{\omega}} = 0, \frac{d^2R}{d\Delta\overline{\omega}^2} < 1$ and $\frac{dT}{d\Delta\overline{\omega}} = 0, \frac{d^2T}{d\Delta\overline{\omega}^2} > 1$) are located at: $\Delta\overline{\omega} = \pm\sqrt[2]{\Gamma^2 - (1+K)^2}$ and for the transmission at $\Delta\overline{\omega} = \pm\sqrt[2]{\Gamma^2 + 1 - K^2}$.

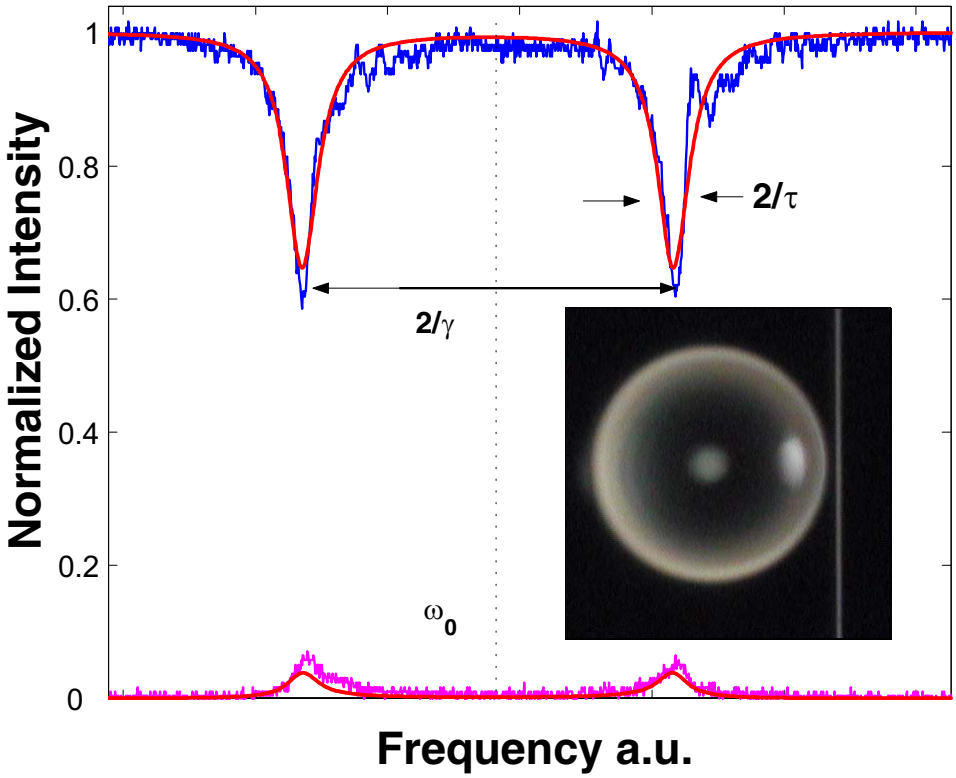

Figure 4.2: Spectral transmission and reflection properties of a 70 μm sphere with $Q_0 = 1.2 \cdot 10^8$ [50] in the regime of strong modal coupling with $\Gamma = 10$. The solid line represent a fit using the presented model from equation 1. The inset shows a microsphere coupled to a tapered fiber.

4.3 Experimental observation of the regime of strong modal coupling

We experimentally observed the frequency splitting of whispering-gallery modes in a fiber-coupled [51] micro-sphere resonator. Due to the high-Q (typically exceeding 10^8) resonances frequently occur as doublets, since only minute scattering is required to cause easily observable mode splitting of the clockwise ($|n, l, m\rangle$) and counterclockwise ($|n, l, -m\rangle$) whispering gallery modes[52]. The waveguide-resonator interface [53], the resonator surface, and thermodynamic inhomogeneities [48] in the resonator itself can all induce scattering. However, the use of small (typically in the range of $D \approx 50\mu m$), high-Q resonators has the advantage that efficient power transfer from the waveguide to the mode can occur with the waveguide several microns removed from the resonator surface. In this way, the presence of the waveguide has a negligible contribution to the overall scattering and distributed scattering centers intrinsic to the resonator or its surface can dominate. As evidence of this, we found the splitting frequency to increase only slightly (less than 5%) while decreasing the taper-sphere gap.

The inset of figure 4.2 shows a photograph of a micro-sphere (diameter ca. 70 μm) coupled to a tapered fiber. The taper is attached to a 20 nm resolution positioning stage to adjust the taper-sphere gap, which allows accurate control of the external lifetime τ_{ex} (and correspondingly K). A 1.55 μm tunable laser source is used to excite a Whispering Gallery Mode (WGM) of the resonator. The laser is scanned repeatedly through a scan range of 60 GHz, containing the resonance doublet. In the experiments the forward and backward transmission through the tapered fiber was recorded as a function of taper-sphere gap. The recorded transmission and reflection spectra were simultaneously fitted to the coupled mode model of equation **??**, and the model parameters inferred. Figure **??** shows a resonance doublet for a 70 μm sphere ($Q_0 = 1.2 \cdot 10^8$) with a resonance splitting of approximately $\Gamma = 10$.

An ideal whispering-gallery-type resonator (characterized by $\Gamma = 0$) allows electromagnetic energy carried by a waveguide to be completely transferred to the resonant

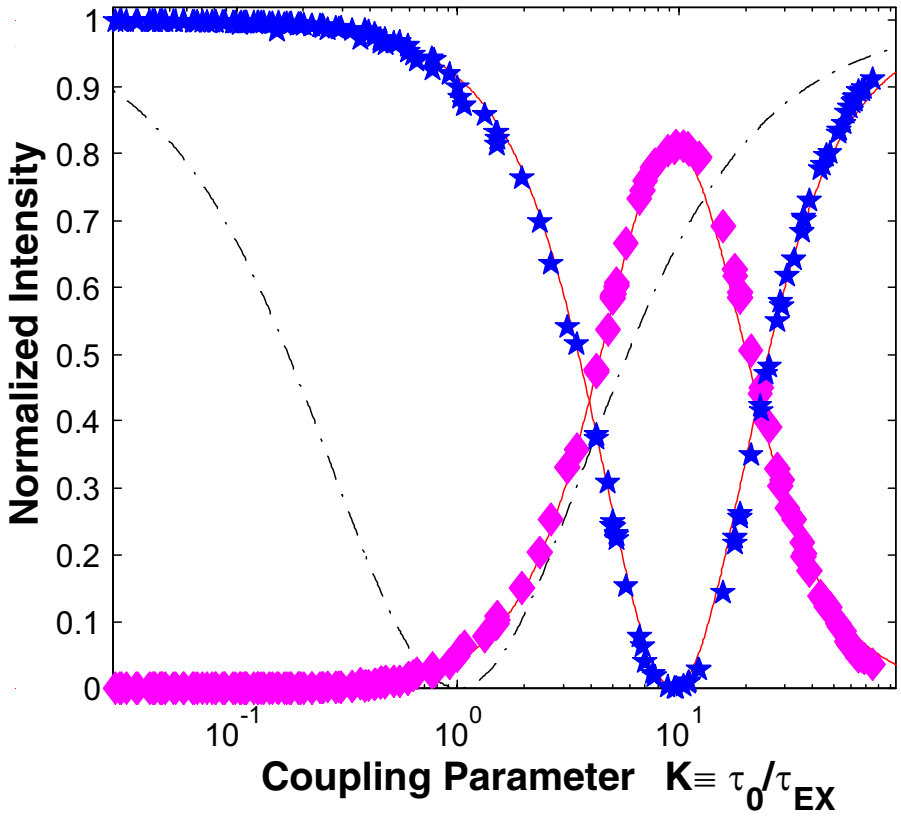

Figure 4.3: Transmission (stars) and reflection (diamonds) behavior for the case of symmetric $\Delta\omega = 0$ excitation vs. K [54], for a mode with $Q_0 = 1.2 \cdot 10^8$ and a modal coupling of $\Gamma = 10$. The solid line is a theoretical fit using the model from equation 4.1, under the assumption of constant scattering γ and constant intrinsic lifetime τ. For large backscattering the minimum $T = 0$ occurs at $K \approx \Gamma$ (compare with equation 4.11) and is accompanied by a maximum back-reflection of 84%. The dotted line shows the transmission for an ideal whispering-gallery micro-resonator in the absence of backscattering, where critical coupling occurs for $K = 1$.

mode - a property which in the optical and microwave domain is termed 'Critical Coupling' [55]. Figure 4.3 shows the power transmission and reflection as a function of external coupling for symmetric excitation ($\Delta\omega = 0$) of a resonator mode. In the absence of scattering ($\Gamma = 0$, corresponding to the dashed curve in figure 4.3) the critical point - the point where the waveguide transmission vanishes - occurs at $K = 1$. The fact that the critical coupling point coincides with the point of maximum circulating power is due to the uni-directionality of an ideal traveling-wave-resonator. The forward input mode of the waveguide is coupled to only one (CCW or CW) mode of the resonator. In the presence of backscattering uni-directionality is lost, drastically altering the coupling properties. The modifications are particularly interesting in the regime of strong modal coupling ($\Gamma \gg 1$). Even in this regime the condition of critical coupling - vanishing waveguide (taper fiber) transmission ($T = 0$) - can be achieved. However, only for the case $\Delta\omega = 0$, as can be seen in figure 4.3. The doublet structure in the transmission at this point vanishes, as the two resonances in transmission are located at:

Furthermore the presence of two eigenmodes changes the transfer-function of the waveguide resonator system to a second order (i.e. causes the presence of two poles). In the transmission this can be observed in particular at the critical point, as a flattened frequency response[5]. In addition, the point of zero transmission is accompanied by a maximum reflected signal. This feature can be understood as an interference effect; the excited CCW and CW modes couple back into the two taper directions. The CW mode interferes destructively with the incoming wave (with the clockwise cavity decay field exhibiting a π-phase shift, resulting in zero (forward) transmission, while the CCW mode leaks back into the opposite direction, causing (back-) reflection. Analyzing the equations it is important to realize that the condition of vanishing waveguide transmission (T=0) has changed and occurs for:

$$K_{crit} \equiv \left(\frac{\tau_0}{\gamma}\right) = \sqrt{1+\Gamma^2} \tag{4.11}$$

[5] The filter reponse in the presence of modal coupling is 2^{nd} order, and is equal to the configuration of two uni-directional resonators, coupled with a rate equal to the scattering rate γ^{-1}.

This expression shows a significant shift of the critical point is possible and causes renewed attention of the definition of critical coupling. The critical coupling point is therefore strongly dependent on the modal coupling and occurs in what would, in the absence of modal coupling, be considered the over-coupled regime, since vanishing transmission occurs for $\tau_{ex} < \tau_0$. The amount of over-coupling required for zero transmission increases monotonically versus modal coupling. (As an aside, we note that the condition $K = 1$ has the special property of causing a transmission and reflection of equal magnitude *irrespective* of inter-mode coupling strength.). It should further be noted that in the case of strong modal coupling, the linewidth (or corresponding photon lifetime) at critical coupling is entirely dominated by the splitting frequency, i.e.

$$\tau_{crit} = \sqrt{\left(\frac{1}{\gamma}\right)^2 + \left(\frac{1}{\tau_0}\right)^2}^{-1} \underset{\tau_0 \gg \gamma}{\approx} \gamma. \tag{4.12}$$

The experimental data presented in figure 4.3 was obtained for a mode exhibiting a modal coupling of $\Gamma = 10$ and $Q_0 = 1.2 \cdot 10^8$. The observed maximum back-reflection was 84%. This agrees very well with the theoretically predicted maximum of 82% (see figure 4.4). In addition the point of maximum back-reflection and zero forward transmission occurs where theoretically predicted. For reference, the dotted line in the figure gives the case of an ideal WG-resonator characterized by no modal coupling ($\Gamma = 0$). As can be seen the critical coupling point is significantly shifted to smaller separations from the microsphere.

The solid line in Figure 4.4 is a fit obtained using a constant splitting frequency and constant intrinsic lifetime. The theoretical fit shows excellent agreement with the experimental data, despite the fact that the splitting frequency was found to vary slightly as a function of resonator loading.

The maximum reflection is observed at the critical point and is given by:

$$R_{crit} = \left(\frac{\Gamma}{1 + \sqrt{1 + \Gamma^2}}\right)^2 \tag{4.13}$$

The reflection asymptotically approaches unity in the limit of large Γ with all incom-

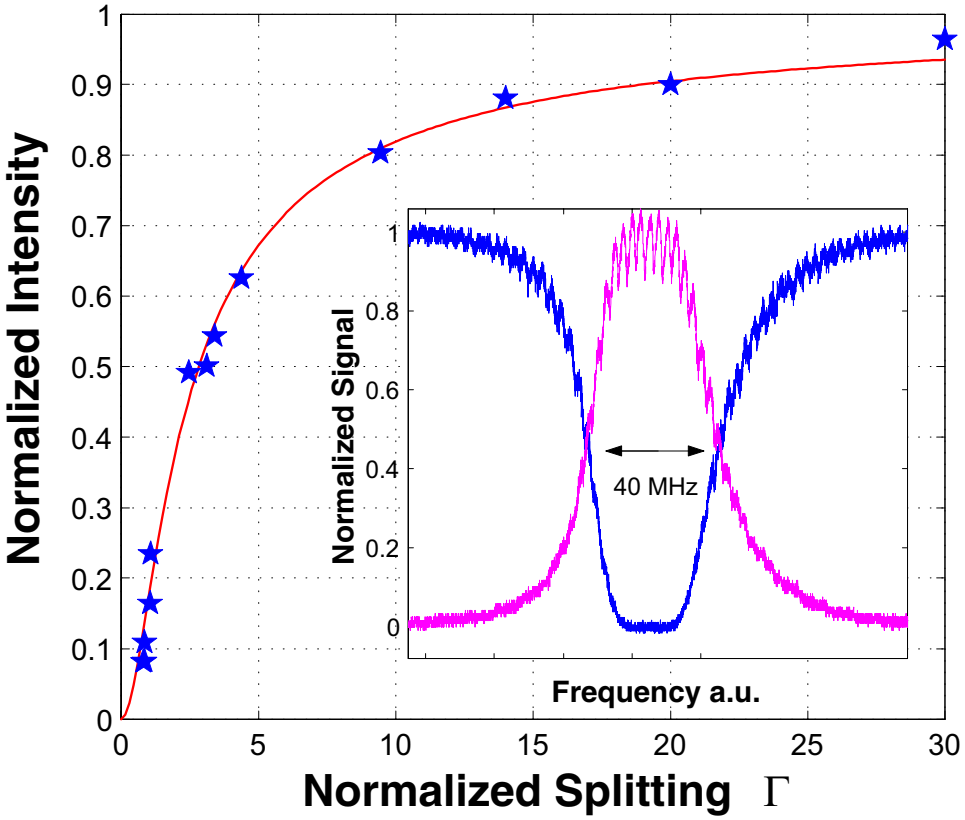

Figure 4.4: Experimentally observed and theoretically determined reflection at the critical point as a function of modal coupling Γ. For large Γ the reflection asymptotically approaches unity. The inset of the figure shows the transmission and reflection at the $T = 0$ point, for a mode having $\Gamma = 31$. In this case 94% of the optical power is reflected. Note that the doublet structure is masked, since the lifetime of the mode is of the same order as the lifetime of the modal coupling process. The presence of modal coupling causes a flattened frequency response at criticality.

ing power coupled back into the direction of the source. We experimentally verified this functional dependence as is shown in figure 4.4. The inset of figure 4.4 illustrates that in the strong modal coupling regime the whispering-gallery-type resonator (in this case a microsphere) behaves like a 'frequency selective reflector'. The highest intermode coupling of $\Gamma = 31$ was observed in a sphere with a diameter of 30 μm. This large modal coupling implies that the probability for scattering a photon into the oppositely oriented mode was 31 times higher than the probability of a photon being lost (absorbed or scattered into nonresonant modes). This surprisingly efficient coupling process can be understood qualitatively by considering the spatial distribution of the mode in the microsphere. Only light which is scattered into an angular segment exceeding the mode's cut-off angle is lost [48], all the remaining light is channeled back into the clockwise and counterclockwise propagating mode, thereby inducing modal coupling. Since the ratio of modal volume (approximately quadratic in radius) and sphere volume increases for smaller spheres, the modal coupling is expected to increase as well. This is in agreement with our experimental findings, since the largest intermode coupling of $\Gamma \approx 30$ was generally only observed in spheres with a diameter of less than approximately 40 μm.

It is important to note that the critical coupling point in the presence of scattering does not correspond to the point of maximum circulating power. In fact, maximum circulating power occurs with finite transmission. We theoretically investigated the shift of the point of maximum power transfer and determined that the largest shift occurs for a modal coupling of $\Gamma = 1.5$ at which it shifts to $K = 1.52$. Interestingly, in the case of large modal coupling ($\Gamma \gg 1$), the maximum power transfer condition approaches the condition $K = 1$, as was the case for weak or no modal coupling ($\Gamma = 0$). The condition $K = 1$ has the special property of causing a transmission and reflection of equal magnitude. In addition the circulating power is reduced in the presence of modal coupling.

Defining a power reduction factor C for the total circulating power, and assuming

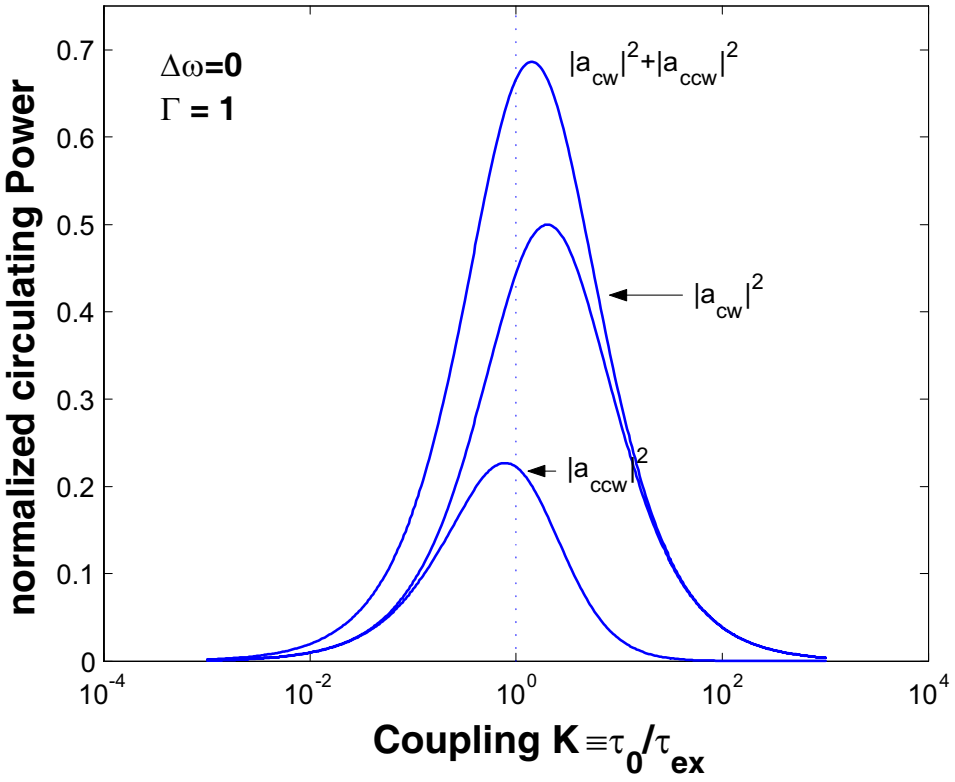

Figure 4.5: Calculation of the resonant circulating power in the microcavity within the microcavity for the case of weak splitting ($\Gamma = 1$) and symmetric excitation $\Delta\omega = 0$ as a function of waveguide-resonator coupling (as defined by equation 4.8). The circulating power in the clockwise ($|a_{cw}|^2$) and counter-clockwise ($|a_{ccw}|^2$) mode is shown, and normalized with respect to the circulating power in the absence of modal coupling ($\Gamma = 0$ case).

that one of the new eigenfrequencies $\omega = \omega_0 \pm \frac{1}{\gamma}$ is excited, C can be written as:

$$C(\Gamma) \equiv \frac{|a_{cw}|_{\gamma}^2 + |a_{ccw}|_{\gamma}^2}{|a_{cw}|_{ideal}^2} = \frac{(2\Gamma^2 + (1+K)^2)^2 + (1+K)^2\,\Gamma^2}{(4\Gamma^2 + (1+K)^2)^2} + \frac{\Gamma^2}{4\Gamma^2 + (1+K)^2} \tag{4.14}$$

The first term on the right hand side is the power contributed by the CW mode and the second term is the power in the CCW direction. In the limit of no scattering ($\Gamma = 0$) one obtains the 'ideal' circulating power, while in the case of large scattering the amount is reduced by a factor of 2. Figure 4.6 shows the fraction of circulating power in the original clockwise and counterclockwise cavity mode as a function of coupling . As evident from the figure, in the undercoupled regime clockwise and counterclockwise mode are excited equally, provided the scattering rate exceeds intrinsic loss rate ($\gamma^{-1} > \tau_0^{-1}$) . As the coupling is increased, a point is reached where the cavity losses (either intrinsic or coupling related) dominate ($\tau_0^{-1} > \gamma^{-1}$). For this case the amplitude of the counter-propagating wave decreases, since the counter-clockwise propagating does not have sufficient time to be build up. In the limit of strong overcoupling, the resonator therefore again approaches the behavior of an ideal traveling wave resonator. The presence of modal coupling and reflection has additionally the important property of reducing the maximum energy storage of the cavity. Figure 4.6 shows the reduction of cavity energy (with respect to the ideal case, i.e. $\Gamma = 0$). In this calculation maximum circulating power was calculated, and compared to the ideal case. In the limit of strong modal coupling the circulating power is reduced by a factor of two. This property will be particularly important in the second part of this thesis, where nonlinear optical effects in microcavities are considered.

4.4 Physical mechanism giving rise to strong modal coupling in micro-sphere resonators

We studied the origin of the scattering amplitudes causing strong modal coupling by analyzing the sphere's surface around the equatorial plane using SEM imaging. It was

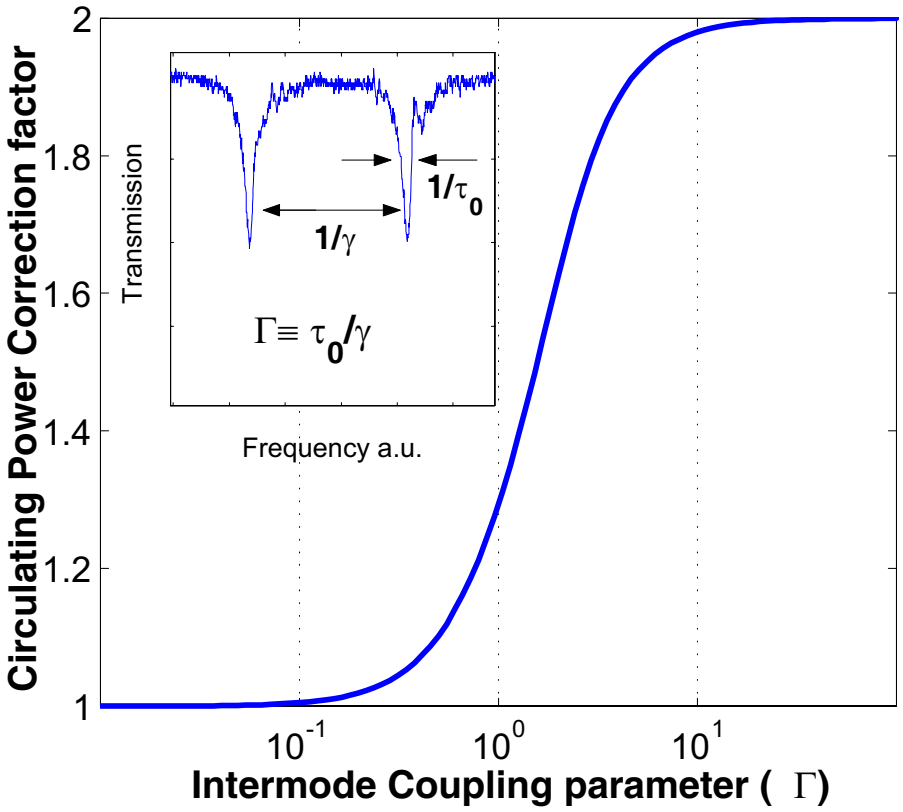

Figure 4.6: Power correction factor as a function of modal coupling parameter Γ. In the case of strong modal coupling ($\Gamma \gg 1$) the maximum Energy stored in the cavity is reduced by a factor of 2. Inset: Doublet structure is evidenced in the transmission.

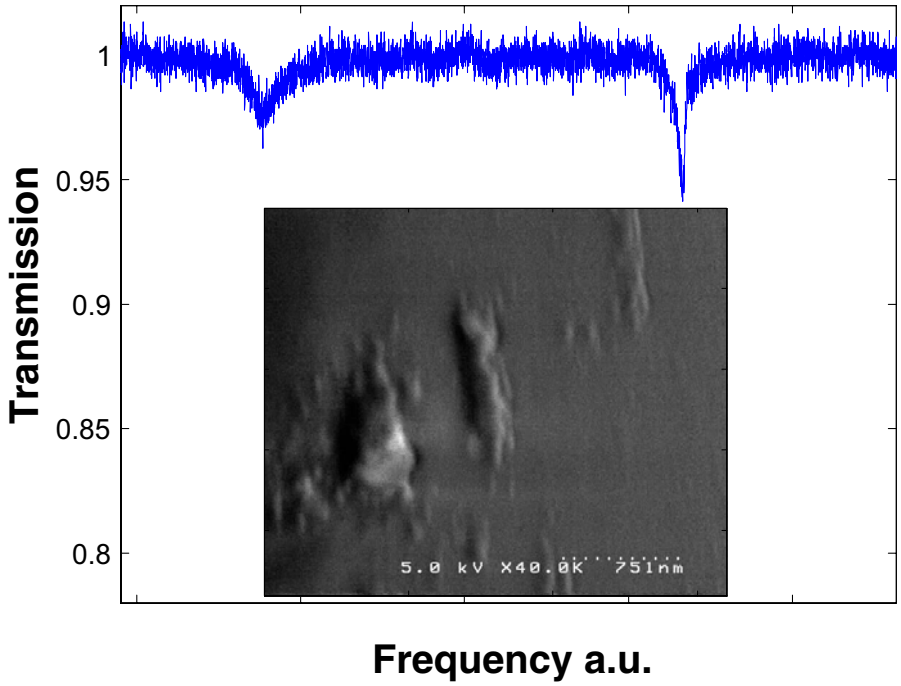

Figure 4.7: Observation of a-symmetric mode splitting. The doublet structure exhibits an a-symmetry in terms of the linewidth and transmission (T). Inset: Scanning electron microscopy of the surface of a microsphere resonator exhibiting strong modal coupling. Surface defect centers with dimensions below the excitation wavelength are visible which can give rise to strong modal coupling. The defects centers are due to evaporation and subsequent redeposition of silica on the sphere surface.

found that for spheres with large intermode coupling, small, localized and randomly distributed surface defects, which had sub-wavelength dimensions (typically hundreds of nanometers as shown in the inset of figure 4.7) were present, while in spheres exhibiting negligible mode splitting these defects were absent. It can be concluded that for the spheres under consideration, the modal coupling was caused by scattering of surface defects. The surface centers are likely due to re-deposition of silica during the CO_2 laser annealing step. As pointed out in Appendix C the laser heating is routinely observed to cause evaporation of silica from the cavity surface.

The sub-wavelength nature of the surface scattering centers can also be a possible explanation for the observation of asymmetric mode splitting. Figure 4.7 shows the observed effect, as evidenced from a transmission spectrum. As the proper eigen-

modes in the presence of (strong) modal coupling are standing waves (with the angular variation $|u|^2 \propto \cos^2(m\phi)$, $\sin^2(m\phi)$) the eigenmodes are orthogonal and sense different parts of the resonator surface and its imperfections. Correspondingly, this can lead to a different loss rate for the two orthogonal pair of standing waves (and correspondingly lead to the asymmetric mode splitting).

4.5 Summary

In conclusion, we have experimentally observed the regime of strong modal coupling, where scattering rate among the degenerate CW and CCW propagating whispering gallery mode is the dominant scattering mechanism and exceeds both intrinsic loss rate as well as the waveguide-coupling rate. We have analyzed the modified coupling properties in the presence of large modal coupling. We observe a shift in the critical coupling point, and a strongly reflected signal. The extent to which the resonator properties are altered can be described by the normalized modal coupling parameter Γ. In the regime of strong modal coupling, back-reflection as large as 94% was observed, and demonstrate that the whispering-gallery mode resonator does not store appreciable optical energy but functions as a 'narrow-band reflector'. The arising modifications of criticality and circulating power are important in cavity QED and nonlinear optical experiments, [49, 40]. The discussed properties are not resonator-type specific and can be found in other resonant geometries, e.g. fiber-rings, planar disks, or cylinders.

Chapter 5

Ultralow-threshold Raman Lasing in spherical microcavities

5.1 Introduction[1]

The long photon lifetimes and small mode volume of ultra-high-Q microcavities, allow to significantly reduce the threshold for nonlinear phenomena. Early work[56][57] recognized these attributes through Raman excitation in microdroplets, and have observed and investigated many stimulated nonlinear phenomena, such as stimulated Brillouin[58], stimulated Raman[59] scattering and cascaded Raman scattering[60] in liquids formed from Raman active media such as Carbondisulfid (CS_2). However, due to the inefficient nature of free space laser excitation used in these experiments, as well as due to the transient nature of the microdroplets, microdroplets required high threshold pump powers and did not allow stable and long term study of nonlinear optical effects. In contrast, silica microspheres (which have first been studied by Ilchenko and Gorodetsky[61]) are good candidates for stimulated Raman sources, and have the highest Q-factors of any optical resonator ($>10^9$). Silica microspheres allow both stable and long term study of nonlinear effects, and can be efficiently excited with tapered optical fibers as studied chapter 3. Despite these favorable properties, however, nonlinear optical phenomena in silica microspheres have remained nearly entirely unexplored, with the with the exception of the Kerr-effect, which was ob-

[1] **Work presented in this chapter has been published in: "Ultra-low threshold Raman laser using a spherical microcavity", *Nature*, 415, 621-623 (2002).**

served in low-temperature experiments as an intensity dependent shift of the resonance wavelength[62]. In this thesis chapter a micrometer-scale, nonlinear Raman source using a taper-fiber coupled microsphere is demonstrated[63] that has a highly efficient pump-signal conversion (higher than 35%) and pump thresholds nearly 1000 times lower than shown before. This reduction of necessary pump power is due the efficient and optimum coupling to ultra-high-Q optical modes. This allows to observe stimulated Raman scattering at threshold levels as low as 65 $\mu Watt$, which is usually considered the regime of linear optics. In contrast, silica-fiber Raman sources used to-date in telecommunication require high power pump lasers (typically with several Watts), and are macro-scale devices. As such, the result presented in this chapter present a route to compact, ultra-low threshold sources for numerous wavelength bands that are usually difficult to access. While ultra-high-Q microsphere enables a large reduction in the necessary threshold pump power, the fiber-coupling notably improves overall efficiency and provides a convenient method of optical field transport.

5.2 Nonlinear optics in fiber

If one wished to study nonlinear optical effects, one would intuitively not choose silica at first sight. Due to the inversion symmetry of the material it does not have a second order nonlinearity $\chi^{(2)}$. The third order nonlinearity $\chi^{(3)}$ of silica is, compared to most other materials, nearly 2-orders of magnitude smaller. However, the low nonlinearity of silica is compensated by the fact that silica possesses low absorption (0.2 dB/km at 1550 nm) yielding a very high nonlinearity-to-loss ratio. This has been recognized by many researchers and makes optical fiber based nonlinear optics a highly attractive and fruitful field of research (A comprehensive overview of quantum and nonlinear optics in fiber is given in ref. [64][65]). On an applied side, optical fiber is the medium of choice for optical field transport and as such bears practical potential.

The nonlinear optical response is in general described by expanding the polariza-

tion in powers of the electric field.

$$P_i = \varepsilon_0 \chi_{ij}^{(1)} E_j + \varepsilon_0 \overline{\chi}_{ijkl}^{(3)} E_j E_k E_l$$

The lowest order nonlinearity in silica is third order[2]. The an-harmonic terms in this expansion of the susceptibility gives rise to a variety of nonlinear optical phenomena, which are explained in Appendix A. The different nonlinear optical effects which can be observed in silica, are associated with different products of the field operators $E_j E_k E_l$ and the respective susceptibility function. In general the third order nonlinearity exhibits both a real and imaginary part:

$$\chi^{(3)} = \chi_{\mathrm{Re}}^{(3)} + i \cdot \chi_{\mathrm{Im}}^{(3)}$$

The third order nonlinearity in silica fiber exhibits both an instantaneous and time delayed response. The instantaneous nonlinear response of silica is determined mainly (81%) by the far-off resonant electronic response from the medium which occurs at a time-scale of $\tau = 5\ fs$. In addition as small part of this instantaneous response (19%) is due to vibrational states (phonons)[64].

5.2.1 Kerr nonlinearity

The instantaneous response of silica gives rise to a change of the refractive index with intensity $n(I) = n_0 + n_2 I$, where $n_2 = 3 \times 10^{-16} cm^2/W$, and is commonly referred to as the optical Kerr effect. As shown in appendix A, it is related to the nonlinear susceptibility by:

$$n_2 = \frac{3}{8nc\epsilon_0} \chi^{(3)}$$

[2] To describe the nonlinear optical response of a medium, the polarization is expanded in a power series of the electric field, i.e.

$$P_i = \varepsilon_0 \chi_{ij}^{(1)} E_j + \varepsilon_0 \overline{\chi_{ijk}}^{(2)} E_j E_k + \varepsilon_0 \overline{\chi}_{ijkl}^{(3)} E_j E_k E_l$$

Due to inversion symmetry of the material (silica), the polarization must transform from $P_i \rightarrow -P_i$ and the electric field as $E_i \rightarrow -E_i$ under spatial inversion. This is only the case if the even terms vanish ($\overline{\chi_{ijk}}^{(2)} \equiv 0$).

As a result a light beam experiences an intensity dependent refractive index, which can be used in a variety of fundamental and applied studies and gives rise to squeezing, solitons, wavelength conversion, pulse compression, optical switching etc. (see references [64][65] for an overview). It should be noted that the imaginary part of n_2, describes two-photon absorption and in the case for silica can be neglected, since resonant processes occur at photon energies of ca. 9 eV.

5.2.2 Raman scattering

In addition to the instantaneous response, there is also a time-delayed response of the medium (which can be modeled as a time-delayed susceptibility function). This non-instantaneous silica response due to vibrations (phonons) gives rise to stimulated Raman scattering. Raman scattering is an inelastic light scattering process which was first observed in 1904 by Raman and Shrinivan. The theory of stimulated Raman scattering was later developed by Bloembergen, and reference [66] contains an excellent treatment on the physics of stimulated Raman scattering. Stokes scattering describes the process where a photon is red-shifted and a phonon created, whereas the reverse process, the absorption of a phonon and the creation of a blue-shifted wave is referred to as anti-Stokes scattering.

In silica stimulated Raman scattering is due to the interaction with optical phonons. Due to the rapid decay of the optical phonons ($\tau \approx 100\ fs$), the treatment of stimulated Raman scattering simplifies considerably, leading to de-coupled Stokes and anti-Stokes fields [66], and leads to Stokes amplification, whereas the anti-Stokes field is attenuated. Stimulated Raman scattering was first observed in optical fibers by Stolen and Ippen at Bell labs (see reference [67][68]). It is important to note, that Raman scattering leads to both forward and backward a scattered Stokes fields. Momentum conversation in this process is intrinsically satisfied, since the dispersion relation $\omega(\left|\vec{k}\right|)$ of optical phonons is essentially flat, and an optical phonon carrying the difference in wave-vector $\Delta\vec{k} = \vec{k}_p - \vec{k}_R$ can be found for both *forward* and *backward* scattered light. Therefore Raman oscillation in a microcavity will excite both

Silica nonlinearity	Frequency Shift (ν_0)	Linewidth ($\Delta\nu$)	Gain-factor (g) (m/W)
Brillouin Scattering	10 GHz	100 MHz	500×10^{-13}
Raman Scattering	14.3 THz	$\approx$10 THz	1×10^{-13}
Kerr-FWM	-	>10 THz	2×10^{-13}

Table 5.1: Nonlinear optical processes of silica and their associated modal gain.

CW and CCW whispering-gallery modes.

5.2.3 Brillouin scattering

In addition the light field can also couple to acoustical phonons which is referred to as Brillouin scattering. This effect has been reported for optical fiber in reference [69]. In contrast to optical phonons, acoustical phonons in silica exhibit a linear dispersion relation $\omega(k) = v \cdot \left|\vec{k}\right|$. Therefore a light wave can only couple efficiently via an acoustical phonon to selected wave-vectors, and gives rise only to backwards light scattering. In addition, the linear dispersion curve leads to a frequency shift much smaller than for optical phonons. Table 5.1 summarizes the characteristic parameters of Brillouin, Raman and Kerr nonlinear optical processes in silica, along with their respective modal gain. It is important to note that the Kerr-effect has a maximum gain which exceed that of Raman by a factor of 2 (This will give rise to parametric oscillation, which is the topic of chapter 10).

5.3 Stimulated Raman scattering in microcavities

In silica, stimulated Raman scattering occurs due to the coupling of a photon to the optical phonons of amorphous silica, and can be described by the third-order nonlinearity, as is described in Appendix A. Figure 5.1 shows the Raman gain spectrum as a function of phonon frequency for silica glass.

In a microcavity stimulated Raman scattering can occur when both energy and momentum conservation among the pump photon, scattered photon and phonon are

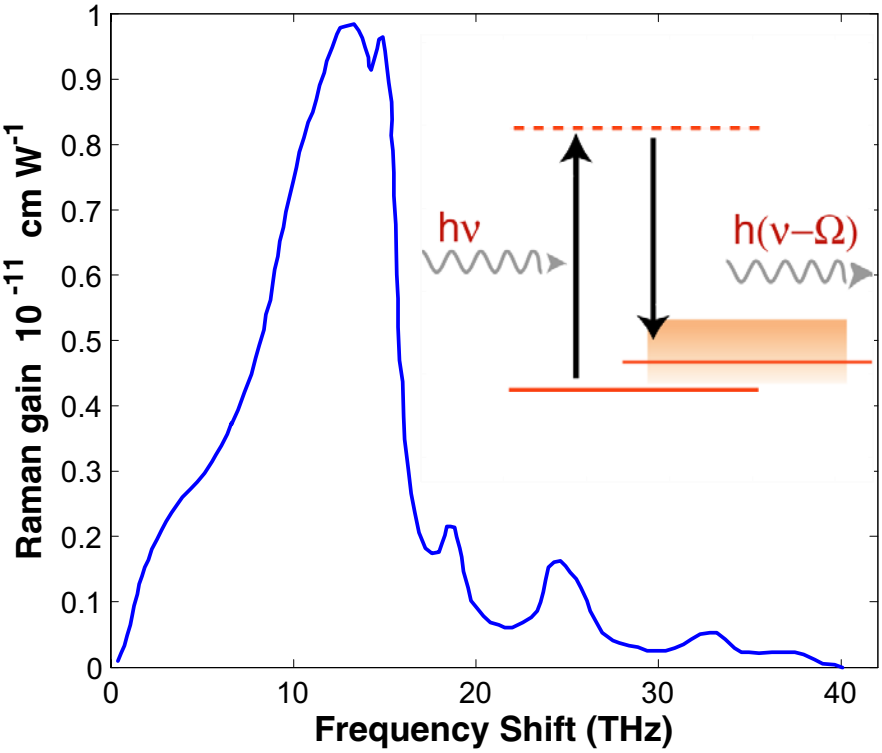

Figure 5.1: Raman gain spectrum of SiO_2. The peak gain occurs at 14.3 THz and 13.9 THz. The broad nature of the Raman gain spectra is due to the rapid de-phasing of the phonons, which occurs on the order of 10 ps. The inset shows the schematic of the light-phonon interaction which gives rise to a red-shifted photon, where the difference in energy is carried by the phonon field.

obeyed. Momentum conservation is intrinsically satisfied, due to the essentially flat dispersion relation of optical phonons. Due to the broad nature of the Raman gain spectrum, the resonance condition (i.e. energy conservation) for a Raman mode is strongly relaxed, as for the microcavities considered in this thesis, the number of modes under the Raman gain curve is typically $\gg 1$ (i.e. since the free-spectral-range is much less than 30 THz), and accidental overlap is in all experimental scenarios guaranteed. In addition the Stokes amplification is a phase insensitive amplification scheme, and therefore phase-matching of pump and Raman mode intrinsically satisfied.

The lasing threshold occurs when cavity round-trip gain equals round-trip loss. For an intensity-dependent gain coefficient (such as for a stimulated Raman scattering), and taking into account the power build-up factor in a resonator, the following equation for threshold pump power can be derived;

$$P_{threshold} = \frac{\pi^2 n^2 V_{eff}}{\lambda_P \lambda_R C(\Gamma) g_R^B} Q_e^P \left(\frac{1}{Q_T^P}\right)^2 \frac{1}{Q_T^R} \tag{5.1}$$

Here $P_{threshold}$ denotes the incident power necessary in the fiber (not the power coupled into the resonator), n is the index of refraction, V_{eff} is the effective pump mode volume (i.e. which will be explained in detail in the next chapter), λ_P and λ_R are the pump and Raman wavelengths, g_R^b is the nonlinear bulk Raman gain coefficient, $C(\Gamma)$ is a correction factor of the circulating power due to internal backscattering (between 1 and 2), and Q_T^p is the total quality factor for the pump mode, made up of an intrinsic contribution Q_o^p and a coupling contribution Q_e^p (and similarly for the Raman mode). Equation (1) has the important feature that the threshold pump power scales inversely with the factor V/Q^2, which is the same as quality factor multiplied by the cavity Purcell factor ($\propto Q/V$). Thus quality factor plays a dominant role in device performance. This is a classical conclusion, neglecting the possible additional benefit due to enhancement of the gain coefficient by cavity quantum electrodynamics (QED)[70]. As a result the ultra-high-Q modes of microspheres, should enable significant reduction in the necessary pump power required for stimulated Raman

Substance	Raman Shift (ν_0) cm^{-1}	Linewidth($\Delta\nu$) cm^{-1}	Raman–gain (g) (m/W)
Silica SiO_2	467		0.8×10^{-11}
CS_2	665	0.5	24×10^{-11}
$LiNbO_3$	256/637	23/20	$8.9/9.4\times10^{-11}$

Table 5.2: Comparison of the Raman properties for the substances used in cavity nonlinear optical experiments using microdroplets and microspheres.

scattering, which is indeed experimentally observed as will be described in the next section.

5.4 Observation of stimulated Raman scattering in microspheres

Silica microspheres were fabricated as described in chapter 2 of this thesis by melting the tip of a standard telecommunication (SMF-28) fiber with a CO_2 laser, and coupled using tapered optical fiber. In these measurements, values of Q were in the low 10^8 range, believed to be limited by surface scattering and OH absorption[71]. Surface scattering also induces backscattering of power and couples the initially degenerate clockwise (CW) and counter-clockwise (CCW) circulating modes, causing a splitting of the resonance wavelength, which has been observed earlier in microspheres[72]. In addition, as discussed in chapter 4, there is an associated reduction of the circulating power due, compared to the case of no backscattering (up to a factor of two). The taper position is controlled relative to the microsphere by a three-axis stage with a resolution of 20 nm. A tunable 1550-nm external-cavity diode laser with 300 kHz linewidth is used as a pump. The laser is scanned repeatedly through a frequency range of approximately 60 GHz around a single whispering gallery mode (WGM).

Figure 5.2 shows the emission spectrum for a Raman microsphere laser (intrinsic pump quality factor of $Q_o = 10^8$) excited far above the threshold for stimulated Raman scattering. There are a multitude of nonlinearly generated wavelengths, from

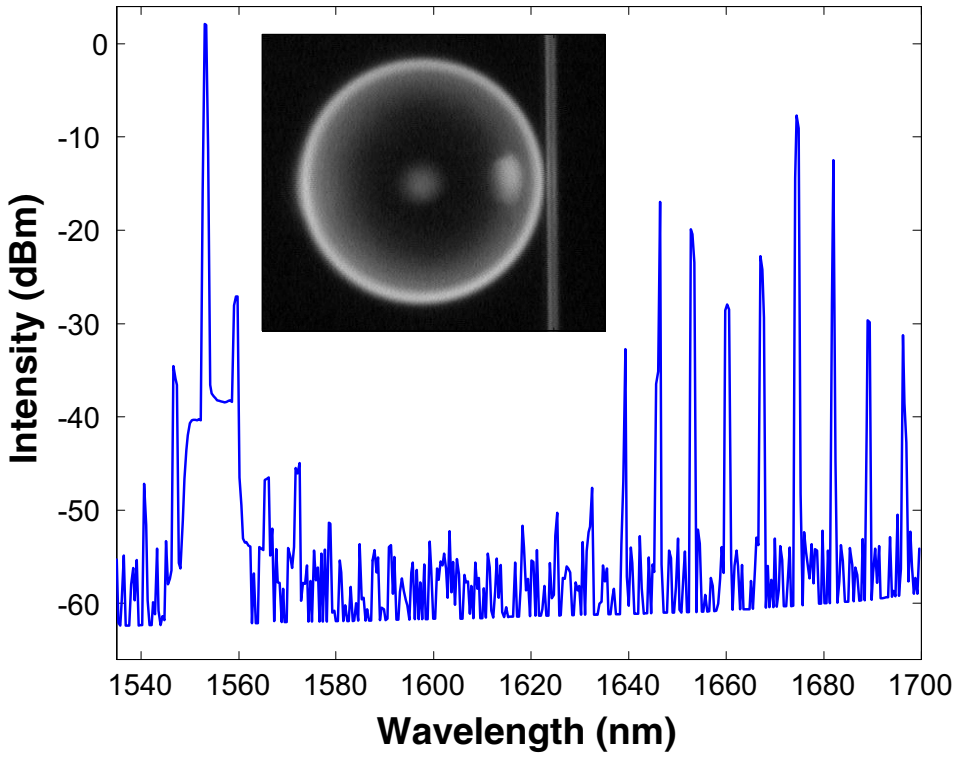

Figure 5.2: Spectrum of a 70-μm diameter Raman microsphere laser with pump powers of 2 mW. The pump is at 1555 nm. The peaks located around 1670 nm are Raman oscillation, separated by the free-spectral-range (here about 5 nm) of the microsphere. The secondary lines around 1555 nm are due to four-wave-mixing (FWM) between the pump and two Raman waves. Inset is a microsphere coupled to a fiber taper.

stimulated Raman peaks centered around 1670 nm to Raman-assisted four-wave mixing (FWM) peaks located symmetrically about the 1550-nm pump. Stimulated Raman scattering has a very high threshold (nonlinear gain coefficient of 10^{-11} cm/W), requiring significant circulating pump powers. This suggests that other nonlinear processes having lower thresholds such as stimulated Brillouin scattering (SBS) could also be present in the systems tested. SBS, for example, should have a threshold roughly 500 times lower than stimulated Raman scattering (nonlinear gain coefficient is 500 times larger). To determine the presence of SBS, an optical spectrum analyzer was used to measure backward propagating optical power coupled from the micro-resonator into the fiber taper. The gain spectrum for SBS is very narrow (< 10 MHz) with a roughly 10 GHz frequency downshift in silica. The micro-resonators tested here have free spectral ranges on the order of teraHertz (the angular mode number was in the range of $50 \lesssim \ell \lesssim 200$), with an eccentricity splitting of the azimuthal modes on the gigahertz scale (i.e. $|\Delta\nu_{ecc}| = \nu \cdot \epsilon \frac{|m|+\frac{1}{2}}{\ell^2}$,corresponding to an eccentricity of the order of $\epsilon \lesssim 1\%$. In general this splitting is dependent upon fabrication-induced irregularities, thus overlap with the SBS spectrum is unlikely. Accidental overlap with the Brillouin gain spectrum has been observed in experiments on liquid droplets[58], but has not been observed in the microspheres used in this study. In addition, it is worth noting that Brillouin scattering in silica fiber leads to the deviation from the Brillouin theory, since the acoustical wave depart from their plane wave nature (underlying the conventional Brillouin scattering treatment) as they are eigenmodes of the cylindrical fiber structure. This leads to the case of forward acoustic wave scattering (guided acoustic wave Brillouin scattering)[73][74], which is due to acoustical modes which have zero wave-vector parallel to the axis of propagation, but non-zero frequency[3]. However, the backward spectral monitor did show the expected strong Raman oscillation. Cascaded Raman peaks, if present, were not observable due to the wavelength range of the optical spectrum analyzer (and are analyzed in a different experiment using a 1450 nm pump as described in the next thesis chapter). Note that

[3]Frequency components (typically $2\times\Delta v, \Delta v$) which might indeed be attributed to forward-wave acoustic Brillouin scattering have been observed in certain cases (for frequency shifts $\Delta v \approx 5$ MHz, which were smaller than the cavity linewidth).

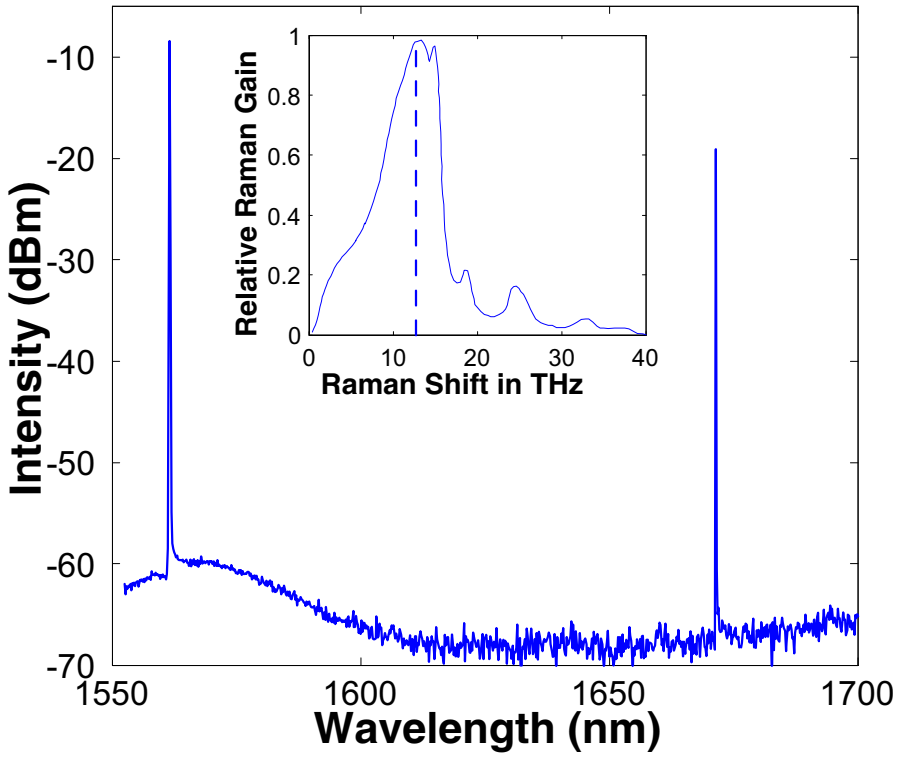

Figure 5.3: Single longitudinal mode Raman lasing. Raman spectrum for a 40-μm diameter microsphere, exhibiting a uni-directional conversion efficiency of 16% (pump is at 1555 nm).

four-wave-mixing associated with the Kerr effect was also observed. However, such processes in micro-cavities are governed by strict conditions imposed by the combined effect of the phase-matching requirement with the WGM spectral structure. This will be investigated in future work, and the results of this study are presented in the last chapter of this thesis.

Stimulated Raman oscillation was observed by pumping a single WGM and monitoring the transmission using an optical spectrum analyzer. Once the threshold for SRS was exceeded, lasing modes in the 1650-nm band could be observed, in correspondence with the peak Raman gain which occurs down-shifted in frequency by approximately 14 THz relative to the pump frequency (wavelength shift of approximately 110 nm). Figure 5.3 shows Raman emission for an ultra-high-Q microsphere. The Raman emission with respect to the gain peak is provided in the inset of figure

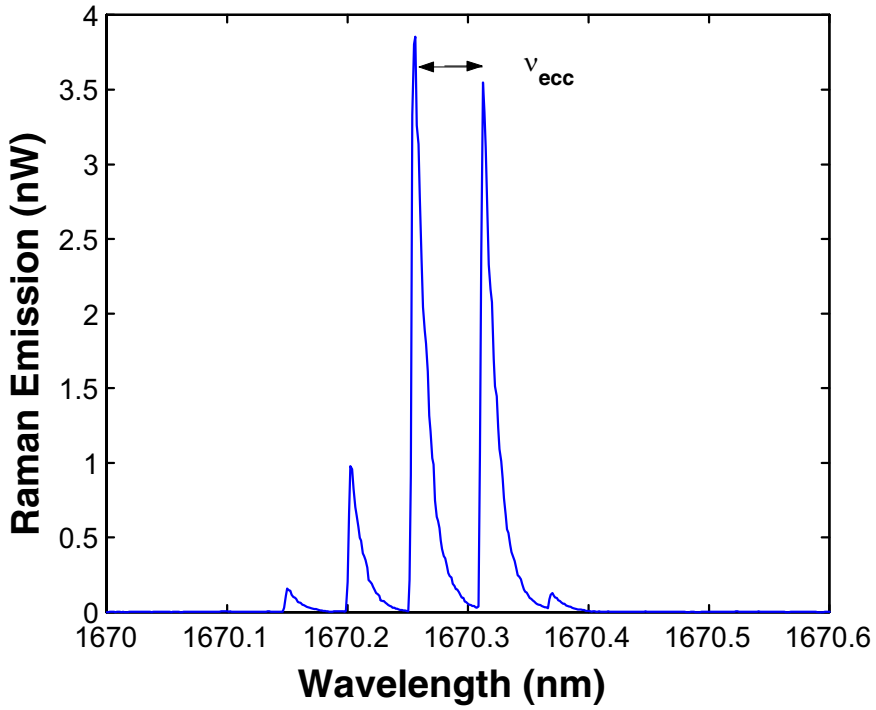

Figure 5.4: High resolution scan of the Raman output emission slightly above threshold from the previous figure, exhibiting 5 oscillating azimuthal modes (identified as $\ell = m, ..., \ell = m - 4$) where $\ell \approx 150$. The modes are split due to eccentricity by $|\Delta\nu_{ecc}| \approx 7.5$ GHz which corresponds to an eccentricity of $\epsilon \approx \frac{|\Delta\nu_{ecc}|}{\nu}\ell \approx 0.06\%$.

5.3 . Since the fundamental whispering gallery modes ($n = 1, \ell = m, p = TM$) are most tightly confined (i.e., smallest mode volume), Raman lasing is expected to occur first for these modes. The presence of nearly degenerate azimuthal modes in a spherical microcavity (i.e., weak eccentricity splitting), causes simultaneous oscillation on several azimuthal modes. Figure 5.4 shows a higher resolution spectral scan of the spectrum in figure 5.4. Several azimuthal modes can be observed to be oscillating simultaneously (to the temporal resolution of the optical spectrum analyzer). The splitting of the modes is for fundamental WGM ($n = 1$, $\ell \approx m$) is given by (compare chapter 1):

$$|\Delta\lambda_{ecc}| \approx \lambda \cdot \epsilon \frac{1}{\ell} \tag{5.2}$$

And corresponds to an eccentricity of $\epsilon \approx 0.06\%$. The efficiency of the Raman oscillator was investigated by decreasing the pump power until a single emission wavelength was observed on the optical spectrum analyzer (inset of figure 5.5). The measured threshold is 86 μW for this 40-μm sphere. This value is nearly 1000$\times$ lower than the corresponding values measured in previous work using microdroplets (45 mW for a 30-μm CS_2 droplet; ref. [57]), despite the fact that silica has a 1000 times lower Raman gain coefficient (compare table5.2). This improvement of nearly 10^6 times lower threshold results from efficient single WGM excitation and controlled coupling, whereas free space beams (used previously) lack high spatial mode selectivity and efficient power transfer. The measured unidirectional absolute conversion efficiency was 16%, with a differential quantum efficiency (CW and CCW oscillation) of 36%. In other microspheres tested Raman output powers as large as 200 μW have been obtained.

5.4.1 Coupling dependence of stimulated Raman threshold

The threshold formula predicts a strong dependence of the threshold on the coupling dependence. To investigate the dependence on quality factor, the threshold was measured while varying the coupling between the taper and microsphere by changing the air gap (compare figure 5.5). The data follow a near parabolic shape with a

measured minimum value of 62 μW. This value is, to the author's best knowledge, the lowest directly measured (not inferred) Raman threshold for any nonlinear substance to date. A theoretical fit, based on exponential dependence of the coupling Q, shows excellent agreement.

As a further verification of the threshold formula the theoretical minimum threshold value was compared with the observed value. The quality factor and the mode splitting of the whispering-gallery mode were measured by performing a linewidth sweep in the undercoupled regime, where the backscattering-induced doublet structure is most pronounced. These measurements yielded $Q_0 = 1 \times 10^8$ and $\Gamma = 2$. The size of the microsphere was inferred from the free spectral range, $\Delta\lambda = 10.5$ nm i.e. 50 μm diameter, where the free-spectral range denotes here modes with successive angular mode number ℓ. The mode volume was calculated using analytic expressions based on estimated mode numbers for the fundamental WGM ($n = 1, p = TM, m = \ell, \ell \approx 139$). Numerical Calculations yield a modal volume of ca. 1300 μm^3. Using these values, the theoretically expected minimum threshold is given by 50 $\mu Watts$ which is in good agreement with the experimentally measured value of 62 $\mu Watts$.

Figure 5.6 shows the measured pump threshold plotted versus the transmission for the data of figure 5.5. Note that the graph is not single-valued as the transmission in over and under-coupled regime take identical values. As evident from the measurement, the Raman threshold is always lower in the undercoupled regime, due to the $1/Q^2$-dependence of the Raman threshold. The minimum threshold (marked by the arrow) does not lie at the critical coupling point[75], where circulating pump power (and correspondingly Raman gain) is largest. It in fact occurs for the system in a slightly undercoupled state (weaker cavity coupling rate than at the critical point), corresponding to an observed pump transmission of 12%. This shift results from the interplay between Raman gain and loss, resulting from the coupling of both the pump and Raman wave to the fiber waveguide, and will be explained in more detail in the next thesis chapter. In the simplified case where the quality factors of pump and oscillating modes are equal the theoretical minimum occurs for a pump power

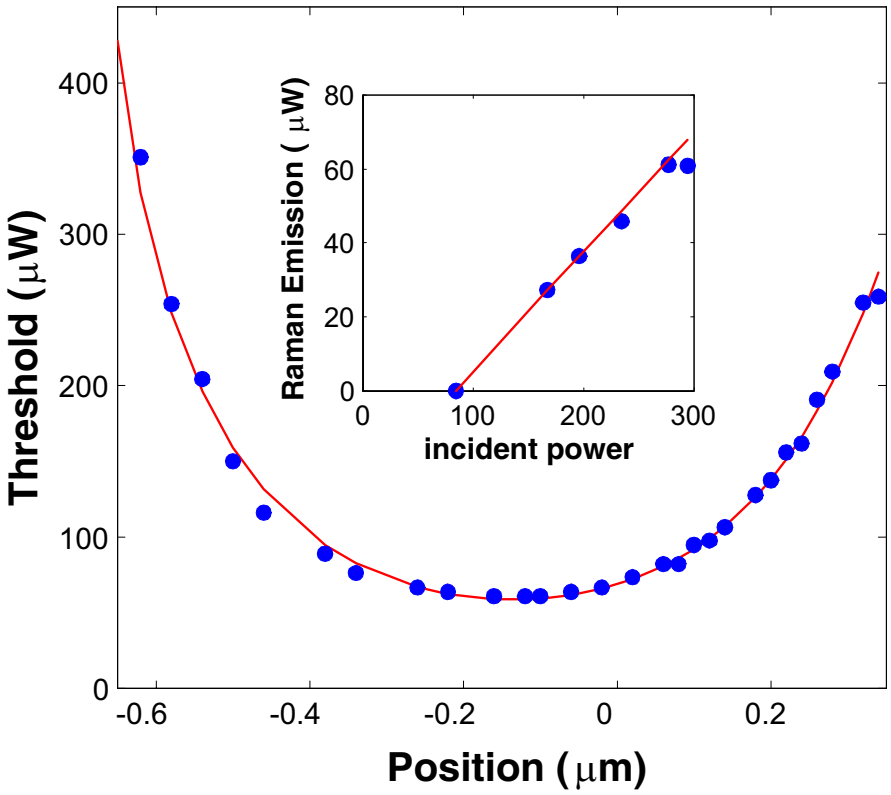

Figure 5.5: Coupling gap and size dependence of the Raman threshold. Main figure, Raman oscillation threshold vs. taper-sphere gap for a 40-μm-diameter sphere (Q_0=10^8). Position is measured from the critical coupling point, where negative values correspond to the undercoupled regime. The minimum threshold occurs with the microsphere about 0.15 μm undercoupled, and corresponds to a transmission of 12%. Solid line, a theoretical fit to the threshold equation. Inset shows Raman power output (sum of forward and backward emission) vs. incident pump power. Differential quantum efficiency is 36%.

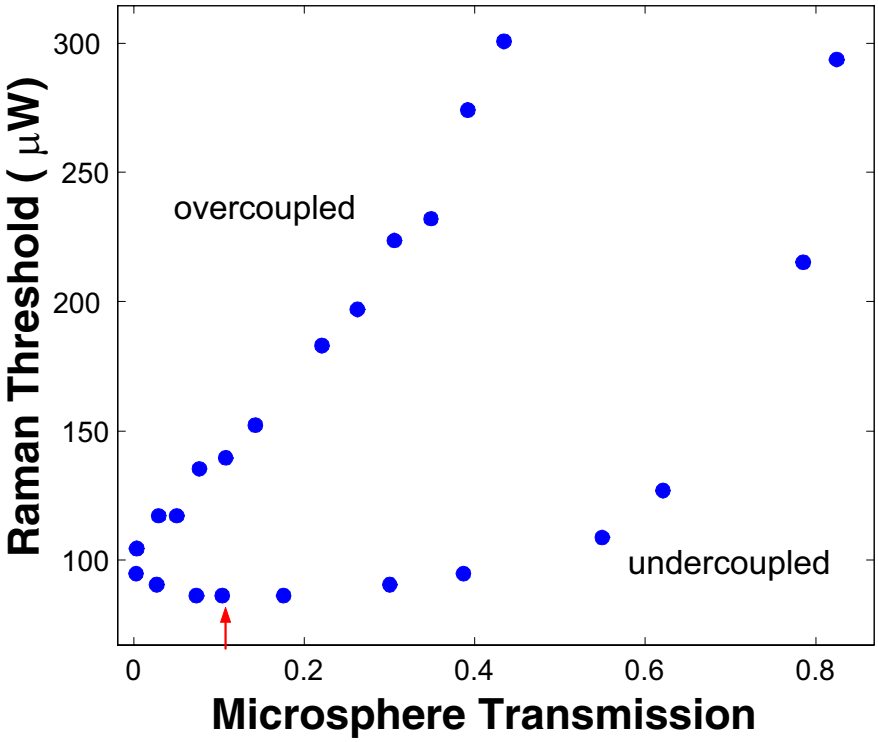

Figure 5.6: Stimulated Raman scattering threshold versus transmission past the microsphere, for the measurement presented in figure 5.5. Since the cavity transmission is a symmetric function with respect to the critical coupling point, the threshold data plotted is not single-valued, and under- and over-coupled regime are indicated in the figure. The arrow denoted the minimum Raman threshold, which occured undercoupled with a finite pump transmission of ca. 12% in agreement with the prediction of the threshold equation (under equal pump and Raman Q).

transmission of $T = 1/9 = 11\%$, and is in good agreement with the measurement.

5.4.2 Mode volume dependence of the Raman threshold

From equation 5.1, the threshold is expected to scale linearly with the mode volume. The inset of figure 5.7shows numerically calculated mode volume for a fundamental mode of a microsphere at 1550 nm. For a microsphere, the mode volume scales approximately as radius squared. Therefore the Raman threshold is expected to exhibit approximately an R^2 behavior on Raman threshold. To investigate this, the minimum threshold for various sphere diameters ranging from 28 to 110 μm was measured. In this experiment, the minimum Raman threshold $P_t^{\min}$, the microsphere size (as inferred from the free-spectral-range), the intrinsic Q in the pump band (Q_0) and the intermode coupling parameter (Γ) were measured. To extract the volumetric dependence of the Raman threshold using data from cavities having different resonant characteristics, the threshold data were normalized to the set of parameters ($Q_0 = 10^8, \Gamma = 0, g_R = g_R^{\max}$). The result of this procedure is shown in the main figure 5.7. The data indeed show a quadratic dependence on R (the actual fitted exponential from a double logarithmic plot is 1.95 and is in good agreement with the expected value of 1.83) and confirm the linear relationship of the Raman threshold on the mode volume as predicted by equation 5.1. It should be noted that for smaller spheres the mode volume deviates from this R^2-behavior and ultimately, since for very small diameters, the mode volume increases due to weakening of the whispering gallery confinement. The minimum mode volume occurs for a radius of $6.9\mu m$ (for $\ell = m = 34$)[76] for 1550 nm wavelength and the mode volume is $V_{\min} = 173.1\mu m^3$. However, this size is not optimum for stimulated Raman scattering as the additional benefit of reduced mode volume is more than offset by the significant decrease in Q factor to ~10^5 due to whispering-gallery loss (Threshold power $\propto V/Q^2$). In previous work on microdroplets, it was found that for droplets with diameters of less than 30 μm there is an additional threshold reduction due to cavity QED effects[70]. In the present work we could not accurately determine threshold in this size range. Smaller

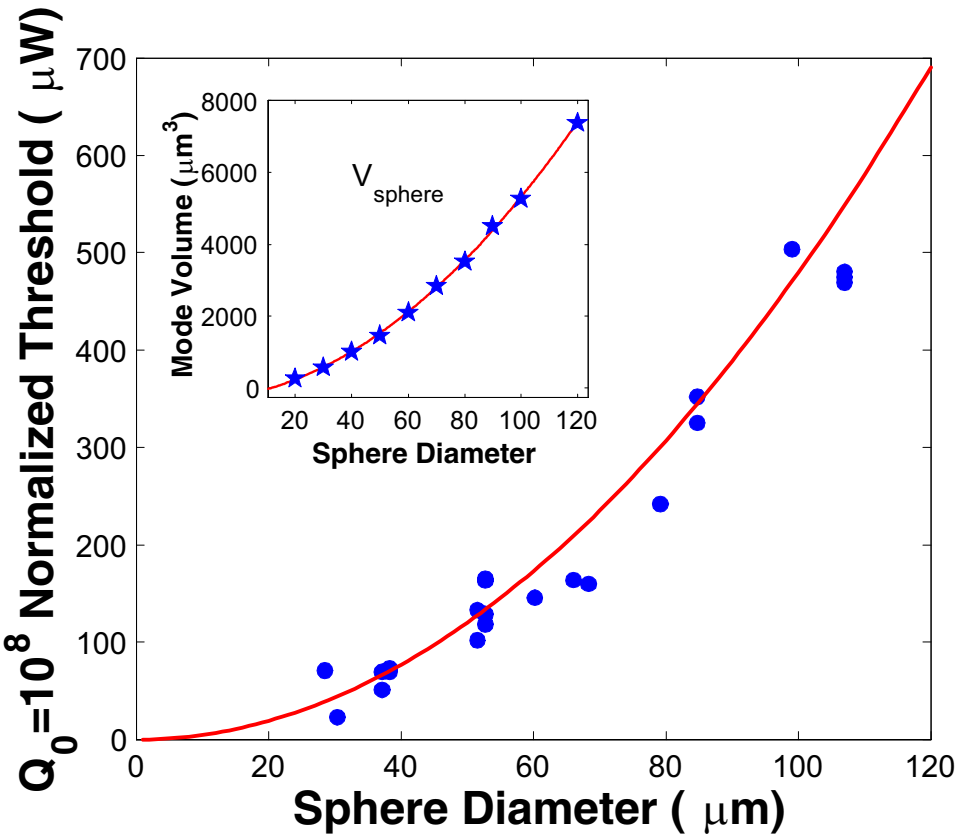

Figure 5.7: The Raman oscillation pump threshold of a microsphere as a function microsphere diameter. To compare microspheres with different resonance characteristics, the Raman threshold was Q-normalized to $Q = 1.0 \times 10^8$ and modal coupling normalized to $\Gamma = 0$. A double logarithmic plot of the data with a linear fit obtains a dependence of $P_{thresh} \propto R^{1.95}$ which is in close agreement with the theoretically expected dependence of $V_{eff} \propto R^{1.83}$. The inset shows the calculated mode volume of a microsphere as a function of diameter using a finite-element solver.

spheres experienced very large temperature effects, causing the WGM's to experience instabilities as well as thermal shifting of the spectrum, complicating pumping of the resonant mode. With sufficient thermal control it may be possible to quantify precisely the reduction of threshold in this smaller size regime.

5.5 Conclusion

There are several ways to improve the performance of this system. Quality factors of 10^9 have been achieved previously in fused-silica microspheres[71], which should lead to sub-microwatt Raman thresholds. The use of small spheres (provided temperature issues can be resolved) should improve Raman conversion efficiencies under increased pump power due to the increase in free spectral range, which decreases the efficiency of secondary Raman lines and Raman-assisted four-wave-mixing. Planar microcavities, such as disks should allow true single-mode emission, and in fact were also demonstrated in this thesis, using toroid microcavities (see chapter 9).

Concerning the outlook for future work and the implications of this work beyond an ultra-efficient and compact Raman source: As noted earlier, Raman and four-wave-mixing in these systems have been observed. These non-linearities can be accessed in a compact volume through a nearly ideal field transport channel (optical fiber) and field coupling junction (the tapered optical fiber). As such, this system can be viewed more broadly as a building block for study of a host of nonlinearity within a high-Q silica resonator and potentially for generation of non-classical photon states[77][64] and their efficient transport. Indeed, the compact nature of the system combined with the potential of fiber field transport could afford relatively straightforward access to resonant systems in normally challenging environments such as ultra-low-T chambers[62]. The ability to load or suitably modify spheres using dopants or quantum dots could also be useful in such studies.

Chapter 6

Theoretical and experimental analysis of cascaded Raman scattering in ultra-high-Q microcavities

6.1 Introduction[1]

In the previous chapter stimulated Raman lasing was observed in fiber coupled microsphere resonators at ultra-low threshold and high efficiency. Due to the high conversion efficiency the internal Raman fields can reach power levels which are sufficient to generate higher order Raman fields. This process, which is referred to as cascaded Raman scattering, is described in this chapter and analyzed both theoretically and experimentally. Cascaded Raman scattering in liquid microdroplets has been observed up to 14^{th} order, but in these studies the characteristics of the pump-to-Raman conversion could not be studied. In this chapter cascaded Raman scattering in microspheres is observed and the pump-to-Raman characteristics measured. Theoretical analysis shows that the generated higher order Raman fields exhibit distinct characteristics on their order. Even order Raman fields exhibit a linear pump-to-Raman conversion, while odd order exhibit a square-root pump to Raman conversion efficiency. Further-

[1] **Work in this chapter has been published in: "Fiber-coupled cascaded Raman laser", Optics Letters, 2003 and "Theoretical and Experimental Analysis of Stimulated Raman scattering in ultra-high-Q optical microcavities", submitted (JSTQE).**

more scaling-laws underlying the cascaded Raman process are derived. The threshold for $N^{th}-$order cascaded Raman modes is shown to follow a N^3-dependence, whereas the efficiency decreases with Stokes order as $1/N^2$. The theoretical findings are in good agreement with measurements up to second order Raman modes, and have also been confirmed beyond second order Raman scattering by Bumki Min [29], who verified the pump threshold and efficiency relation up to 5 orders in microspheres[29], using a 980-nm-wavelength pump laser. Furthermore, the first section will present the coupled-wave equations for Raman lasing in a waveguide-coupled whispering-gallery-mode resonator, and complements the experimental results discussed in the previous chapter. The nonlinear processes can be conveniently described using the coupling-of-modes formalism of chapter 2, by properly defining the (intra-cavity) Raman gain coefficient. Using this set of equations, the expression for the threshold and the efficiency of stimulated Raman scattering is derived and the optimum coupling (minimum Raman threshold) analyzed. The analysis is then extended to the case of cascaded Raman oscillation in which Raman signals serve to pump and generate higher-order Raman waves.

6.2 Theoretical analysis of stimulated Raman scattering in microcavities

6.2.1 Coupled-mode equations for 1^{st} order Raman scattering in microcavities

The classical coupled-wave-equations for stimulated Raman scattering have been given by several authors. In the conventional treatments, the pump and Raman waves are assumed to be plane waves, with only one spatially varying variable, simplifying considerably the coupled wave-equations. In the case of a microcavity, the fields involved are the whispering-gallery modes. By reformulating the wave-equation one arrives at a similar set of equations as in the case of plane waves, however with

modified coupling coefficients, which take into account the coupling among different WG-modes. This treatment leads to the definition of overlap factors (or alternatively stated to the definition of the effective mode area, or effective mode volume). The plane wave interaction is described by:

$$\begin{aligned} \frac{d}{dz}I_p &= -\left(\frac{\omega_p}{\omega_R}\right) g_R I_R I_p \\ \frac{d}{dz}I_R &= g_P I_p I_R \end{aligned}$$

In these equations[2] the bulk Raman gain coefficient is given by g_R and is well known for silica fibers. The equations can also be formulated in terms of the electric field which is related to the field strength by: $I = \frac{1}{2} n \epsilon_o c \left|E\right|^2$.

$$\begin{aligned} \frac{d}{dz}\overrightarrow{E}_p &= -\frac{1}{2}\left(\frac{\omega_p}{\omega_R}\right)\left(\frac{c}{n_{eff}}\right) g_R \left|\overrightarrow{E}_R\right|^2 \overrightarrow{E}_p \\ \frac{d}{dz}\overrightarrow{E}_R &= \frac{1}{2} g_R \left(\frac{c}{n_{eff}}\right) \left|\overrightarrow{E}_p\right|^2 \overrightarrow{E}_R \end{aligned}$$

To connect these equations with the previously introduced model of a WGM microcavity-waveguide system, the slowly varying amplitude (cavity excitation) $A_i(t)$ is introduced. Furthermore, to facilitate the discussion, the amplitude is normalized to yield the electromagnetic energy of the whispering gallery mode, $\left|A_i\right|^2 = U_{WGM}$.

$$\vec{E}_i(r, z, \phi, t) = \frac{1}{\sqrt{N_i}} A_i(t) \cdot \vec{E}(r, z) e^{i\omega_i t - i m_i \phi}$$

where

$$N_i \equiv \int \left|\vec{E}_i\right|^2 dV = 2\pi \int \left|\vec{E}_i\right|^2 dA$$

[2]The factor $\left(\frac{\omega_p}{\omega_R}\right)$ reflects conservation of photon number in the Raman process, i.e. $\frac{d}{dz}(\frac{I_p}{\hbar\omega_p} - \frac{I_R}{\hbar\omega_R}) = 0$. (termed Manley-Rowe relations).

Inserting these solutions into the coupled mode equation (and reformulated in the temporal domain) leads to:

$$\begin{aligned}\left(\frac{c}{n_{eff}}\right)^{-1}\frac{dA_p}{dt}\vec{E}_p &= -\frac{\omega_p}{\omega_R}g_R(\omega_{p,}\omega_R)\left(\frac{c}{n_{eff}}\right)\left|\vec{E}_R\right|^2\vec{E}_p\cdot|A_R|^2A_p\frac{1}{N_R}\\ \left(\frac{c}{n_{eff}}\right)^{-1}\frac{dA_R}{dt}\vec{E}_R &= g_R^c(\omega_p,\omega_R)\left(\frac{c}{n_{eff}}\right)\left|\vec{E}_p\right|^2\vec{E}_R\cdot|A_P|^2A_R\frac{1}{N_p}\end{aligned} \tag{6.1}$$

Next, in order to eliminate the explicitly appearing field dependence $\vec{E}_i$, and to arrive at an equation which describes the evolution of the energy of the pump ($|A_p|^2$) and Raman modes($|A_R|^2$), the equation is multiplied by the operator $\int E_{R,p}^* dV$ from the left. This reduces the explicit field dependence as entered through $E_{p,R} = E_{p,R}(r,z,\phi)$ to an overlap factor, which is the effective mode are of the nonlinear process.

$$\begin{aligned}\frac{dA_p}{dt} &= -\frac{\omega_p}{\omega_R}g_R(\omega_{p,}\omega_R)\left(\frac{c}{n_{eff}}\right)^2V_{eff}\cdot|A_R|^2A_p\\ \frac{dA_R}{dt} &= g_R^c(\omega_p,\omega_R)\left(\frac{c}{n_{eff}}\right)^2V_{eff}\cdot|A_P|^2A_R\\ V_{eff}^{-1} &= \frac{\int|E_p|^2|E_R|^2dV}{\int|E_p|^2dV\int|E_R|^2dV}\end{aligned} \tag{6.2}$$

Since the reformulated equations are now compatible with the coupling-of-modes formalism (for the treatment of the whispering-gallery coupling junction), one can proceed and add waveguide coupling and intrinsic loss terms, as has been done in chapter 2:

$$\begin{aligned}\frac{dA_p}{dt} &= -\left(\frac{1}{2\tau_{ex}}+\frac{1}{2\tau_0}\right)_pA_p-\left(\frac{\omega_p}{\omega_R}\right)g_R(\omega_{p,}\omega_R)\frac{c^2}{2n_{eff}^2}V_{eff}\cdot|A_R|^2A_p+\sqrt{\frac{1}{\tau_{ex}}}s\\ \frac{dA_R}{dt} &= -\left(\frac{1}{2\tau_{ex}}+\frac{1}{2\tau_0}\right)_RA_R+g_R^c(\omega_p,\omega_R)\frac{c^2}{2n_{eff}^2}V_{eff}\cdot|A_P|^2A_R\\ V_{eff}^{-1} &\equiv \frac{\int_{V_{cav}}|E_p|^2|E_R|^2dV}{\int dV|E_R|^2\cdot\int|E_p|^2dV}\end{aligned} \tag{6.3}$$

Three comments are in place. First, it should be noted that the Raman gain will excite both CW and CCW Raman modes of the resonator. For simplicity of discussion the two modes are here described by only one amplitude, such that $|A_R|^2 = |A_R^{ccw}|^2 + |A_R^{cw}|^2$. Therefore, equal amplitude emission occurs along both waveguide directions given by $|s_r|^2 = \frac{|A_R|^2}{2\tau_{ex}}$. Secondarily, modal coupling is generally present in the UHQ WG-resonators, exciting both CW and CCW pump modes, as described by a coupled set of equations as in chapter 4. The treatment of modal coupling in the case of stimulated Raman scattering can however be simplified, by treating the total pump field $|A_p|^2 = \left|A_p^{ccw}\right|^2 + \left|A_p^{cw}\right|^2$. The reduction in total circulating power due to modal coupling $C(\Gamma)$, can be taken into account power by redefining an equivalently reduced Raman gain (i.e. by a factor of $1/C(\Gamma)$). Thirdly, other nonlinear effects such as Four-wave-mixing or Brillouin scattering are not considered in this analysis as the microcavity poses stringent frequency matching constraints on these processes making their observation difficult. In the case of Stimulated Brillouin Scattering, the narrow gain bandwidth in the range of 100 MHZ makes overlap of cavity modes with the Brillouin gain spectrum unlikely. In the case of four-wave-mixing, stringent phase matching conditions are present (and will be discussed in chapter 10). For simplification, we assume that the pump wavelength and the Raman wave are on resonance and use the slowly varying envelope approximation.

$$\begin{aligned} \frac{dA_p}{dt} &= -\left(\frac{1}{2\tau_{ex}} + \frac{1}{2\tau_0}\right)_p A_p - \frac{\omega_p}{\omega_R} g_R^c \cdot |A_R|^2 A_p + \sqrt{\frac{1}{\tau_{ex}}} s \\ \frac{dA_R}{dt} &= -\left(\frac{1}{2\tau_{ex}} + \frac{1}{2\tau_0}\right)_R A_R + g_R^c \cdot |A_P|^2 A_R \end{aligned} \tag{6.4}$$

Here A signifies the slowly-varying amplitude of the pump and Raman WGM modes of the cavity and s denotes the input wave. The excitation frequency of the pump mode and resonant Raman mode is given by ω_R and $\omega_p$and τ is the total life-time of photons in the resonator, which is related to the quality factor by $Q = \omega \cdot \tau$. The coupling coefficient $\kappa = \sqrt{\frac{1}{\tau_{ex}}}$ denotes the coupling of the input pump wave s to the cavity whispering-gallery-mode E_p[46]. The Raman intra-cavity gain coeffi-

cient is denoted as g_R^c, which is related to the more commonly used gain coefficient g_R(measured in units of m/Watt) by,

$$g_R^c \equiv \frac{c^2}{C(\Gamma)2n^2}\frac{1}{V_{eff}}g_R(\omega_R,\omega_p) \text{ and } V_{eff} = \frac{\int |E_P|^2\, dV \int |E_R|^2\, dV}{\int |E_P|^2 |E_R|^2\, dV} \tag{6.5}$$

where V_{eff} is the effective modal volume, and $\overrightarrow{E}$ is electric field of the WGM. This definition of effective mode volume deviates from the previously introduced energy-density related definition, because it takes into account the spatial overlap of the pump and Raman modes, and the intensity dependent gain.

6.2.2 Effective mode volume and modal coupling

It is interesting to note that the presence of standing waves (as described by the intermode coupling parameter Γ, see chapter 3) does *not* effect V_{eff} , and for different combinations of standing-wave and traveling-wave character pump and Raman mode leads to the same value (provided pump and Raman mode are fundamental whispering-gallery modes). This is the case, since mode volume is smallest for the fundamental modes, and overlap of the fundamental with higher order azimuthal modes is low). This can be seen explicitly inserting the $\phi-$dependence pump and Raman WGM into the definition of V_{eff} (containing the proper normalization as in chapter 3), and allowing for different excitation strength of the CW and CCW amplitude (a,b). Here $m_p = \ell_p, m_R = \ell_R$ designate the azimuthal mode number of pump and Raman mode.

$$\begin{aligned}
\vec{E}_R(r,z,\phi) &= \vec{E}_R(r,z)\frac{1}{\sqrt{|a_R|^2+|b_R|^2}}\left|a_R e^{im_R\phi} \pm b_R e^{-im_R\phi}\right|^2 \\
\vec{E}_p(r,z\phi) &= \vec{E}_R(r,z)\frac{1}{\sqrt{|a_p|^2+|b_p|^2}}\left|a_p e^{im_p\phi} \pm b_p e^{-im_p\phi}\right|^2
\end{aligned}$$

As can be seen there are four possible cases of Raman and pump mode overlap, designated by $\{(++),(-+),(+-),(--)\}$. Carrying out the $\phi-$integration (and ne-

glecting the r, z integration over the transverse mode profile) yields for the $(++)$ case:

$$\begin{aligned} V_{eff}^{-1}(++) &\propto \int d\phi \cdot \frac{\left|a_R e^{im_R\phi} + b_R e^{-im_R\phi}\right|^2 \left|a_p e^{im_p\phi} + b_p e^{-im_p\phi}\right|^2}{(|a_p|^2 + |b_p|^2)(|a_R|^2 + |b_R|^2)} \\ &= 2\pi + \frac{2\pi}{(|a_p|^2 + |b_p|^2)(|a_R|^2 + |b_R|^2)} \underbrace{\int d\phi \cdot \left(2a_p b_p^* e^{im_R\phi}(|a_R|^2 + |b_R|^2) + ...\right)}_{=0}. \\ &= 2\pi \end{aligned}$$

Equivalently all the other combinations overlap factors $\{++, -+, +-, --\}$ also lead to this result, and as such the effective mode volume, is for different values of inter-mode coupling (as given by Γ) of pump and Raman mode equivalent. This result is due to the fact, that the polar mode numbers of pump and Raman mode are distinct, causing no contribution from the cross terms in the integration. Hence the effective mode volume is given for all four cases by:

$$\begin{aligned} V_{eff} &= 2\pi \frac{\int |E_p(r,z)|^2 |E_R(r,z)|^2 \, r dr dz}{\int |E_p(r,z)|^2 \, r dr dz \int |E_R(r,z)|^2 \, r dr dz} \\ &\approx 2\pi R_0 A_{eff} \end{aligned}$$

Where in the last line the highly localized nature of the WGM modes near the perimeter has been used (i.e. $r \approx R_0$).

6.2.3 Stimulated Raman scattering threshold and conversion efficiency

Steady state analysis of the coupled mode equations, results in a clamped, cavity pump field above threshold. This clamping alters the coupling of pump power to the resonator, and, in turn, the pump power dependence of Raman laser power such that the following square root dependence results.

$$P_R = \frac{\omega_r}{\omega_p} \left(\frac{1}{\tau_{ex}}\right)^2 \left(\frac{1}{2\tau_0} + \frac{1}{2\tau_{ex}}\right)^{-2} \cdot P_t \left(\sqrt{\frac{P}{P_t}} - 1\right) \tag{6.6}$$

The physical origin of this square root dependence of the pump-to-Raman conversion can be viewed as a "pumping inefficiency" i.e. the coupled pump power does not increase linearly with launched fiber power. The nonlinear dependence of coupled pump power can be illustrated by considering a pump wave that is initially *critically coupled* to the resonator. As noted above, critical coupling features complete transfer and dissipation of power from the resonator (i.e., zero transmission). In terms of the fields involved in coupling both to and from the resonator, critical coupling results from the destructive interference of the cavity leakage field with the transmitted, pump field (i.e., the portion that does not couple to the resonator from the waveguide). Once the onset of Raman lasing is reached, the cavity pump field is clamped at the threshold value resulting in a fixed cavity pump leakage field. Subsequent increase in launched pump power will imbalance the leakage and the transmitted pump fields, giving rise to finite transmission and a shift away from the critical point. The pump coupling to the resonator is thereby less and less efficient as the pump field is increased. The expression for the Raman threshold pump power can be factorized into terms involving modal volume, waveguide-cavity coupling strength and cavity lifetime (or Quality factor). To facilitate separation of the coupling and intrinsic lifetime dependence, the in chapter 4 introduced dimensionless normalized coupling parameter $K_p = \left(\frac{\tau_0}{\tau_{ex}}\right)_p$ is used. In the ideal case of a single-mode waveguide coupled to a whispering-gallery-mode the waveguide transmission as a function of coupling is given by $T = \left(\frac{1-K}{1+K}\right)^2$and K typically varies exponentially with the waveguide-microcavity "coupling gap" distance [46].

$$P_t = \frac{\pi^2 n^2}{C(\Gamma) g_R \lambda_p \lambda_R} V_{eff} \cdot \left(\frac{1}{Q_0}\right)_R \left(\frac{1}{Q_0}\right)_P \cdot \frac{(1+K_R)\,(1+K_p)^2}{K_p} \tag{6.7}$$

Here $C(\Gamma)$ is a correction factor to account for intermode coupling of the degenerate clockwise and counterclockwise propagating whispering-gallery modes, and which has been introduced and plotted in chapter 4 of this thesis. Briefly restated, the leakage of the cavity field into the backwards waveguide direction causes a reduction of the cavity buildup factor with respect to the ideal case in the absence of intermode coupling.

In the limit of strong modal coupling, the cavity buildup factor is reduced by a factor of 2, which subsequently causes a twofold increase in the threshold necessary to achieve Raman lasing. In the presence of modal coupling the waveguide coupling condition for minimum threshold experiences a slight shift towards over-coupling with the maximum shift occurring at $\Gamma \approx 1.5$. In the regime of very strong modal coupling the condition of minimum Raman threshold approaches again the original condition $K = 1/2$.

The threshold expression follows an inverse square dependence on the quality factor. This reflects the fact that an increase in Q will cause a twofold benefit in terms of both reducing cavity round trip losses that must be overcome for threshold as well as increasing the Raman gain, due to the intensity dependence of the Raman gain coefficient on the pump field ($\propto g_R I_p$). In addition, the equation shows that the threshold scales linearly with the effective modal volume. The volume dependence of the Raman threshold was examined experimentally in previous chapter, and confirmed experimentally.

The threshold equations also exhibits a strong loading dependence, and figure 6.1 shows a plot of the threshold equation for typical microcavity parameters, for the experiments in the previous chapter. A good approximation in the experiments, is to assume equal coupling strength to both pump and Raman mode i.e. $Q_{ex}^p = Q_{ex}^R$.This assumption is based on the assumption of equal evanescent field decay for pump and Raman mode, which is the case for $\ell_p, \ell_R \gg 1$ (see chapter 1). When analyzing the coupling dependence under this assumption ($Q_{ex}^p = Q_{ex}^R$) but allowing for different intrinsic Raman Q_0^R and pump Q-factors Q_0^p, the minimum threshold can be calculated and occurs for:

$$Q_{ex}^{\min} = \frac{Q_0^p}{2} + \sqrt{\left(\frac{Q_0^p}{2}\right)^2 + 2Q_0^R Q_0^p} \tag{6.8}$$

Furthermore from eqs. 6.8 it is evident that for $Q_0^R < Q_0^p$ minimum threshold occurs for $Q_{ex}^{\min} < 2 \cdot Q_0$, whereas for $Q_0^R > Q_0^p$ minimum threshold occurs for $Q_{ex}^{\min} > 2 \cdot Q_0$. When analyzing the coupling dependence under the assumption of equal Raman and pump quality factors and coupling factors $K_p = K_R \equiv K$ and $\tau_R = \tau_p$, the minimum

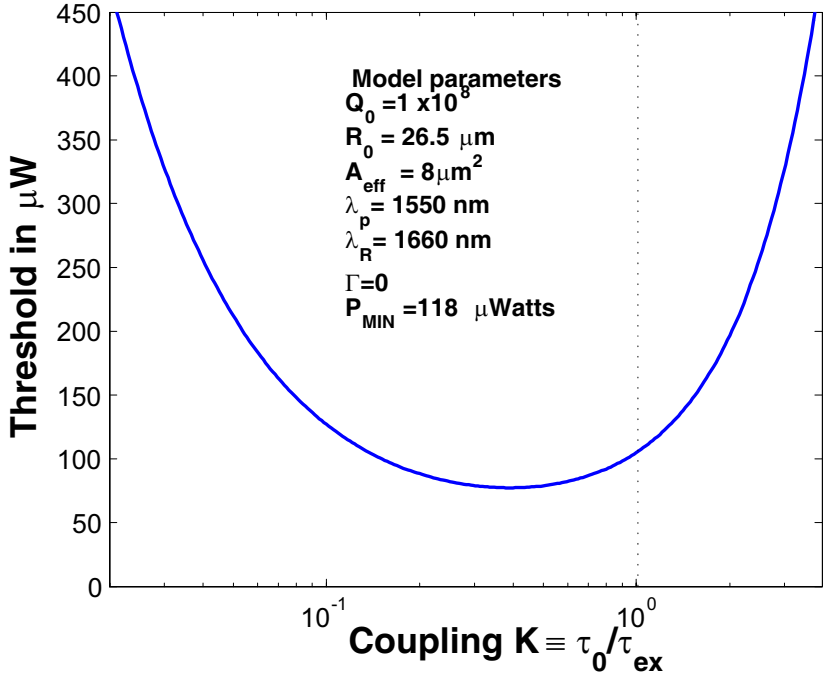

Figure 6.1: Theoretical calculation of the stimulated Raman threshold as a function of coupling, for a Q=10^8, 53-$\mu m-$diameter microsphere. Minimum threshold occurs undercoupled.

threshold occurs when $Q_{ex}^{\min} = 2 \cdot Q_0$ or $K^{\min} = \frac{1}{2}$, i.e. in the undercoupled regime with *finite* waveguide transmission of $T^{\min} = \frac{1}{9}(\tilde{}11\%)$, which was indeed observed experimentally (as noted in the last chapter).

$$P_t = \frac{\pi^2 n^2}{C(\Gamma) g_R \lambda_p \lambda_R} V_{eff} \cdot \left(\frac{1}{Q_0}\right)^2 \cdot \frac{(1+K)^3}{K} \tag{6.9}$$

$$P_t^{\min} = \frac{c\pi^2 n^2}{C(\Gamma) g_R \lambda_p \lambda_R} V_{eff} \cdot \left(\frac{1}{Q_0}\right)^2 \cdot \frac{27}{4} \tag{6.10}$$

It is worth noting that at this coupling condition, the circulating pump-power in the resonator is not maximum. This can be understood since minimum threshold represents an optimal balance of both pump coupling and Raman mode coupling loss. The conversion of pump power to Raman power above threshold can be characterized by the differential slope efficiency. The bidirectional external differential slope efficiency η_{ex} is derived by linearizing the expression for P_R near the threshold condition and is given by,

$$\eta_{ex} \equiv \frac{dP_{Raman}}{dP_{launched}} = 2 \cdot \frac{\omega_r}{\omega_p} \left(1 + \frac{1}{K}\right)^{-2} \tag{6.11}$$

Figure 3 shows the differential slope efficiency as a function of coupling strength. It is noteworthy that it approaches the value of $2\frac{\omega_r}{\omega_p}$in the limit of strong over-coupling ($\frac{\tau_0}{\tau_{ex}} = \infty$). Surprisingly, this value exceeds unity, indicating that every waveguide pump photon added above threshold, is converted on average to more than one Raman photon. This result can be understood by again considering the nonlinear dependence of coupled pump power, except this time in the over-coupled regime. In particular, the differential increase in coupled pump power grows more quickly in the over-coupled (more slowly in the undercoupled regime) than the differential increase in launched pump power. This leads to the interesting effect that the differential photon conversion efficiency can exceed unity. Taking into account the nonlinear dependence of coupled pump power by defining the internal differential efficiency η_{int} as the coupled (as distinct from the launched) pump-to-Raman power, the efficiency

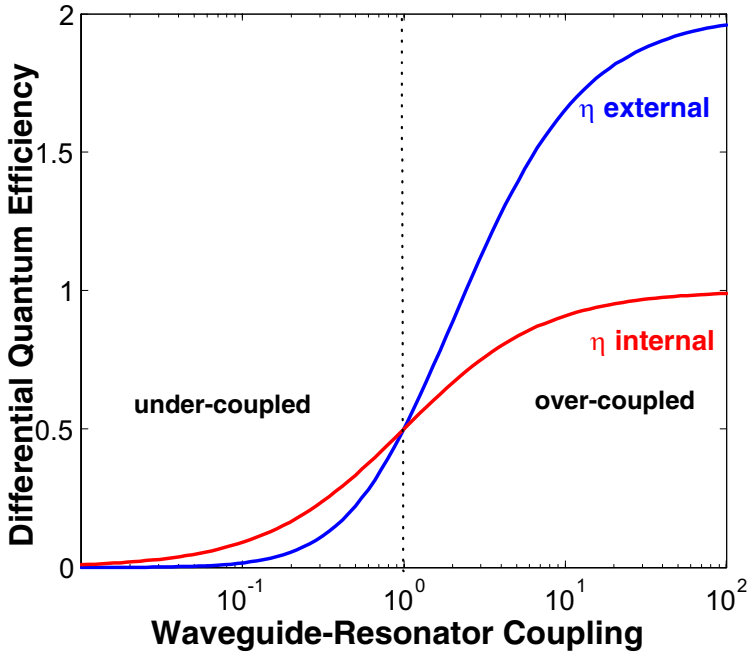

Figure 6.2: External and internal pump to Raman differential conversion efficiency. The external efficiency refers to conversion of launched pump power to Raman output power, while the internal efficiency is the coupled pump power to Raman output power. As evident, the external efficiency can exceed unity in the over-coupled regime.

approaches, as expected , the value $\frac{\omega_r}{\omega_p}$ in the limit of strong over-coupling.

$$\eta_{int} \equiv \frac{dP_{Raman}}{dP_{coupled}} = \frac{\omega_r}{\omega_p}\frac{K}{(K+1)} \tag{6.12}$$

Figure 6.2 shows both the internal and external differential Raman conversion efficiencies as a function of coupling strength.

6.2.4 Analysis of cascaded Raman scattering in high-Q microcavities

The first Raman field can itself act as a secondary pump field and generate further Raman modes. This process of cascaded Raman scattering can be described by including higher order coupling terms into the coupled mode equations of pump and Raman fields as shown below[29].

$$\begin{aligned}
\frac{dE_p}{dt} &= \left[-\left(\frac{1}{2\tau_t}\right)_P - g^c_{R1}\left(\frac{\omega_P}{\omega_R}\right)|E_{R1}|^2\right]E_p + \sqrt{\frac{1}{\tau_{ex}}}s \\
\frac{dE_{R1}}{dt} &= \left[-\left(\frac{1}{2\tau_t}\right)_{R1} + g^c_{R1}|E_p|^2 - g^c_{R2}\left(\frac{\omega_{R1}}{\omega_{R2}}\right)|E_{R1}|^2\right]E_{R1} \\
\frac{dE_{R2}}{dt} &= \left[-\left(\frac{1}{2\tau_t}\right)_{R2} + g^c_{R2}|E_{R1}|^2 - g^c_{R3}\left(\frac{\omega_{R2}}{\omega_{R3}}\right)|E_{R3}|^2\right]E_{R2} \\
&\cdots\cdots \\
\frac{dE_{RN}}{dt} &= \left[-\left(\frac{1}{2\tau_t}\right)_{RN} + g^c_{RN}\left|E_{R(N-1)}\right|^2\right]E_{RN}
\end{aligned} \tag{6.13}$$

where N is the Raman order. To find the corresponding thresholds and output powers for these higher order processes, the set of equations can be solved iteratively in steady state. To facilitate the discussion, the dimensionless coefficients c_i is introduced.

$$c_i \equiv \frac{\omega_i}{\omega_{i+1}} \cdot \frac{g^c_{i+1}}{g^c_{i+2}} = \frac{\omega_i}{\omega_{i+1}} \cdot \frac{V_{eff}(\lambda_{i+2})}{V_{eff}(\lambda_i)} \tag{6.14}$$

The general solutions for the threshold of the even and odd order N^{th} Raman modes are given by the following expressions. As in the previous section, we have assumed

equal coupling strengths and intrinsic Q factors for the pump and Raman modes.

$$\begin{aligned} P_t^{N=2m} &= \frac{1}{C(\Gamma)}\frac{1}{g_R^c}\frac{\tau_{ex}}{(\tau_t)^3}\left(\sum_{i=0}^{m}(c_i)^i\right)^2\left(\sum_{i=0}^{m-1}(c_i)^i\right) \\ P_t^{N=2m+1} &= \frac{1}{C(\Gamma)}\frac{1}{g_R^c}\frac{\tau_{ex}}{(\tau_t)^3}\left(\sum_{i=0}^{m}(c_i)^i\right)^3 \end{aligned} \tag{6.15}$$

As evident from these expressions even and odd order Stokes fields exhibit different threshold powers as a function stokes order. When considering Raman scattering in silica at optical frequencies, one can approximate the above expressions by taking $c_i \approx 1$ since the Raman shift is small compared to the optical frequency. In addition it is assumed that the mode volume is wavelength-independent. Under this assumption, the threshold expressions reduce to:

$$\begin{aligned} P_t^{N=2m+1} &= \frac{1}{C(\Gamma)}\frac{\pi^2 n^2}{g_R\lambda_p\lambda_R}V_{eff}\frac{1}{Q_0^2}\frac{(1+K)^3}{K}\cdot\frac{(N+1)^3}{8} \\ P_t^{N=2m} &= \frac{1}{C(\Gamma)}\frac{\pi^2 n^2}{g_R\lambda_p\lambda_R}V_{eff}\frac{1}{Q_0^2}\frac{(1+K)^3}{K}\cdot\frac{N^2(N+2)^2}{8} \end{aligned} \tag{6.16}$$

It follows that the threshold for cascaded Raman oscillation exhibits a *cubic* dependence on Raman order N (compare figure 6.3). The emission power varies depending upon whether the highest order wave is even or odd. For the odd order case, all odd orders increase as the square root of the pump power and even orders are clamped. For the even order case, all even order lines increase linearly with pump power while odd orders are clamped. Figure 6.3 illustrates this behavior showing the Raman output for several Stokes orders as a function of input pump power. The analytic expressions for the Raman output power in these cases are given by:

$$\begin{aligned} P^{N=2m+1} &= \eta_{ex}^N \cdot 2\left(\sqrt{P_t^N P} - P_t^N\right) \\ P^{N=2m} &= \eta_{ex}^N \cdot \left(P - P_t^N\right) \end{aligned} \tag{6.17}$$

The differential power conversion efficiencies can be obtained by linearizing the above

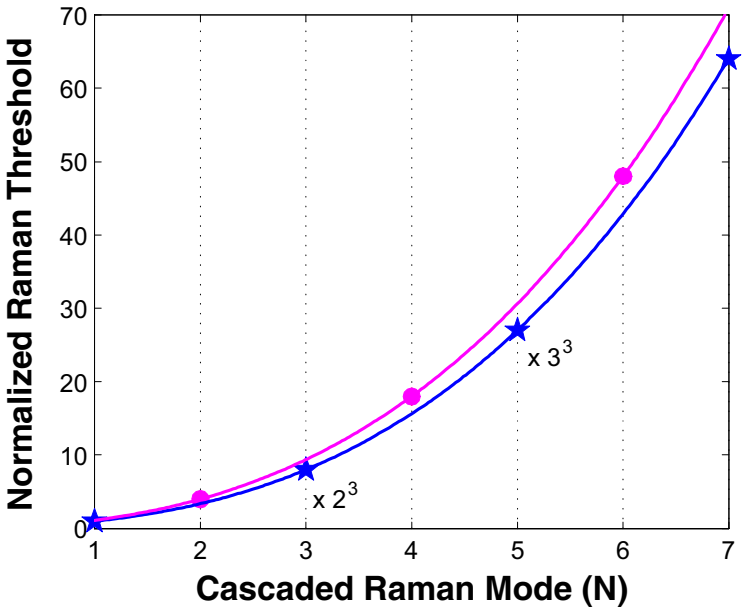

Figure 6.3: Microcavity stimulated Raman threshold as a function of cascaded Raman order (N) as given in equation 6.16. The threshold is normalized to the threshold of the first order. The cascaded Raman threshold exhibits a N^3-scaling law on Stokes order N.

expressions near the threshold condition. The external and internal differential efficiencies decrease steadily as a function of stokes order. For optical frequencies that are much larger than the Raman shift, the external differential conversion efficiency reduces to:

$$\begin{aligned} \eta_{ex}^{N=2m} &= \frac{\lambda_p}{\lambda_{RN}}\left(1+\frac{1}{K}\right)^{-2}\cdot\frac{16}{(N+2)^2} \\ \eta_{ex}^{N=2m+1} &= \frac{\lambda_p}{\lambda_{RN}}\left(1+\frac{1}{K}\right)^{-2}\cdot\frac{8}{(N+1)^2} \end{aligned} \tag{6.18}$$

For high order (N) Raman fields, the external differential conversion efficiency thus follows a $1/N^2$-dependence.

6.3 Observation of cascaded Raman scattering in ultra-high-Q microspheres

The presence of Raman scattering in microspheres leads to the possibility of generating higher order Raman modes by cascade. By using a shorter pump laser (located at around 1450 nm) cascaded Raman scattering was indeed observed. Figure 6.4 shows a typical cascaded Raman spectrum, with a second order Raman mode appearing in the 1650-nm band, two phonon frequencies shifted from the pump. The pump-to-Raman conversion characteristics for first order Raman scattering and the 2^{nd} order Raman mode are shown in the inset. It can be seen that the first order mode does indeed exhibit a square-root dependence on the launched pump power. The solid line is a fit using equation 6.17. The 2^{nd} order Raman mode, in contrast, exhibits the expected linear increase with pump power.

To study cascaded Raman scattering beyond 2^{nd} order, experiments using a 980 nm wavelength pump [29] were employed. The shorter wavelength pump allowed the observation of up-to 5th-order cascades (from 980-1300 nm) owing to the reduced mode volume at shorter wavelengths, and the higher Raman gain coefficient ($g_R \propto 1/\lambda$). With less than 900 μ-Watts of launched fiber power up to fifth order Stimulated

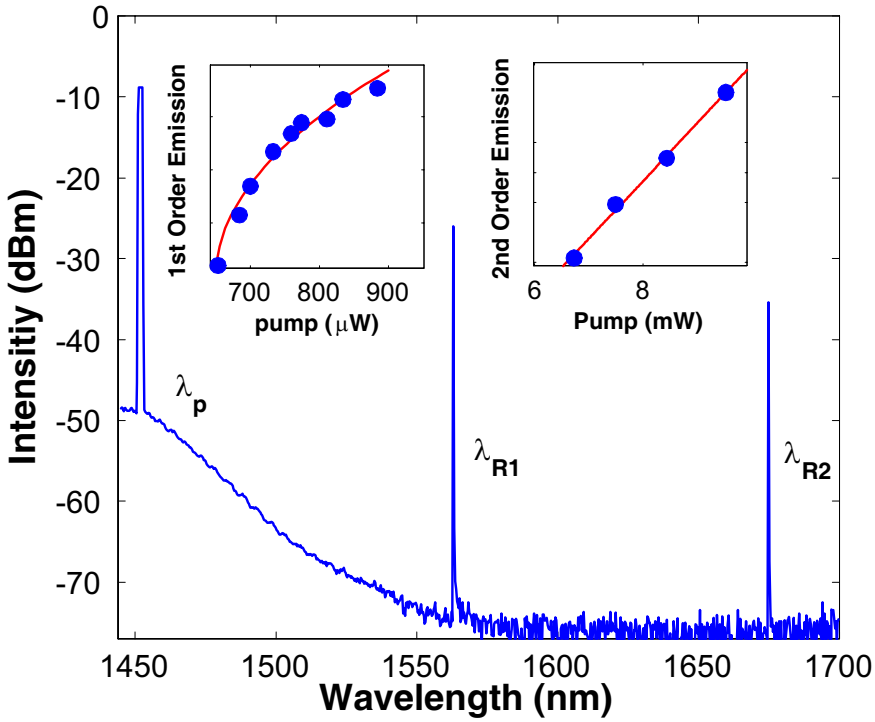

Figure 6.4: Cascaded Raman scattering in a 58-$\mu m-$diameter microcavity. The pump WGM is located at 1450 nm. The insets show the pump-to-Raman conversion for first (left inset) and second order (right inset) Raman modes (measured on different microcavities). The 1^{st} order Raman mode exhibits a square-root, and the 2^{nd} order Raman mode a linear pump-to-Raman conversion characteristic, in agreement with the theoretical prediction. Solid lines: A theoretical fit using equations 6.17.

Raman Scattering was observed [29].

6.4 Summary

In summary cascaded Raman scattering in microspheres is experimentally observed and theoretically analyzed in waveguide-coupled microcavities, which apply to the results obtained in taper-fiber coupled microspheres or toroid microcavities. A theoretical analysis was presented using the coupled mode equations for the pump and Raman WGMs. Using these equations, the threshold condition for stimulated Raman scattering was derived and the relative importance of waveguide coupling strength, mode volume and intrinsic resonator Q were described. Furthermore the analysis was extended to the case of cascaded Raman oscillation and threshold and efficiency expressions were derived for higher-order Raman fields. This analysis revealed that odd and even order Raman lines exhibit different pump-to-Raman emission characteristics. Even order Stokes fields are found to exhibit a linear increase in generated Raman power as a function of pump power, whereas odd-order Stokes fields exhibit a square root dependence. In addition the underlying scaling laws for threshold and efficiency were derived.

Chapter 7

Ultra-high-Q toroid microcavities on a chip

7.1 Introduction[1]

Wafer-scale processing techniques allow precise dimensional at the nano-scale level, and are the foundation of modern microelectronics. The potential of these techniques in the domain of optics, and in particular optical microcavities, has been extensively investigated in the early 1990, and have led to the demonstration of a variety of chip based optical microcavities concepts. Microdisk cavities were among the first chip-based microcavities demonstrated[78]. Since then, a variety of other confinement geometries, such as vertical micro-posts or photonic crystal defect cavities have been demonstrated. The small mode volume and high-Q factor of these structures, can be used in a variety of fundamental and applied studies. In addition the wafer-scale nature allow possible integration with complementary optical, mechanical or electrical functionality. Reported Q-factor results have ranged from 13,000[79] in InGaAs microdisks, to 130,000 in polymer rings[80], to a record value of more than 3 million in a silica microdisk [34] and described in thesis chapter 8.

However, these Q-factors are several orders of magnitude lower than those found in surface-tension-induced micro-cavities, since the nanometer-scale surface finish required for ultra-high-Q has not been attainable using wafer-scale processing. In this

[1] **Section 1.1-1.3 have appeared in: "Ultra-high-Q toroid microcavity on a chip", *Nature,* 421, No. 6926 (2003). Remaining sections are in preparation (2004).**

chapter, we present and explore the properties of a chip-based (planar) STIM devices in the form of a micro-toroid which combine for the first time the advantages of wafer-scale processing and ultra-high-Q [81]. These cavities are made by combining conventional micro-fabrication techniques with a laser-assisted re-flow process to achieve the atomic-scale surface finish characteristic of STIMs, and the fabrication is described in appendix A of this thesis. In this chapter, the optical properties of toroid microcavities are analyzed, and Quality factors demonstrated in excess of 100 million. This value constitutes an improvement in terms of Q-factor of nearly 4 orders of magnitude. The mode structure of these micro-cavities is shown to exhibit a strongly-reduced mode density compared to a micro-sphere of the same size. Besides Q-factor, the mode volume is of interest. Using a finite element solver, the optical modes of toroid microcavities are solved and the corresponding mode volume calculated. Numerical simulation reveals that a strong reduction of mode volume compared to spherical microcavities is possible, and experimental results for high Q-factor small mode volume cavities are presented. The highest value of Q/V was ca. $10^6 \left(\lambda/n\right)^{-3}$.

7.2 Taper coupling to toroid microcavities

The optical modes of a toroid are whispering-gallery type and circulate at the periphery of the toroidally-shaped silica cavity. Efficient coupling to the toroid microcavities can therefore be achieved using tapered optical fibers in the same experimental setup, which has been described in chapter 2 of this thesis. In particular, as the material of the cavity is silica, the effective index n_{eff} is close to the index of refraction of optical fiber, and therefore tapered fibers are also expected to achieve phase–matching of the toroidal WGM. Whereas in the case of microspheres, also D-shaped fibers or prisms have been used to efficiently excite the whispering-gallery type optical modes, the latter is not suitable for coupling to toroid microcavities on a chip, due to the proximity of the toroid to the planar silicon substrate (typically only several microns of separation). Tapered optical fibers in contrast, provide an ideal coupling technique

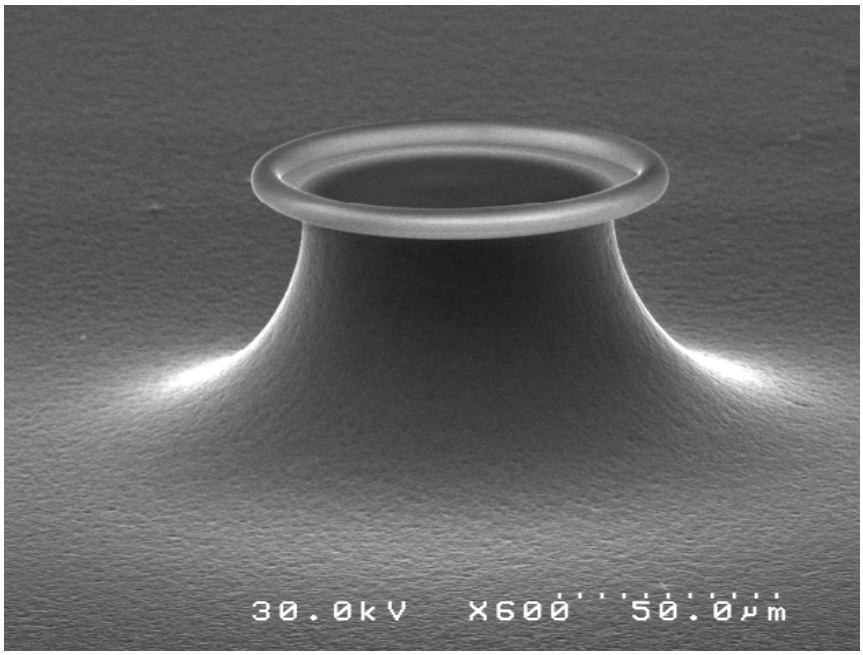

Figure 7.1: A toroid microcavity fabricated from a 1 $\mu m-$thickness thermal oxide. The toroidal cross section is apparent and exhibits a diameter of approximately 4 micron.

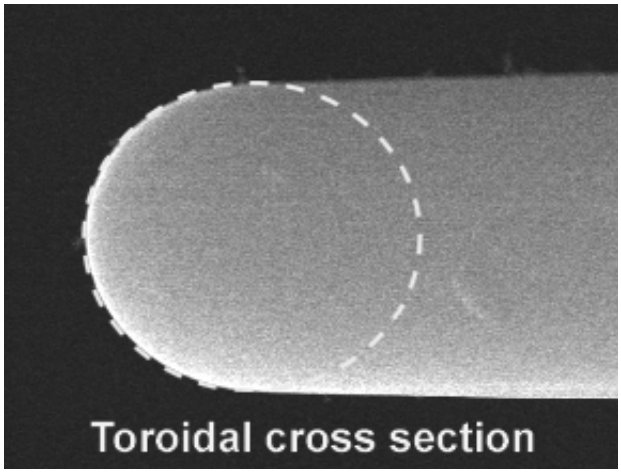

Figure 7.2: SEM image of a microdisk which underwent the CO_2 reflow process. The profile clearly reveals the toroidal shape and exhibited in this sample an eccentricity of 2%.

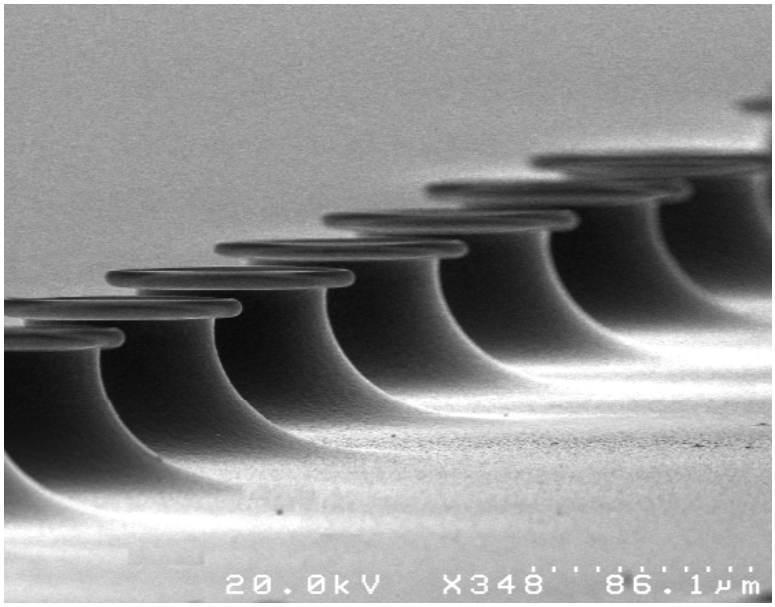

Figure 7.3: Array of toroid microcavities.

due to the small transverse extend of the tapered optical fibers, which can be used to locally excite the toroidal WGM at the cavity periphery. Figure 7.4 shows a tapered optical fiber coupled to a microtoroid in this fashion.

7.3 Cavity ringdown Q-factor measurements of toroid microcavities

Figure 7.5 shows the transmission spectra through a taper in close proximity (on the order of hundreds of nanometers) to a toroidal micro-resonator. The observed free spectral range corresponds to the angular mode number (ℓ-index, which in this case is >130). Inspection of the data (inset of Fig. 7.5) shows that the resonator supports two azimuthal (m-index or transverse) modes, tentatively identified as ($m = \ell$ and $m = \ell - 1$) and that coupling to the fundamental radial mode ($n = 1$) dominates the measurement. This is in contrast to spheres, which support $(2\ell+1)$ azimuthal modes. In the case of ultra-high-Q modes, the spectra also exhibited a reflected signal due to modal coupling, due to the sensitive nature of these modes to scattering centers, as

Figure 7.4: Optical micrograph of a tapered optical fiber coupled to a toroid microcavity on a silicon chip. The bright reflection from the central region is due to the reflection from the silicon pillar.

evident in figure 7.6. The significant reduction of azimuthal modes in this case, can be inferred from comparison with the mode spectrum of a microsphere of equivalent principal diameter, as given in figure 2.9.

The quality factor or Q of the resonators was measured in two ways, as outlined in chapter 3. First, the full-width half-maximum of the Lorentzian-shaped resonance in the under-coupled regime was directly measured by scanning a single-mode laser (short-term line-width about 300 kHz) through a resonance. Low input power levels (typically less than 5 micro-Watts) were used to avoid thermally-induced distortion of the line shape due to resonant-field buildup within the cavity. Repeated measurements on samples fabricated with various radii (80-120 μm) and tori thickness (5-10 μm) yielded Q values in excess of 100 million (10^8). This is a record value for a planar device, and constitutes an improvement by nearly 4 orders of magnitude over all previous planar micro-resonators fabricated by wafer-scale processing[2].

[2]It is interesting to note that the optical modes of disk microcavities made from silica deposited by electron-cyclotron-resonance plasma-enhanced chemical vapor deposition (ECR-PECVD), exhibited Q-factors typically 1-2 orders of magnitude below those of thermally grown oxide. The laser assisted reflow did improve the quality factor, but to a level typically 1-2 orders of magnitude lower than for thermal oxide.

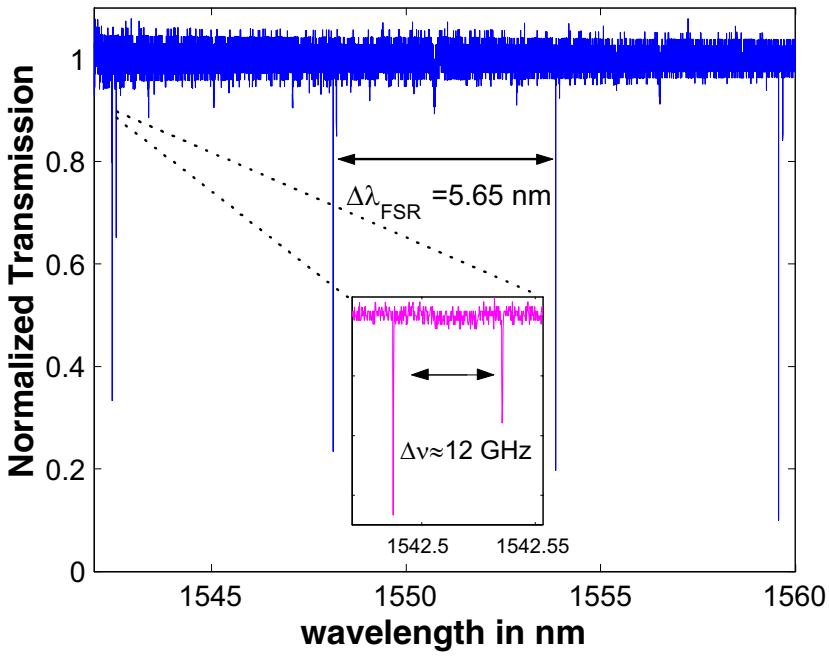

Figure 7.5: Typical transmission spectrum of a toroidal resonator. The free spectral range (defined as the wavelength spacing between modes with successive angular mode number ℓ) is 5.65 nm, which corresponds to a 94-μm-diameter torus. The inset shows the splitting of the different azimuthal modes, which is ~12 GHz (0.1 nm).

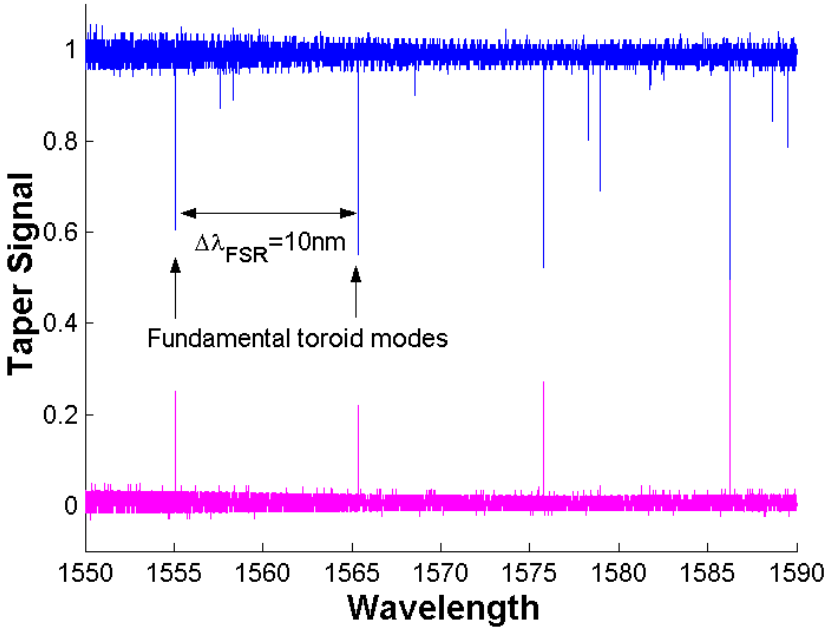

Figure 7.6: Transmission and reflection spectrum of an ultra-high-Q toroid microcavity on a chip. The designated fundamental toroid modes are separated by the free spectral range ($\Delta\lambda = 10\ nm$). Due to the presence of modal coupling the optical modes appear as doublets, giving rise to reflection (magenta). The fundamental modes couple most strongly to the taper mode and higher order modes are more weakly coupled.

As an independent and more precise measurement of quality factor, the photon lifetime was directly measured by cavity ringdown (The experimental setup has been described in Chapter 2). In particular, ringdown measurements are immune to the thermal effects described above. This was done by repeatedly scanning the laser into resonance with a mode that was critically coupled (i.e. $T = 0$) to the taper. As the laser scanned into resonance, power transfer increased until maximal "charging" of the resonant mode was attained. At this moment, the laser input was gated "off" by use of a high-speed, external modulator and cavity ringdown is observed as the resonant power discharges. Because the resonator is by necessity loaded during this measurement, the observed ringdown time yields the loaded Q-factor at the critical point (not the intrinsic Q). Data from a typical ringdown measurement is shown in Fig. 7.7. At time $t = 0$ in the figure, the laser is fully gated off and the detected power is due entirely to the cavity discharge field. The solid line represents an exponential fit as expected for decay of a single cavity mode. The inset shows a logarithmic plot to infer the cavity lifetime. Nearly two orders of magnitude decay could be observed before reaching the instrumental noise level. The loaded lifetime in this structure was 43 ns. As a further check on this time constant, after fully gating-off the pump laser the waveguide power has dropped to 80% of its predicted maximal value. This value is in agreement with the gating delay of the ringdown setup (approximately 8 ns). In particular, using the observed mode-lifetime of $\tau = 43\ ns$ yields,

$$T_0 = e^{\Delta t/\tau_{crit}} \approx 0.83$$

As noted before, to infer the intrinsic cavity Q it is necessary to correct for loading by the taper waveguide. In addition it is necessary to take into account excitation of the counter-propagating mode due to scattering centers intrinsic to the resonator (described by a dimensionless inter-mode coupling parameter Γ [82] as has been introduced in chapter 4). For the mode of figure 7.7 the inter-mode coupling was measured to be approximately $\Gamma \approx 1$, giving rise to a weak counter-propagating wave excitation (17% of the cavity buildup field is stored in the counter-propagating mode at critical

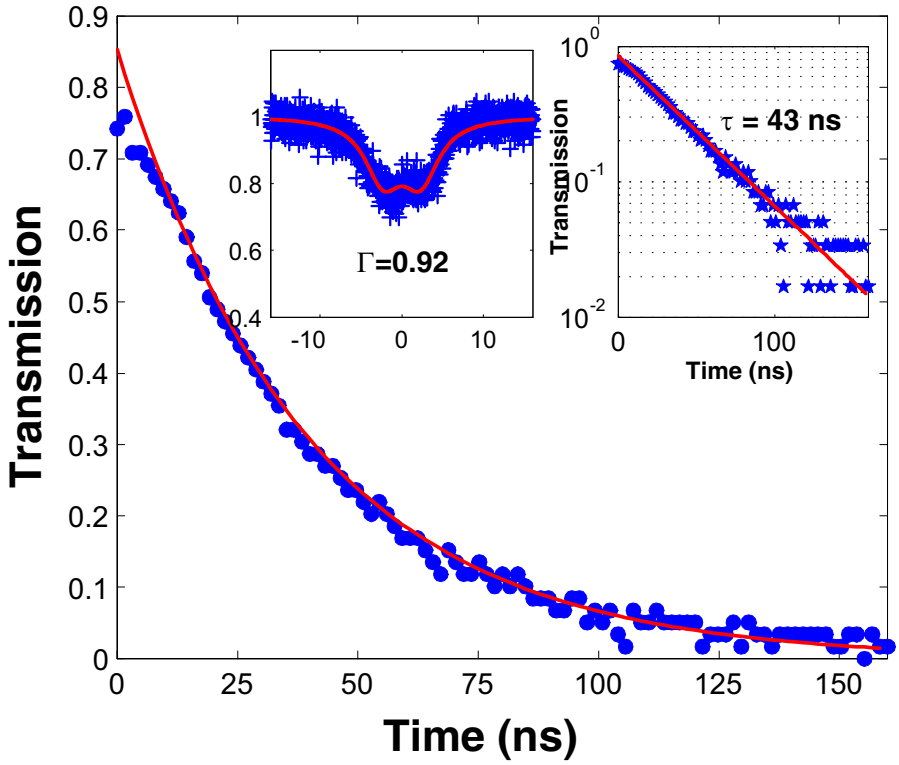

Figure 7.7: Cavity ringdown measurement of a toroid microcavity at the critical coupling point. The solid line is a fit using an exponential decay of the recorded cavity leakage field. Right Inset: logarithmic plot to infer the cavity decay time. Left inset: Under-coupled line-width scan to obtain the splitting frequency and modal coupling parameter. When taking into account the waveguide loading and modal coupling, the measured lifetime of $\tau_{crit} = 43\ ns$ and corresponds to an intrinsic quality factor of $Q = 1.25 \times 10^8$.

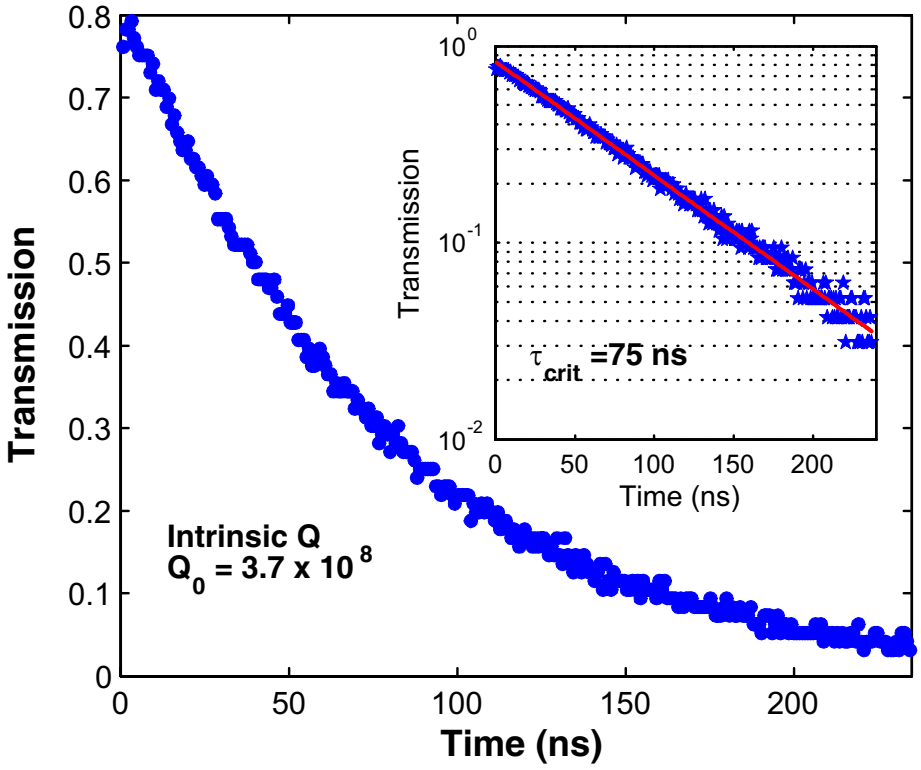

Figure 7.8: Cavity ringdown measurement of a toroid microcavity with a free spectral range $\Delta\lambda_{FSR} = 7.3\ nm$. The main figure shows the cavity decay signal at the critical coupling point, exhibiting a critical decay time of 75 ns (which corresponds to 0.98×10^8). When correcting for waveguide loading ($\Gamma \approx 3$) the intrinsic Q-factor yields 3.7×10^8. The corresponding finesse of the cavity is $F = \Delta\lambda_{FSR}/\Delta\lambda = 1.74 \times 10^6$.

coupling). As has been discussed in chapter 4, the presence of inter-mode modifies the relation between intrinsic (unloaded) and critically coupled Q:

$$Q \equiv \omega_0\tau_0 = \omega_0\tau_{crit}\left(1+\sqrt{1+\Gamma^2}\right) \tag{7.1}$$

This yields an intrinsic cavity Q of 1.25×10^8 inferred from cavity ringdown. This value agrees with the measurements of the frequency line shape described above. The highest optical Q-factor presently observed in toroid microcavities is shown in figure 7.8, yielding a intrinsic Q factor of 4×10^8, which has been observed in a microtoroid with a ca. 70 μm principal diameter.

Finally, there is an alternate method for determining the intrinsic Q factor in cases where thermal broadening does not allow to accurately determine the intermode coupling parameter. This approach does not require knowledge of Γ, but rather only the doublet splitting frequency (γ^{-1}). As before, the ring-down lifetime at the critical coupling condition is measured. However, now the following expression is used to relate both this information and the measured splitting frequency to the intrinsic Q factor.

$$Q_0 = \omega\tau_0 = \frac{2}{\tau_{crit}}\left(\frac{1}{\tau_{crit}^2} - \frac{1}{\gamma^2}\right)^{-1} \tag{7.2}$$

This method is less sensitive to thermal effects since the splitting frequency is nearly immune to thermal shifts (since for symmetric mode splitting, each mode is affected equally by the excitation wave and thermally shifted by equal amounts).

7.4 Modeling of toroidal whispering-gallery modes

Besides the Q-factor, an understanding of the optical modes of toroid microcavities is of significant interest. In this section the intensity distribution and mode volume of toroid microcavities are calculated, within the scalar wave equation approximation. The details of the modeling are given in appendix C. Figure 7.9 shows the mode volume for a fundamental toroid mode (TM-polarization) as a function of minor diameter (d). In this simulation the angular mode number ($\ell = 138$) was kept constant, as well as the toroid principal diameter ($D = 50\mu m$). The case of equal minor and principal diameter ($d = D$) corresponds to a microsphere. As evident from the calculation, and intuitively expected, the mode volume decreases as a function of the toroid minor diameter. Two regimes of mode volume reduction can be identified.

7.4.1 Weak modal compression regime

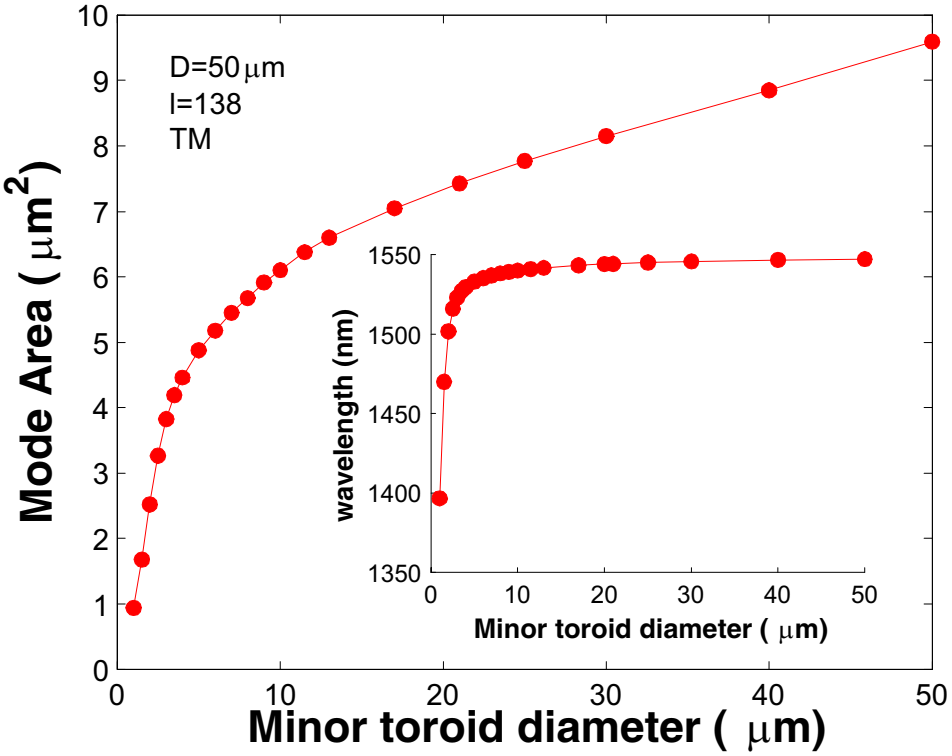

Figure 7.9: Numerically calculated mode volume of the fundamental (TM-polarization) toroid mode as a function of minor toroid diameter (d). In this calculation the principal toroid diameter (D) was kept constant at a value of 50 μm. The angular mode number was $\ell = 138$ and was kept constant in this simulation.The inset shows the resonance wavelength as a function of minor toroid diameter (d).

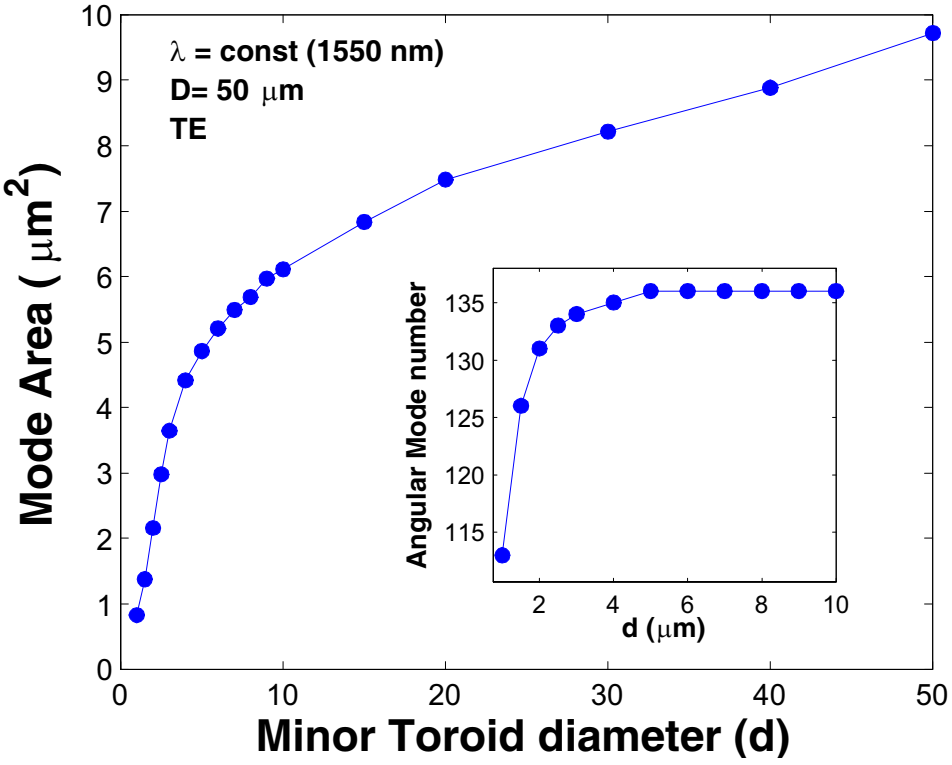

Figure 7.10: The mode area of a fundamental toroid mode with principal diameter of 50 μm as a function of minor toroid diameter (d). In the numerical modeling the angular mode number was adjusted to correct for the wavelength shift, due to the decreased effective index. Inset: Angular mode number as a function of toroid diameter.

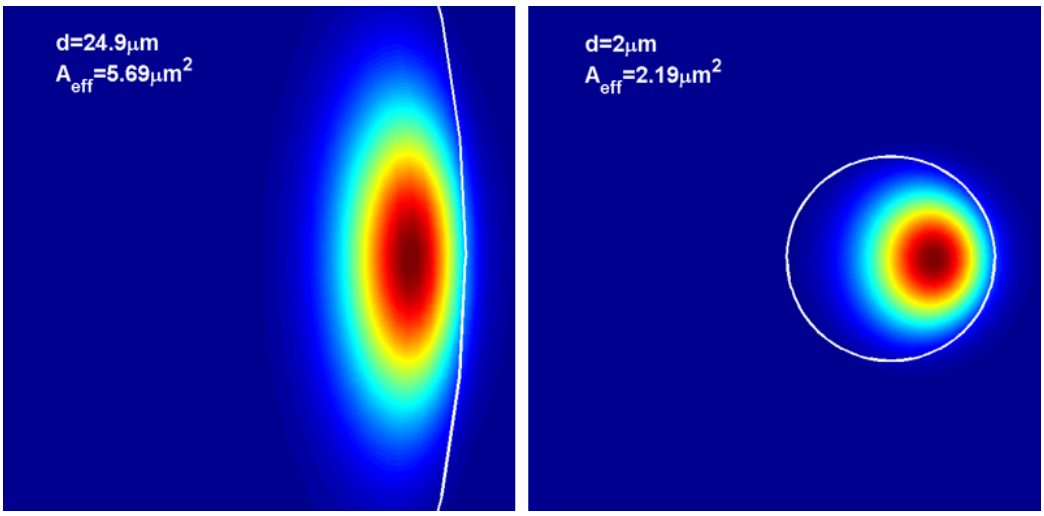

Figure 7.11: Intensity plot $|E_\phi|^2$ for a fundamental TM-mode with an angular mode number $\ell = 66$ for a silica microsphere (left panel) and for a silica toroid (right panel). The principal diameter is constant ($25\mu m$).

In the initial transition from a spherical ($d = D$) to a toroidal ($d < D$) geometry, the mode volume is reduced slowly (obeying a $V_m \propto d^{1/4}$ scaling law). The resonance wavelength of the mode (shown in the inset of figure 7.9) is perturbed slightly and shifted to shorter wavelengths. The wavelength shift exhibits a much slower dependence on the toroidal cross section than the mode volume (obeying a $\lambda \propto d^x$,with $x = 0.04$). Since in this "weakly perturbative" regime the resonance frequency remains nearly unchanged and the mode volume is slowly decreasing, it can be inferred that the dominant effect of the toroidal geometry are changes of the azimuthal eigenfunctions (spherical harmonics in case of a sphere).

Indeed, numerical modeling confirms (figure 7.12) that the radial field dependence (which in a sphere determines the resonance locations), remains only weakly perturbed in this regime, whereas the azimuthal eigenfunctions are perturbed significantly leading to narrowed field distribution in the azimuthal direction.

7.4.2 Strong mode volume compression

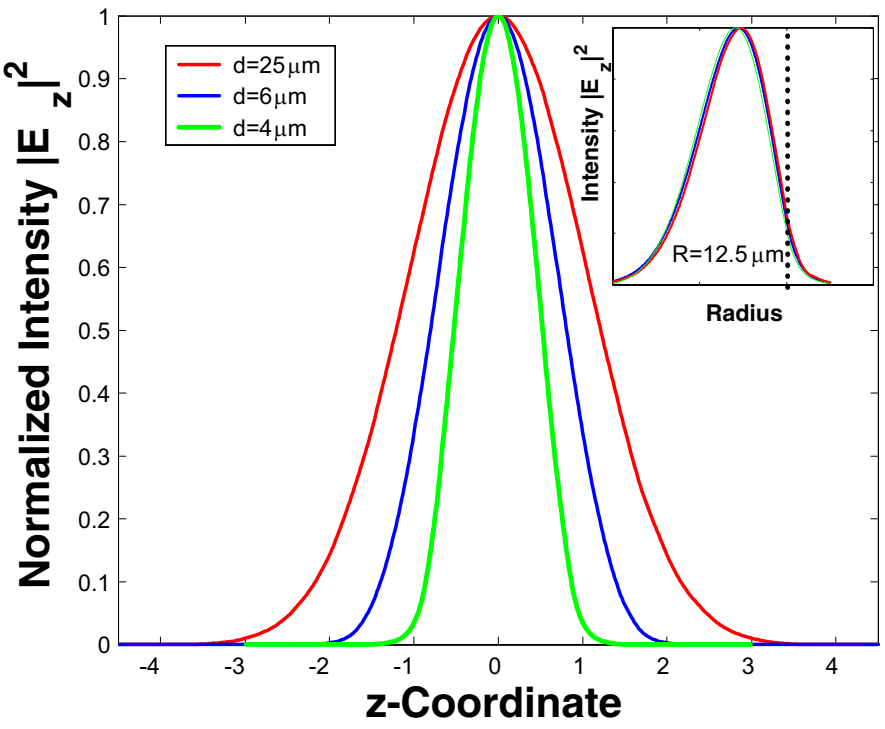

Figure 7.12: Radial (inset) and polar (main figure) intensity distribution for a microsphere ($D = d = 25\mu m$) and toroid microcavities ($d = 6\mu m, d = 4\mu m$). The polar scan is taken at a radial position corresponding to the maximum intensity.

Upon reducing the toroid cross section beyond the weak model compression regime, a transition to a rapidly decaying mode area can be observed in the simulation. In this strong compression regime, not only the azimuthal eigenfunctions are significantly changed, but also the radial eigenfunctions. The latter is evident from the fact that the resonance locations are strongly shifted to higher frequencies, as seen in the inset of figure 7.9. This is expected as the strongly reduced azimuthal degree of freedom of the toroid leads to an increase in field intensity outside the dielectric cavity, leading to a lower effective index n_{eff} (and as a result a shorter effective round-trip path-length). This also implies that in order to calculate the mode volume for constant resonance frequency (which reflects the experimental situation where the excitation wavelength is kept constant), the angular mode number has to be adjusted to lower values in order to compensate the decreased effective index $n_{eff} = \beta_m/k_0$. Taking this into account the mode volume is seen to decrease earlier than in the simulation for constant ℓ, making the mode volume compression even more severe in this regime.

Figure 7.10 shows the result of the adjustment of the angular mode number for a 50 μm-diameter toroid microcavity as a function of minor toroid diameter (TE-polarization). The inset of figure 7.10 shows the changes in the angular mode number, which shifts from its original value ($\ell = 138$ for $d = D$) to a value of $\ell = 113$ for $d = 1$ μm. It is significant to note that due to the reduction in angular mode number, also the whispering-gallery loss is expected to increase (as discussed for a microsphere in chapter 2).

7.5 Fabrication of small mode volume toroid microcavities

In many microcavity applications the figure of merit is determined by a combination of Q-factor and mode volume. Table 7.1, shows a list of representative areas and their respective microcavity requirements. The preceding section has shown, that the mode volume of toroid microcavities is reduced with respect to the mode volume of

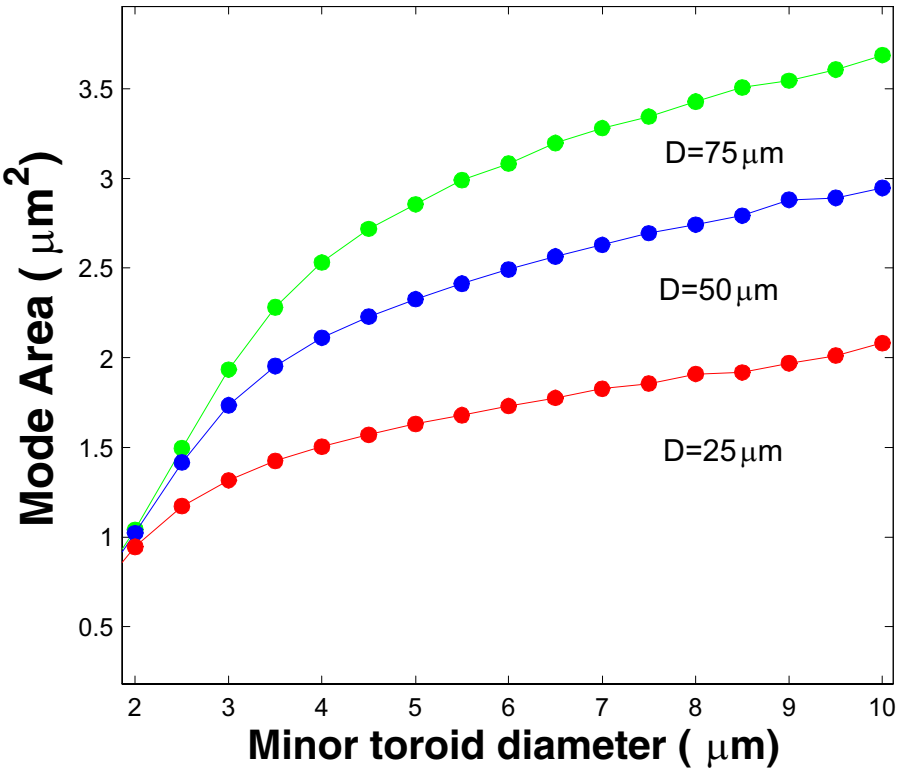

Figure 7.13: Mode volume of toroid microcavities as a function of minor toroid diameter (d), for various principal toroid diameter $(25, 50, 75\mu m)$.

Area of Study	**Figure of Merit**	**Q-V Dependence**
Weak coupling	Purcell-factor	$F_p \propto \left(\frac{Q}{V}\right)$
Strong coupling	Crit. atom/photon number	$N_0 \propto \frac{V}{Q}, n_0 \propto \frac{1}{V}$
Photonics	Laser threshold, optical loss	$P_{thresh} \propto \frac{1}{Q}$
Bio-chemical sensing	Finesse (sensitivity)	$F \propto \frac{Q}{V}$
Nonlinear optics	Threshold Nonlin. oscillation	$P_{NL} \propto \frac{V}{Q^2}$

Table 7.1: Microcavity application areas and their respective figure of merit, expressed in mode volume (V), and Quality factor (Q).

a spherical microcavity of identical principal diameter.

In this section the experimentally possible reduction of mode volume is investigated experimentally for toroid microcavities with varying principal diameter (d). Toroid microcavities used for this study were fabricated from 1 micron thermal oxide wafers, and exhibited a toroidal cross section of less than $d < 4\ \mu m$. As in the case of microspheres, small principal diameter toroid microcavities ($D < 40\ \mu m$) were observed to exhibit strong modal coupling ($\Gamma > 10$). Figure 7.14 shows the Q-factor (measured at 1550 nm) as a function of principal toroid diameter, for approximately constant minor toroid diameter (d). Ultra–high Q in excess of 10^8 could be maintained for principal diameters of more than 28 μm. Subsequent decrease of principal diameter resulted in a strong reduction of Q. The solid line is the whispering-gallery-loss limit for a microsphere calculated by numerically solving the characteristic equation (for TE and TM polarization), as has been discussed in chapter 2. The toroid microcavities exhibited a Q-factor nearly an order of magnitude below the spherical radiation limit, indicating that other Q-limiting processes, such as surface scattering, significantly determine the experimentally observed Q-factor. The inset of figure shows the ratio of Q-factor to mode-volume, by measuring the geometry parameters using a SEM. The highest Q/V achieved in the present study was $8.9 \times 10^5(\lambda/n)^{-3}$ which is nearly an order of magnitude larger than recent measurements in photonic crystals defect cavities. It is worth noting that the finesse of this structure F of nearly

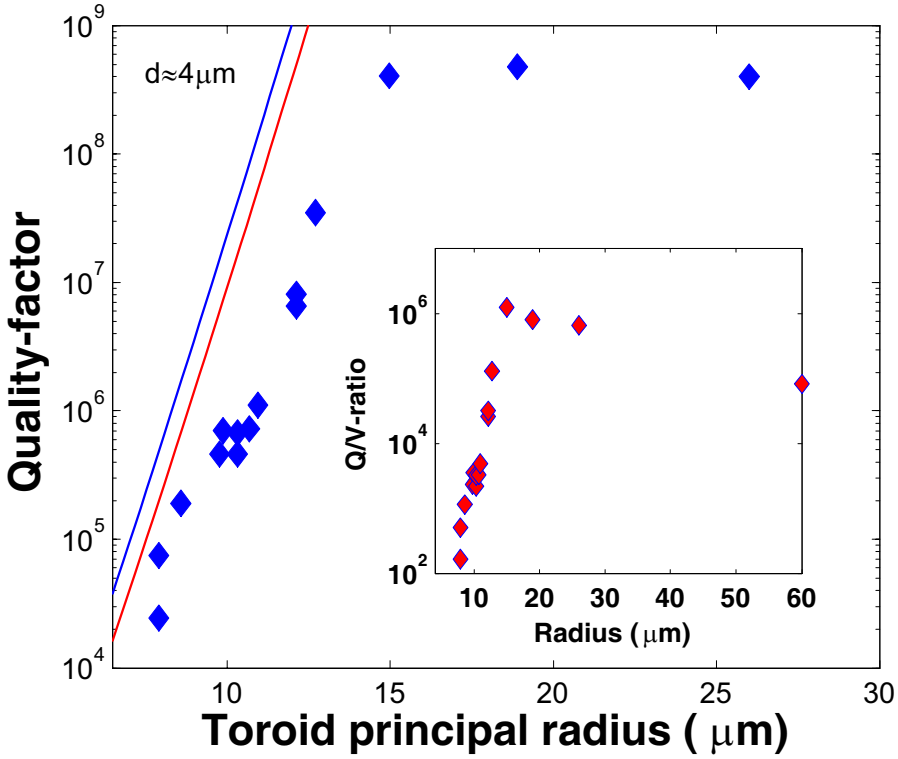

Figure 7.14: Main figure: The optical Q-factor measured as a function of toroid principal diameter (D) for approximately constant toroidal cross-sectional diameter ($d \approx 4\mu m$). The numerically calculated whispering-gallery-loss Q-factor is given by the solid line (blue:TE-case, red: TM-case). Inset: The ratio of quality factor to mode volume (in μm^3) for the devices tested.

4.6×10^6 constitutes a record value for an optical microcavity.

7.6 Summary

Thus ultra-high-Q planar cavities on a chip were demonstrated for the first time. Toroid-shaped microcavities were formed using a combination of lithography, dry etching and a selective re-flow process, as described in the appendix A. Self-limited collapse of a molten silica disk enables the dimensional control typical of wafer-scale processing while providing the surface finish (and hence cavity Q) typical of a spherical resonator. Q values obtained by this process are typically four orders of magni-

Parameter:	**Value:**
Quality factor ($Q = \omega\tau$)	400×10^6
Mode volume (V)	d=3.5μm D=14.4μm
Ratio Q/V	890,000 $(\lambda/n)^{-3}$
Finesse F	4.7×10^6
Purcell-factor F_p	6.8×10^4

Table 7.2: Characteristic parameters of an ultra-high-Q small mode volume toroid microcavity.

tude higher than previous wafer-based resonators. In some applications mode volume is also an important factor, and certain chip-based micro-resonators[83] [84] feature smaller mode volumes than the present structures. As a gauge to the lower bound on size, radiation leakage becomes a significant factor in determining Q for diameters less than 28 micron. The highest Q-factor to mode-volume ration obtained was 890,000 $(\lambda/n)^{-3}$. The planar nature of the toroid microcavity and the large transparency window of silica suggest that these devices will find a wide range of applications in photonics as well as in fundamental studies. As an indication of the possibilities for these structures, in the course of this work nonlinear optical effects have been observed with characteristics comparable to recent studies on spherical ultra-high-Q cavities, and which will be investigated in the next chapters. As standard processing techniques are used, the addition of optical functionality by techniques such as implantation or coating is possible. Likewise, electrical functionality can be introduced to integrate control functions with the ultra-high-Q microcavities. More generally, this work provides a new functional element that is synergistic with recent demonstrations of basic experimental physics on a chip. For example, by combining the present results with techniques recently demonstrated to integrate atomic traps on a chip[85] it would be possible to achieve chip-scale integration of cavity quantum electrodynamics experiments and related devices. Finally, there is great interest in improving the sensitivity of biological and chemical sensors. Proposals based upon optical resonators[86] will benefit from the ability to attain ultra-high Q on a chip.

Chapter 8

Optical properties of microdisk resonators

8.1 Introduction[1]

Using a combination of lithography and etching, semiconductor whispering-gallery microcavities have obtained Q values in the range of 10^4 [84] while polymer whispering-gallery cavities have recently obtained a Q value of 10^5. Q values are typically limited by scattering at the all-important resonator perimeter. As a way to overcome this problem, we have recently reported a technique to fabricate ultra-high-Q (exceeding 10^8) toroid microcavities on a chip [30]. In that work a laser-assisted re-flow step is used to achieve the atomically-smooth resonator surface finish characteristic of ultra-high-Q surface-tension-induced-microcavities. In this chapter it is demonstrated that - surprisingly - planar silica disk resonators can exhibit whispering-gallery-type modes with high-Q values in excess of 1 million and up to 5×10^7, without any additional chemical or laser processing. The observed Q-factors are due to modal isolation, due to the wedge shaped perimeter of the microdisk cavities. The proposed mechanism is in agreement with experiments and numerical modeling of the microdisk modes. The spectral properties of these resonators are very regular and reproducible, and are readily modeled. Additionally, highly efficient coupling to a planar resonator is demonstrated by efficient coupling to these resonators through a tapered optical fiber.

[1] **This chapter has been published in "Fabrication and coupling of high-Q silica disk microcavities", Applied Physics Letters, 83(4), p.797-799 (2003).**

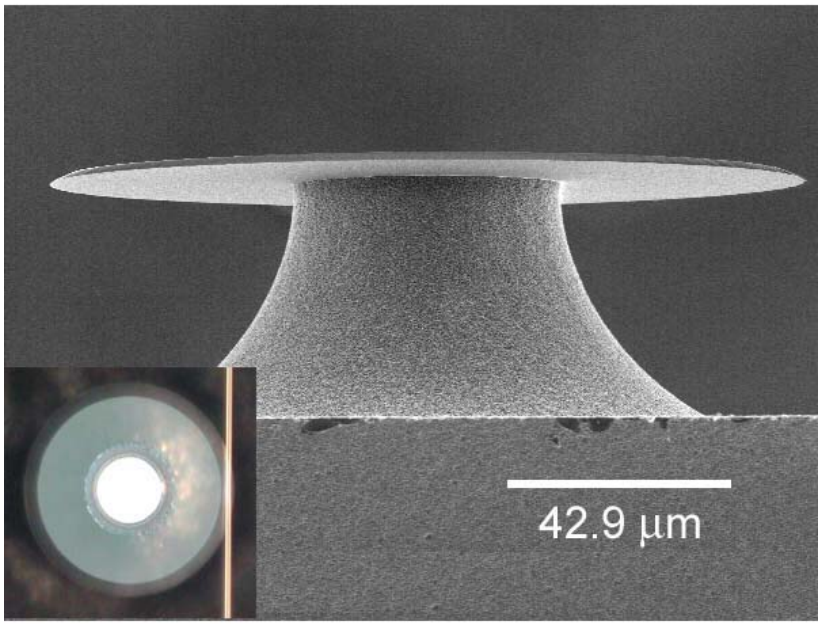

Figure 8.1: Scanning electron micrograph of a silica disk resonator. Inset: A silica micro-disk coupled to a tapered optical fiber.

8.2 Taper coupling to microdisk resonators

To analyze the quality factor of these modes as well as the mode spectrum, tapered optical fibers [55] were used to couple to the disk resonator. The tapered fiber was attached to a piezoelectric stage which allows precise positioning of the taper with respect to a silicon wafer containing multiple microdisks. An optical micrograph of a taper coupled to a disk is shown in the inset of figure 8.1.

When brought in the proximity of the microdisk, the taper mode can evanescently excite a whispering-gallery mode. The efficiency of this process depends on the ratio of parasitic loss (e.g. undesired coupling from either the fundamental taper mode or the target resonator mode to higher order taper modes or radiation modes) to the intended taper-junction coupling. The efficiency of this junction in the context of

coupling to high-Q micro-resonators has been studied in reference [55]. Figure 8.2 shows the absolute transmission and reflection properties at resonance as a function of the taper-disk gap of a microdisk resonator side-coupled via a tapered fiber. As the taper is progressively moved closer to the resonator (step-size being 20 nm), the transmission transits different coupling regimes, from undercoupled to critically-coupled to over-coupled [46]. Nearly complete extinction is reached at the critical point ($> 99\%$). When further reducing the gap distance the over-coupled transmission approaches unity (the actual measured value is $> 93\%$). In addition, bringing the taper close to the microdisk caused negligible scattering as observed by the small increase in off-resonant loss of $< 5\%$. The fact that strong over-coupling can be achieved, with negligible off-resonant loss, demonstrates the high efficiency of the tapered-fiber-coupling junction, which is $> 93\%$ in this case [55].

The quality factor of whispering-gallery resonances was inferred by line-width measurements, using a 300 kHz external-cavity diode laser to excite the resonances in the 1550-nm band. Q-factors above 1 million were consistently observed, the highest observed value to date being 3.2×10^6. We attribute the high quality factor, despite the lithographic roughness (which can be observed at the cavity perimeter with an optical microscope), to the fact that the cavity disk perimeter exhibits angled side-walls, due to the use of an isotropic etch. The wedge is believed to induce *modal isolation* from the disk edge, where etch blemishes are most pronounced. The fact, the highest optical Q-factor observed in devices exhibiting the strongest wedge angle (ca. 8 degree) also supports this hypotheses.

Due to a combination of perimeter roughness and intrinsic thermal-oxide inhomogeneities, a fraction of the circulating power is back-scattered into the mode that counter-propagates with respect to the mode excited by the taper. As discussed in chapter 4 this mode couples out of the resonator in the reverse direction along the fiber, equivalent to a reflection [82]. The transmission (T) and reflection (R) through the resonator-waveguide system in the presence of backscattering are given by (at

line-center $\Delta\omega = 0$):

$$T = \left[\frac{\Gamma + (1-K)(1+K)}{\Gamma + (1+K)^2}\right]^2 R = \left[\frac{2\Gamma K}{\Gamma + (1+K)^2}\right]^2 \tag{8.1}$$

Here Γ accounts for the excitation of the counter-propagating waveguide mode, and K is the coupling strength, defined as $K \equiv \frac{\tau_0}{\tau_{ex}}$ (i.e. the ratio of intrinsic lifetime to the coupling lifetime). The $K-$parameter typically varies exponentially with waveguide-resonator separation. The Γ-parameter was readily be measured in the undercoupled regime by observing the associated resonant splitting [82] and was approximately 1.5 for the device measured in figure 8.2. The observed reflection of approximately 28% is consistent with this Γ value using theory. We have observed the regime of strong modal coupling with inter-mode coupling parameters up to $\Gamma \approx 10$ for structures of similar dimensions. The solid lines in Figure 8.2 represent a theoretical fit using equation 8.1.

8.3 Microdisk mode Structure

We also investigated the mode-structure of the samples. Figure 8.4 shows the measured cavity mode spectrum for a 114-μm-diameter resonator (2-μm-oxide thickness). The dimensions were measured by scanning-electron-microscope studies. The spectrum was taken for both polarizations (TE/TM) supported by the microdisk resonator. The free spectral range (modes with successive angular mode numbers) was measured to be $\Delta\lambda_{FSR} = 4.80\ nm$. We inferred the approximate center of the radial field distribution from the free spectral range $\Delta\lambda_{FSR} \approx \frac{\lambda^2}{2\pi \cdot R \cdot n}$ using the refractive index of thermally-grown oxide $n = 1.445$ (the actual effective index is expected to be lower than the bulk value). The resulting diameter of 109 μm lies between the measured inner wedge edge (100 μm) and outer (114 μm) diameter of the disk, suggesting that the modes are confined to within inner and outer radii of the wedge. A further indication is that the maximum coupling strength of these modes was achieved with the tapered fiber located tangentially near the center between inner and outer radii.

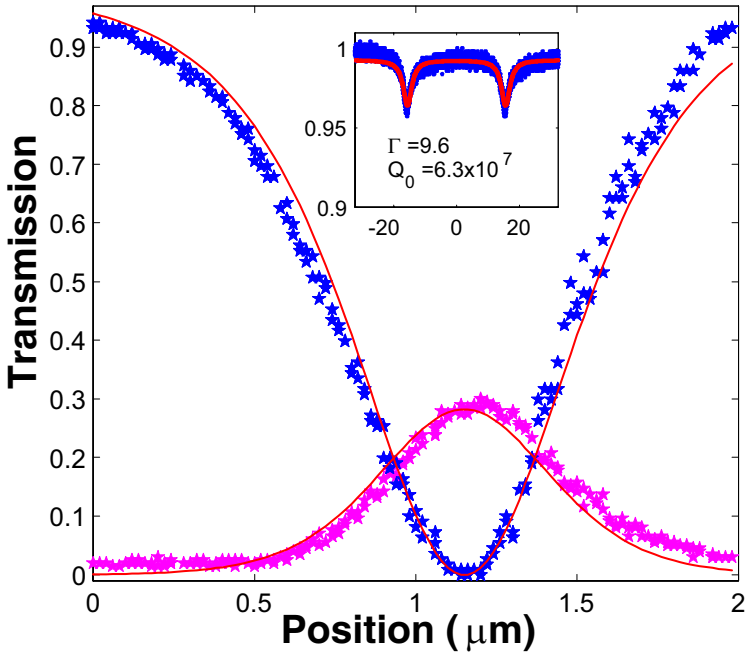

Figure 8.2: Transmission (normalized with respect to the launched fiber power, with the tapered fiber far away from the resonator) and reflection properties versus taper-disk gap-distance. The inset shows the transmission versus frequency near the critical point. The off-resonant loss was less than 5%. Inset: Undercoupled line-width scan of the device with the highest Q-factor of 6×10^6 exhibiting strong modal coupling ($\Gamma = 9.6$).

These findings are consistent with the conjecture concerning the origin of the high modal Q.

To confirm the hypothesis of modal isolation, the optical modes were numerically modeled using a finite element solver PDE solver. Figure 8.3 shows the calculated intensity distribution of a fundamental mode of a disk microcavity for three different wedge angles. In this simulation, the resonant wavelength was $\lambda = 1550\ nm$, and a principal diameter of 50 μm was used. The simulation reveals the increased modal isolation from the scattering-contributing edge perimeter, as the wedge angle (or the corresponding wedge parameter w,which is related to the inner diameter $D - w$) is decreased. In addition, modeling the geometry which was measured above yielded a mode center located at 105.2 μm . This value is smaller than the approximate value of calculated above (109 μm), due to the expected reduced effective index (i.e. $n_{eff} < n$).

As the WGM's of this structure cannot be solved analytically, approximate solutions were obtained using a simplified disk model. Identifications using this model are given in figure 8.4 with first and second order radial modes denoted using circles and diamonds. The TE/TM spectra exhibit slightly different splitting of the radial modes (0.6 and 0.8 nm). In addition, the influence of vertical confinement on mode spectra was studied. In experiments two samples having layer thicknesses of 1 and 2 microns were measured. The resulting spectra exhibit qualitatively the same structure as shown in figure 8.4. However, as the oxide thickness was reduced from 2 to 1 micron, the splitting of the two dominant radial modes increases significantly for one polarization, while remaining practically unchanged for the other.

8.4 Application of disk microcavities for add-drop devices

The high-Q devices demonstrated here can be important for low insertion loss devices such as add-drop filters, which typically require large bandwidth and correspondingly

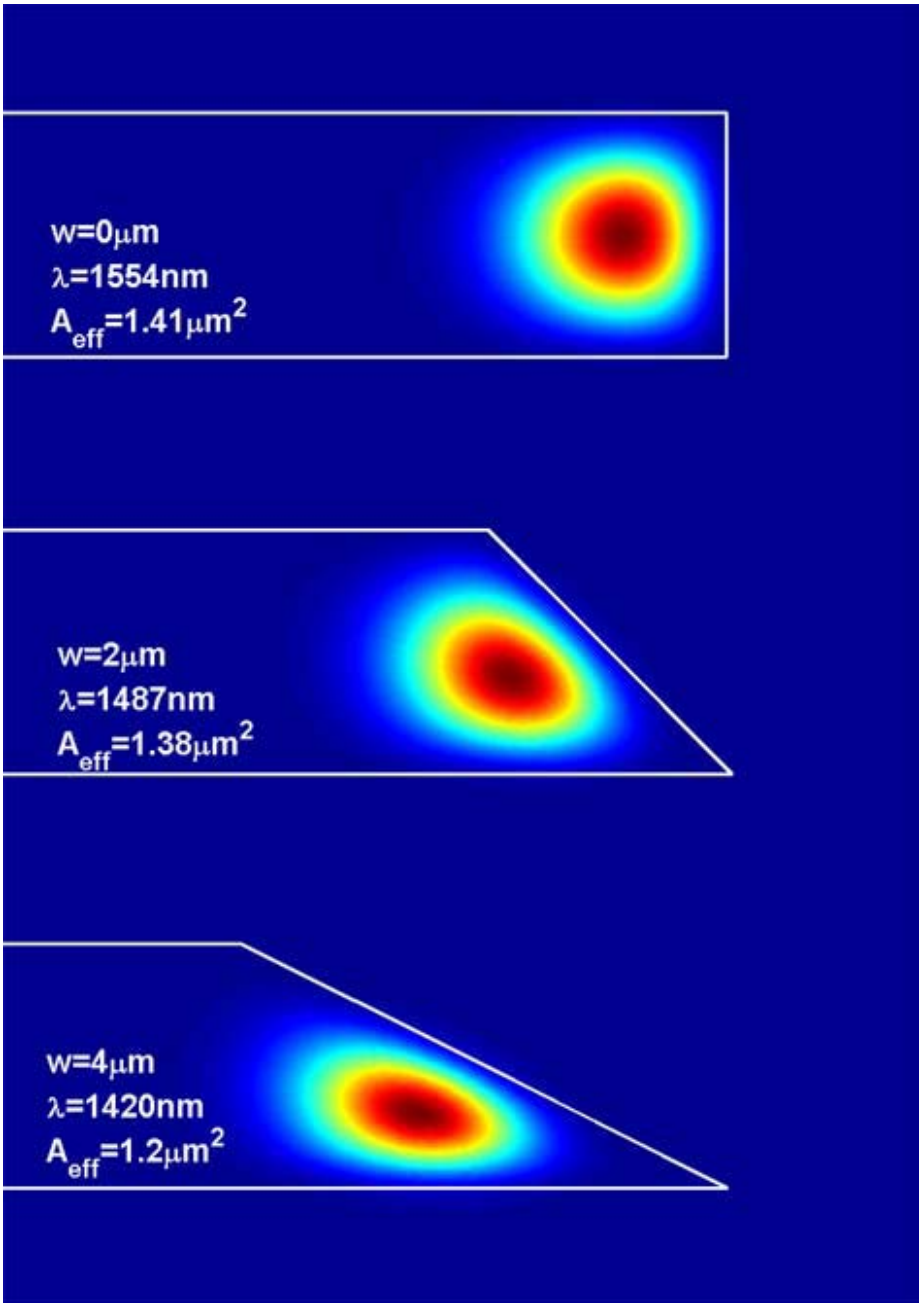

Figure 8.3: Modal isolation in microdisk cavities. The graph shows the numerically calculated intensity distribution $|E_\phi|^2$ for a fundamental disk mode (TM-polarization). In the simulation the principal disk diameter was 50 μm and the inner diameter is given by $(D - 2w)$. The simulation shows the decrease in the effective radius for the mode (as evidenced from a shift of the center of the intensity distribution), as a function of the wedge parameter (w).

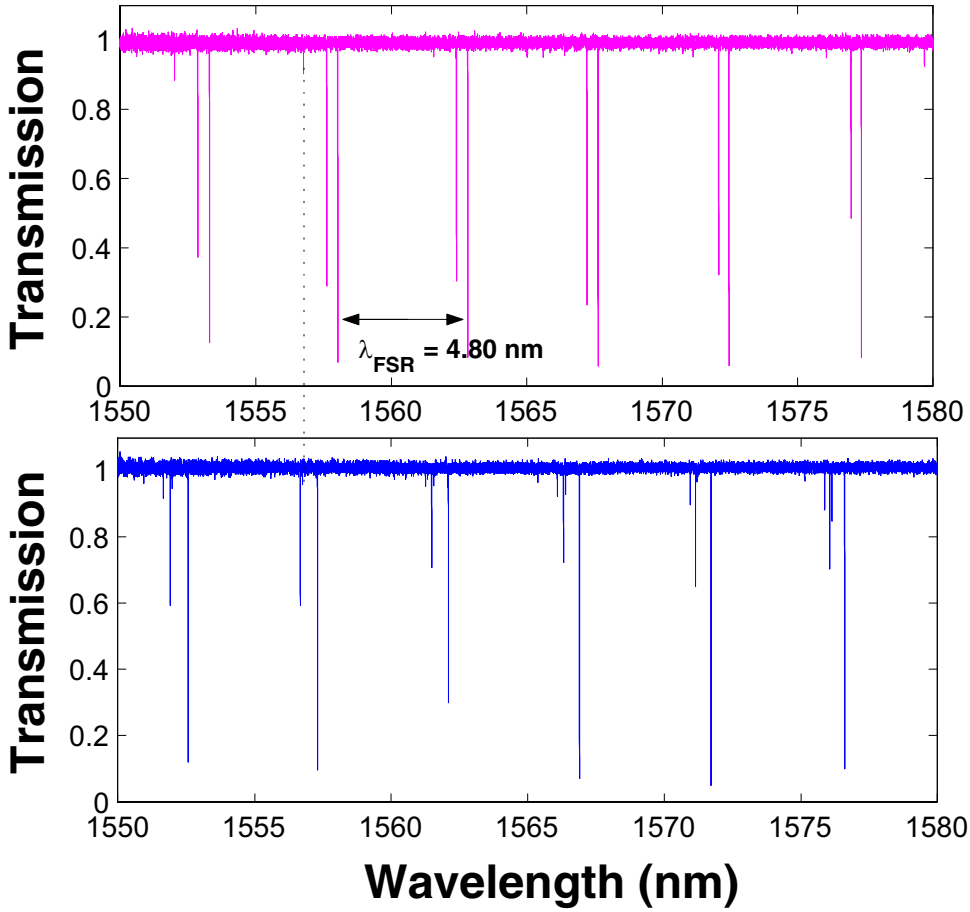

Figure 8.4: Mode spectrum of a 114-μm diameter resonator for TE and TM polarizations.

low total Q. In a symmetric add/drop device, efficient channel dropping requires that the total Q factor of the resonator is primarily induced by loading. If this is not the case, then parasitic cavity loss will induce an excessive loss penalty upon channel drop as well as an extinction-ratio penalty. For example, consider the ratio of power dropped versus incoming waveguide power, in a device consisting of two identical waveguides symmetrically coupled to a resonator. A simple analysis gives,

$$\frac{P_{dropped}}{P_{in}} = 1 - \frac{4 \cdot Q_0/Q_{ex}}{(1 + 2 \cdot Q_0/Q_{ex})^2} - \frac{1}{(1 + 2 \cdot Q_0/Q_{ex})^2} \tag{8.2}$$

Here, the first term constitutes a loss incurred because the resonator has a finite Q_0, and the second term is a loss resulting from residual transmission. As is evident from the expression, a high intrinsic-to-external Q ratio, will minimize insertion loss of the dropped signal by first reducing the impact of intrinsic resonator loss and second by biasing the input waveguide towards the optimal critical-coupling point, thereby coupling more power into the resonator. For asymmetrically-coupled waveguides, the finite channel transmission can be remedied by critically coupling the input waveguide to the resonator. The insertion loss of the dropped channel in this case is composed only of intrinsic resonator loss, which can be minimized using a large intrinsic Q.

$$\frac{P_{dropped}}{P_{in}} = 1 - \frac{1}{(1 + Q_0/Q_{ex})^2} \tag{8.3}$$

Using the highest Q values observed in this work and assuming a loaded Q of $2 \cdot 10^4$ (corresponding to a dropped bandwidth of 10 GHz) yields a channel extinction of 50 dB and a drop loss of 0.03 dB for a symmetrically configured add/drop filter. For comparison, an intrinsic Q factor of $2 \cdot 10^4$ yields an extinction of 9.5 dB and a drop loss of 3.5 dB.

8.5 Summary

In summary, high-Q silica resonators on a chip were fabricated. A combined wet etch and isotropic gas etch leaves undercut silica disks with a silicon support pillar. Without any further surface processing, quality factors in excess of 10^7 were measured. These high-Q values are attributed to *modal isolation* away from the disk edge that is induced by a wedge-shaped disk profile. High Q values can be used to create very low loss and high extinction add-drop filters, even in devices which operate at a substantially lower loaded Q value. In addition we have shown that tapered fibers enable efficient excitation of the disk modes as well as strong over-coupling with low, off-resonant insertion loss. Additional optical functionality in these structures can be added by means of implantation to obtain low threshold lasers.

Chapter 9

Ultra-low-threshold microcavity Raman laser on a chip

9.1 Abstract[1]

The ultra-high-Q optical modes in toroid microcavities, as well as the observed strongly reduced azimuthal mode spectrum, make toroid microcavities a promising candidate for nonlinear optical oscillators. In contrast to spheres, toroid microcavities are wafer-scale, and as such allow possible integration with other functionality. In this chapter the particular suitability of toroid microcavities as nonlinear Raman oscillators is shown, and the first Raman laser on a chip demonstrated. As in the case of microspheres, the long photon storage times in conjunction with the high ideality of a tapered optical fiber coupling junction[31], allows stimulated Raman lasing to be observed at ultra-low threshold (as low as 74 μW of fiber-launched power at 1550 nm). High efficiency (up to 45% at the critical coupling point) is obtained and in good agreement with theoretical modeling. In addition the emission is observed to be single mode over a large range of pump powers, which was not attainable in microspheres, due to the presence of nearly degenerate azimuthal modes. In addition, numerical modeling shows that the optical modes of toroid microcavities, possess a lower effective mode volume compared to microspheres. While the mode volume is readily calculated using numerical tools, it is experimentally difficult to access. In

[1] **Work in this chapter has appeared in "Ultra-low threshold microcavity Raman Laser on a microelectronic Chip", *Optics Letters*, Vol. 29, No. 11 (2004).**

this chapter a technique is presented, which uses the minimum stimulated Raman threshold as a means to infer the mode volume. Using this method the mode volume of toroid microcavities with small cross sectional areas is retrieved, and the observed threshold reduction is in qualitative agreement with numerical modeling.

9.2 Stimulated Raman scattering in toroid microcavities

In chapter 5, the long photon storage times and small mode volume of ultra-high-Q spherical microcavities were shown to allow significant reduction of the necessary threshold for stimulated Raman scattering[63]. However, microsphere properties such as their size and shape are not easily controlled during fabrication, nor are they readily integrable with other optical devices or electronics. In addition the microsphere Raman lasers were observed to emit inherently multi-mode, due to the presence of nearly degenerate azimuthal modes.

In this chapter the first demonstration of a chip-based (monolithic) single-mode micro-cavity Raman laser is presented, using ultra-high-Q toroid microcavities[33]. Toroid microcavities are excellent candidates for nonlinear oscillation based on Raman gain, as they exhibit microwatt-level stimulated Raman thresholds and high-pump-to-Raman conversion efficiencies (up to 45% observed). In comparison to Raman oscillation in microspheres[63], these devices, oscillate single mode over a wide range of pump powers, due to their reduced azimuthal degree of freedom. The latter also leads to a reduced mode volume, of the WGM modes taking part in the nonlinear process, and lead to an lower effective Raman oscillation thresholds compared to a spherical microcavity.

The fabrication of wafer-based toroid microcavities is described in appendix C, and uses a combination of conventional silicon micro-fabrication techniques and a CO_2 laser assisted re-flow process, and is described in detail in reference [33]. The re-flow process creates an exceptionally smooth dielectric interface and enables ultra-

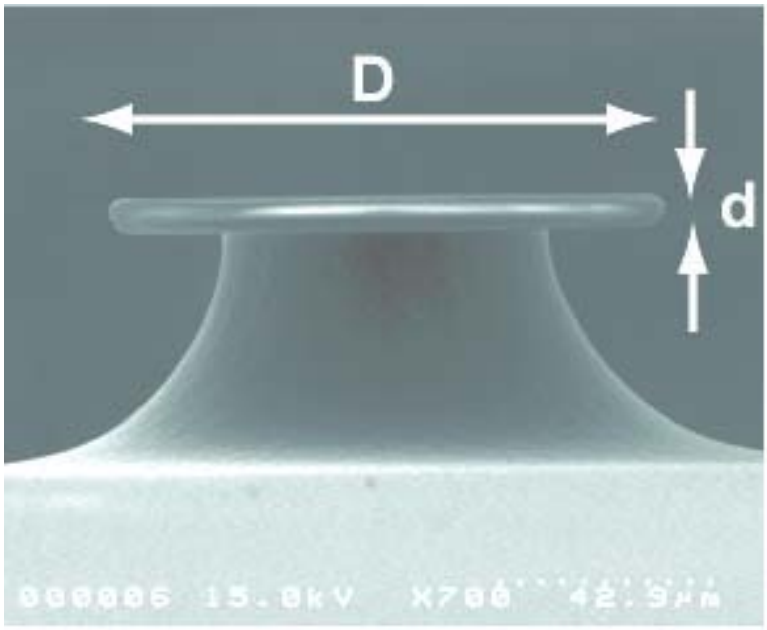

Figure 9.1: SEM side profile of a toroid microcavity showing the principal (D) and minor(d) toroid diameters.

high Q factors in excess of 100 million, as has been demonstrated in chapter 7. Figure 9.1 shows a scanning electron micrograph of a toroid microcavity and it's geometry parameters.

Figure 9.2 shows a typical Raman emission spectrum for a critically coupled microtoroid WGM pumped above Raman threshold. The pump wavelength is located at 1550 nm and the Raman emission is present in the 1650-nm band, down-shifted by approximately 12.5 THz relative to the pump mode, cavity-detuned from the peak Raman gain in silica, which occurs at 14 THz [87]. It is significant to note that the emission was observed to be *single mode*. Single mode operation was generally observed over a large range of pump powers and, in contrast to microspheres, is a result of the strongly reduced azimuthal degrees of freedom within the toroidal cavity, as has been investigated in chapter 7. This single mode behavior constitutes a significant improvement with respect to prior work on micro-spheres[63] or micro-droplets[56], which exhibit multi-mode oscillation spectra due to the presence of numerous nearly-degenerate azimuthal modes (as has been discussed in chapter 5 in the context of

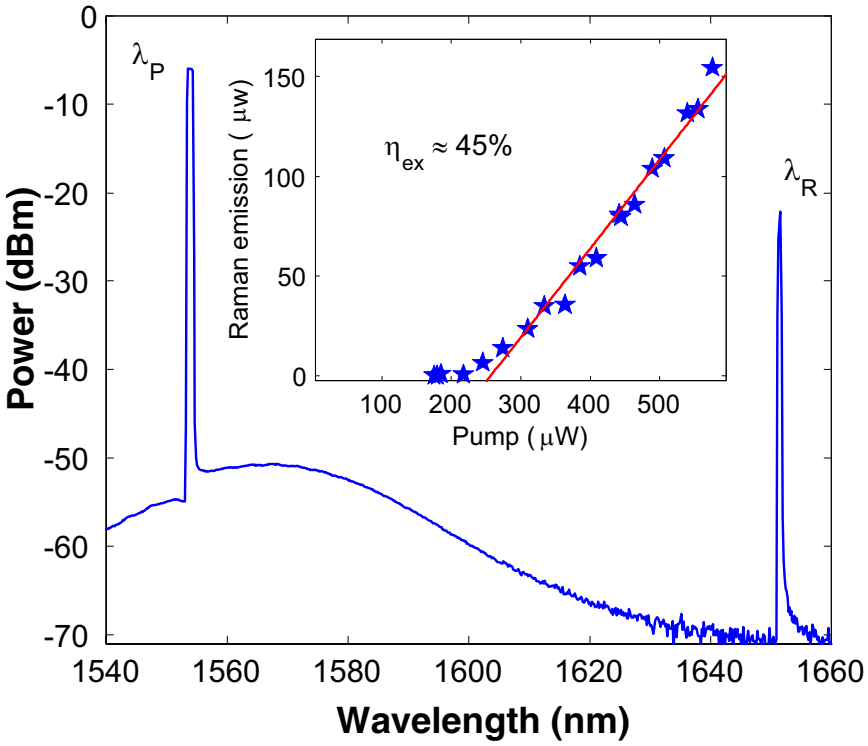

Figure 9.2: Raman emission spectrum of a toroid microcavity showing single mode oscillation. The pump is located at 1550 nm and the Raman emission is 12.5 THz shifted into the 1650 nm band. Inset: Bidirectional Raman emission as a function of pump power for a 58-μm-diameter toroid microcavity (Q_0=0.6×10^8) at the critical point. The threshold is ca. 250 μ-Watts and the bidirectional conversion efficiency is ca. 45%.

Raman lasing in microspheres).

The dependence of the Raman emission as a function of pump power for a critically-coupled microtoroid is given in the inset of figure 9.2 and displays a clear threshold behavior. The maximum Raman output power for this micro-toroid was more than 150 μW (bidirectional) and the measured pump-to-Raman differential conversion efficiency was 45 %. This number is close to the theoretically expected launched-pump-to-Raman differential conversion efficiency in the absence of any parasitic losses, which is ~47% at the critical point, as given by:

$$\eta_{ex} \equiv \frac{dP_{Raman}}{dP_p} = 2\frac{\lambda_p}{\lambda_R}\left(1+\frac{1}{K}\right)^{-2}$$

As experimentally and theoretically shown in chapters 5 and 6, the pump threshold for stimulated Raman scattering depends linearly on the effective mode volume V_{eff}. Due to the different cavity geometry of toroid microcavities, and the reduced azimuthal confinement, a lower threshold operation in a toroidal geometry is expected. In this chapter the extent of mode volume reduction is quantified using numerical modeling. These results are then compared to experimentally measured mode volume, which has been achieved by means of using the stimulated Raman threshold as a probe of mode volume.

9.3 Numerical modeling of the effective mode volume

To calculate the effective mode area (or volume) of toroid microcavities, the toroidal WGM were solved using the scalar wave equation approximation (In appendix B the details of the numerical modeling are given). In the case of a third order nonlinear process such as stimulated Raman scattering, the gain coefficient is linearly dependent upon the intensity of the pump field ($g_{NL} \propto I_p$), and the gain will only occur in a region close to the peak intensity. This fact is taken into account in the threshold equation by the effective mode volume[88][65]:

$$V_{eff} = \left(\frac{\int_V |E_p|^2 \, dV \int_V |E_R|^2 \, dV}{\int_{Vc} |E_p|^2 \, |E_R|^2 \, dV} \right) \approx \frac{\left(\int_V |E_p|^2 \, dV \right)^2}{\int_{Vc} |E_p|^4 \, dV} \tag{9.1}$$

The integral in the denominator is taken only over the extent of the dielectric cavity volume (which contributes to the nonlinear gain), whereas the integral in the numerator is taken over the entire volume. The effective mode volume, as will be seen in this section V_{eff}, differs in definition and value from the previously introduced energy related definition $V_m = \frac{\int \varepsilon(r) \left| \vec{E} \right|^2 dV}{\max(\varepsilon(r) \left| \vec{E} \right|^2)}$, which assumes a rectangular profile at peak intensity. Figure 10.2 shows the mode volume as well as the effective mode volume for a fundamental TM-mode of a $25 - \mu m-$diameter toroid microcavity with varying minor diameter. The numerical modeling shows that the effective mode volume for high aspect ratio D/d is approximately a factor of two larger than the (energy related definition) of mode volume V_m (eqs. 2.16). This is due to the fact that the definition V_m overestimates the gain for an intensity dependent process such as Raman scattering or parametric oscillation, as only regions of high field intensity contribute significantly to the Raman gain (and consequently lead to a lower effective intensity and correspondingly higher effective mode volume).

A reduction of the toroidal cross section causes the effective mode area to decrease as a function of toroid minor diameter (d). A comparison of the mode area (mode-volume) and effective mode area (volume) is shown in the inset. In the weak compression regime the toroidal cross section does equally reduce mode volume and effective mode volume, and the ratio remains unchanged (ca. $V_{eff} = 2 \times V_m$). In the case of strong modal compression, the effective mode volume reduces faster than the mode volume, which decreases the Raman oscillation threshold. Figure 9.5 shows the effective mode volume as a function of toroid cross sectional diameter (from 1-10 μm) for three different principal diameters($D = 25, 50, 75 \ \mu m$). It is furthermore interesting to note, that the mode volume of higher order azimuthal modes are also significantly reduced. In fact, the difference of fundamental to higher order mode (which in a microsphere is ca. 30%) reduces, as the toroid minor diameter is decreased. This behavior is shown in figure 9.6.

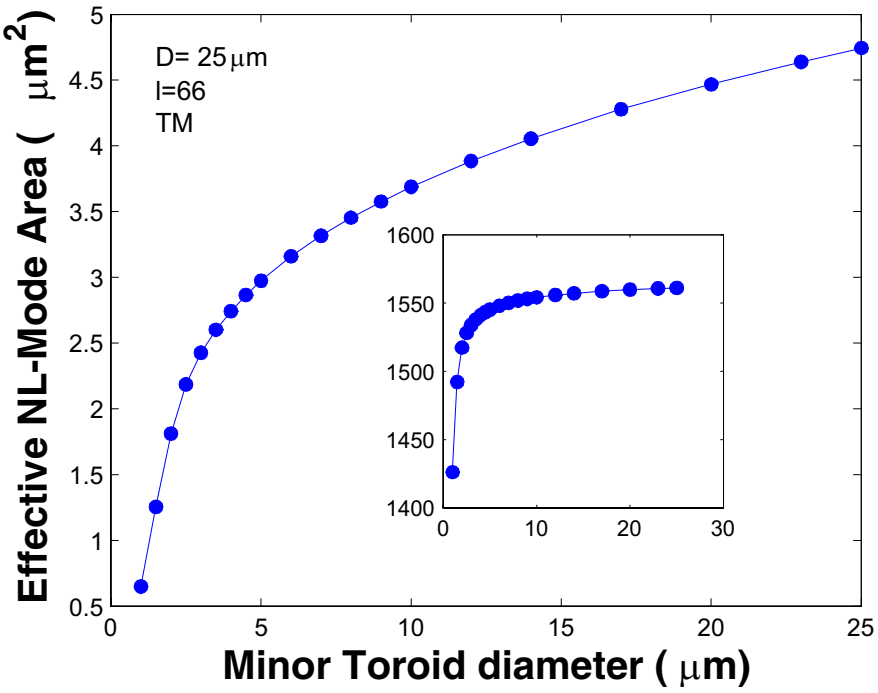

Figure 9.3: The effective mode area of for a TM-WGM of a toroid microcavity as a function of toroid diameter (d). The inset shows the resonance wavelength as a function of minor diameter.

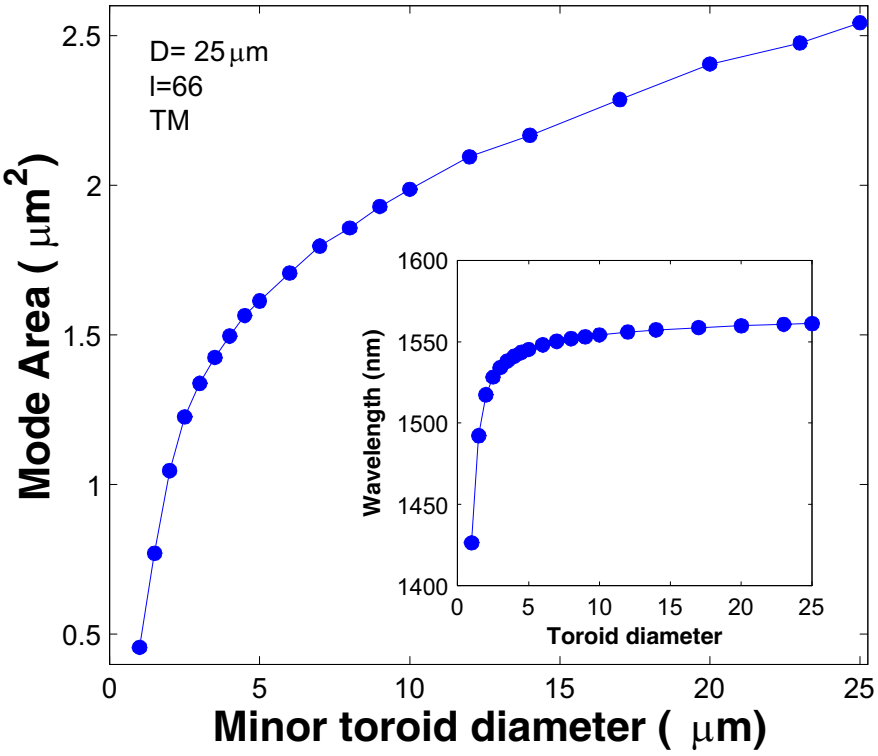

Figure 9.4: The mode area A_m of a toroid microcavity as a function of toroid diameter. Comparison with figure 9.3 shows that the effective mode volume (V_{eff}) is twice as large as the volume (V_m) .

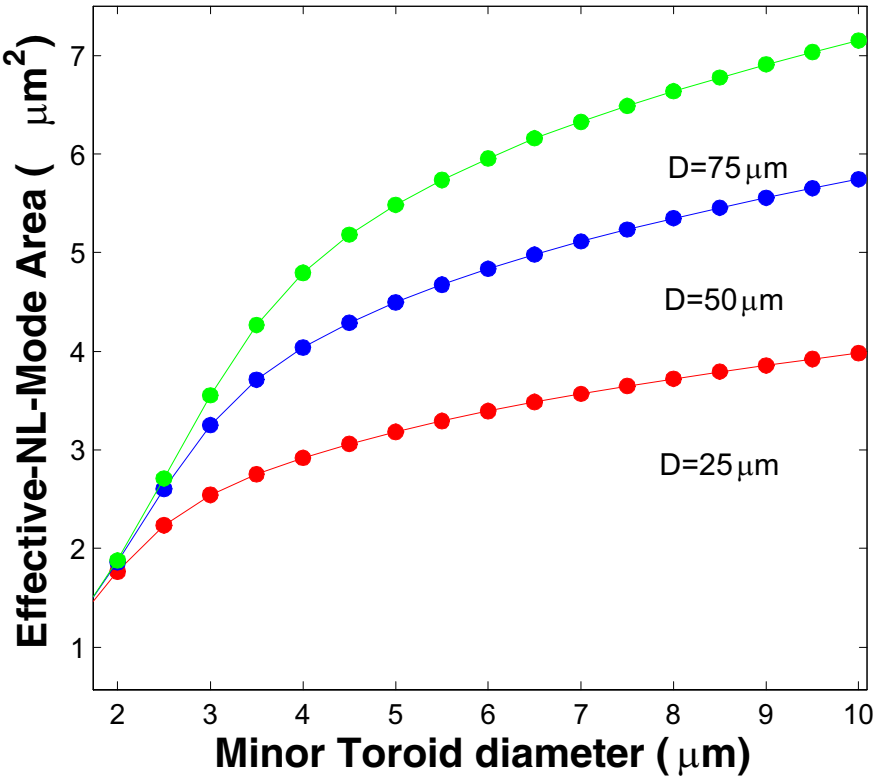

Figure 9.5: Effective mode area A_{eff} for a toroid microcavity as a function of minor toroid diameter (d), for three different principal diameters $(25, 50, 75\mu m)$.The resonance wavelength in this simulation was adjusted to the 1550 nm band.

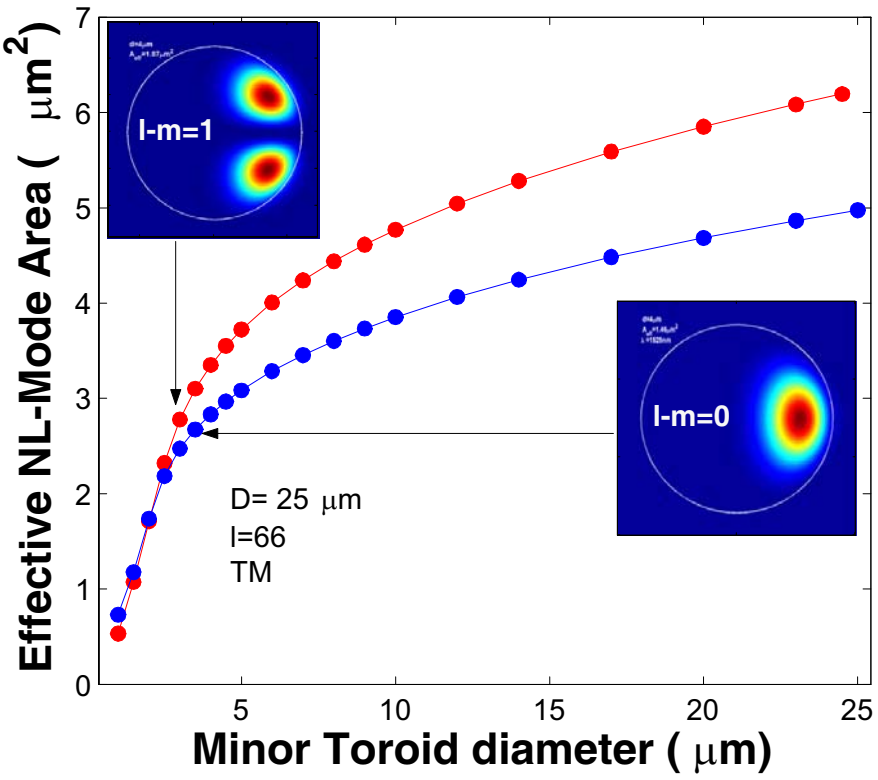

Figure 9.6: Effective mode volume of a $|\ell| = |m|$ and $|m| = |\ell - 1|$ toroidal whispering gallery mode. As evident from the simulation, the difference in mode volume between higher order azimuthal modes decreases as the toroidal cross sectional diameter is reduced.

9.4 Measurement of effective mode volume via Raman scattering

Since the mode volume of the toroidal WGMs is expected to be reduced as the minor diameter is reduced for D fixed (see figures 9.5 and 9.3), lower threshold operation is expected in a microtoroid when compared to the case of a micro-sphere having diameter D and comparable Q. Conversely, measurement of the Raman threshold allows the mode volume to be inferred via inversion eqs. 6.7:

$$V_{eff} = \frac{4}{27} (Q_0)^2 \frac{g_R \lambda_p \lambda_R}{C(\Gamma)\pi^2 n^2} P_t^{\min} \tag{9.2}$$

This method is used below to both infer the toroid mode volume with varying minor diameter as well as to compare the mode volume of toroids and spheres having equivalent principal diameters. For this study, toroid micro-cavities were fabricated with an approximately constant principal diameter (D) of 55 μm and varying minor diameters (d) from 3.7 to ~10 μm. The quality factors were measured by cavity ring-down, as used in ref. [63], and had values in the range of 100 million (ca.,~80 ns) for all the samples used in the Raman study. The observed Raman thresholds varied in the range of 74 μW to 250 μW. To compare the threshold among different cavity geometries, the threshold formula was normalized to take into account the different resonator characteristics, leaving only the modal volume dependence. The experimental protocol proceeded by determining the loaded Q factor and the modal coupling parameter Γ. To correct for variation of the Raman gain coefficient g(λ_R,λ_p), both the pump λ_p and Raman emission wavelength λ_R were also measured. Subsequently, scanning electron microscopy was used to record the side profile of the micro-cavities to determine the effective toroid minor diameter (d). Mode volume was then retrieved from the minimum Raman threshold measurement by eqs. 9.2.

Figure 9.7 presents the experimental results of this procedure and plots the mode volume of the toroid inferred from the measurement process. For comparison, the solid (dashed) line is the theoretically expected volume dependence based on a calcu-

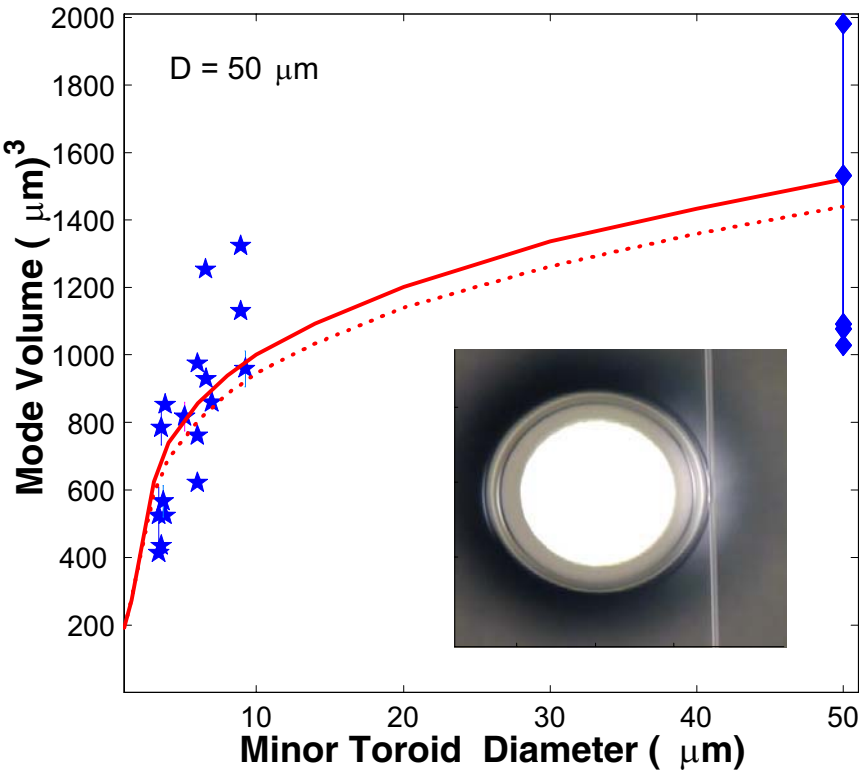

Figure 9.7: Main figure: Experimental and theoretical mode volume (in cubic-microns) of toroid microcavities as a function of the toroid minor diameter (d) for fixed principal diameter D (D= 50 microns). The case d=D (unity aspect ratio)corresponds to a microsphere, and the data shown for this case is taken from ref [89] for comparison. The solid and dotted lines refer to the mode volume of a fundamental toroidal WGM (TM and TE case respectively) obtained by numerical modeling. Inset: An optical micrograph of a ca. 80-micron-diameter toroid microcavity coupled to a tapered optical fiber.

lation of the TM (TE) fundamental mode volume for a 50-μm-diameter microtoroid. Despite experimental uncertainty due to the inability to measure ring-down in the 1600 nm band, the measured volume dependence is in qualitative agreement with the calculation. The lowest observed threshold in this measurement occurred for the smallest toroidal minor diameter ($D = 61\ \mu m, d = 3.7\ \mu m, \Gamma = 1.3$, $Q_0 = 1.0 \times 10^8$ with P=74 μW) in agreement with the Raman threshold formula). Also, for comparison purposes, data obtained from a previous study[89] using silica microspheres having a comparable diameter (case of $d = D$) are included in the plot.

9.5 Summary

In summary the first Raman laser on a chip is demonstrated. Compared to microspheres, these microcavity oscillators allow integration with other optical and electrical functionality. In addition to their practical advantages, the emission properties are highly advantageous, and single mode emission was observed over a large range of pump powers, owing to the strongly reduced azimuthal mode spectrum. The strong azimuthal confinement also leads to a reduced mode volume and effective mode volume of toroid vs. spherical microcavities. To compare and infer the mode volume, a measurement of effective mode volume is presented using the minimum Raman threshold as a probe. The results indeed confirm the reduced mode volume of toroid microcavities, and are in qualitative agreement with the numerical modeling.

Chapter 10

Kerr-nonlinearity optical parametric oscillation in an ultra-high-Q toroid microcavity

10.1 Abstract[1]

Kerr-nonlinearity induced optical parametric oscillation in a microcavity is reported for the first time. Geometrical control of recently developed toroid micro-cavities enables a transition from stimulated to optical parametric oscillation regimes. Optical parametric oscillation is observed at record low threshold levels (174 micro-Watts of launched power) more than two orders of magnitude lower than for optical-fiber-based OPOs. In addition to their microscopic size (typically tens of microns), these oscillators are wafer-based, exhibit high conversion efficiency (36 %) and are operating in a highly ideal "two photon" emission regime, with near-unity (0.97±0.03) idler-to-signal ratio.

10.2 Introduction

Optical parametric oscillators (OPOs) rely on energy and momentum conserving optical processes to generate light at new “signal” and “idler” frequencies. In contrast to oscillation based on stimulated gain, optical parametric oscillation does not involve

[1] **This chapter has been submitted to *Physical Review Letters* (2004)**

coupling to a dissipative reservoir. The lack of such dissipation makes them uniquely suited for fundamental studies, such as the generation of non-classical states[90][91] for quantum information research[92][2] as well as in numerous applied areas (e.g. photonics, spectroscopy, sensing). However, oscillation based on optical parametric gain requires stringent phase matching of the involved optical fields[93]. This combined with the necessity of high field intensity or long interaction length poses severe challenges to attaining micro-cavity optical parametric oscillators. In fact, whereas micro-cavity stimulated nonlinear oscillators have been demonstrated[60, 70, 56, 94, 63, 95], optical parametric equivalents have not been demonstrated so far.

Here we report Kerr-nonlinearity induced optical parametric oscillation in a toroidal microcavity. Toroid micro-cavities are silica-based whispering-gallery-type resonators possessing ultra-high Q-factors[33]. Efficient coupling, with high ideality[63] is a achieved using tapered optical fibers as coupling elements. While ultra-high-Q ensures high circulating field intensities within the resonator[61], causing a variety of nonlinear optical effects[70, 62, 94, 56, 60], it is not a sufficient condition to ensure parametric oscillation. Due to inversion symmetry, the lowest order nonlinearity in silica is the third order nonlinearity so that the elemental parametric interaction converts two pump photons (ω_p) into signal (ω_S) and idler (ω_I) photons[93, 91]. In order for parametric oscillations to efficiently occur, both energy and momentum must be conserved in this process[88, 93]. In whispering-gallery-type resonators, such as microtoroids, momentum is intrinsically conserved when signal and idler angular mode numbers are symmetrically located with respect to the pump mode (i.e. $l_{S,I} = l_p \pm N$

[2]Due to parametric conversion process, the signal and idler photons are generated in pairs at the same instant in time. The simultaneous generation of photon pairs, leads to two beams which are highly correlated. In particular, the individually generated beams exhibit noise above the shot-noise-limit (SNL). However if the noise produced by both beams is subtracted it can fall below the shot-noise limit, a situation which is commonly referred to as two-mode squeezing. Part of the correlations is however lost due the presence of the cavity, which randomizes the photon escape times. The correlations will thus only persist for correlation times exceeding the cavity lifetime. A simple model leads to the noise spectrum at frequency Ω :

$$S(\Omega) = S_{SNL}(\Omega) \cdot \left(1 - \frac{\epsilon}{1 + \Omega^2(\tau_0^{-1} + \tau_{ex}^{-1})^{-2}}\right)$$

Here ϵ is the probability that the photon is detected, and τ is the cavity lifetime. In the present case, the cavity lifetime is given by $\tau_0^{-1} + \tau_{ex}^{-1}$.

)[3].

$$\begin{aligned} 2\beta_m &= \beta_{m+N} + \beta_{m-N} \\ 2\frac{m}{R_0} &= \frac{m-N}{R_0} + \frac{m+N}{R_0} \end{aligned}$$

Energy conservation ($2\hbar\omega_p = \hbar\omega_S + \hbar\omega_I$), on the other hand, is not expected to be satisfied a priori, since the resonant frequencies are, in general, irregularly spaced due to both cavity and material dispersion. As a result, the parametric gain is a function of the frequency detuning,

$$\Delta\omega = 2\omega_p - \omega_S - \omega_I$$

which effectively gives the degree to which the interaction violates strict energy conservation. In the case of silica, the material dispersion of silica in the 1500 nm band $\left(\frac{dn}{d\lambda} < 0\right)$ leads to a positive detuning frequency. It can be shown that the existence of parametric gain requires that this detuning be less than the parametric gain bandwidth[88] $\Omega = 4\frac{c}{n}\gamma P$ ($\gamma = \frac{\omega}{c}\frac{n_2}{A_{eff}}$) where $n_2 \approx 2.2 \times 10^{-20}\frac{m^2}{W}$ is the Kerr nonlinearity for silica [93] and P is the circulating power within the micro-cavity. The effective nonlinearity γ depends on inversely on the effective cross section of the mode[4]. By equating parametric gain and micro-cavity loss (as determined by loaded Q factor), the threshold pump power necessary in the waveguide is obtained for parametric oscillation.

$$P_t^{Kerr} = \frac{\omega_0^2 Q_0^{-2}\left(1+K\right)^2 + (\Delta\omega/2)^2}{2\gamma\Delta\omega\left(c/n_{eff}\right)} \cdot \frac{\pi^2 R n_{eff}}{C(\Gamma)\lambda_0}\frac{(K+1)^2}{Q_0 K}$$

Here $K \equiv Q_{ex}/Q_0$ characterizes the coupling of the resonator to a waveguide used for

[3] The propagation constanst is given by $\beta_\ell = \frac{m}{R}$, where R is the cavity radius.

[4] As shown in the appendix, the effective cross section for a third order nonlinear process, is given by: $A_{eff}^{-1} = \frac{\int \left(E_i\right)^* \left(E_j\right)^* E_k E_l \, dA}{\left(\int |E_i|^2 dA \int |E_j|^2 dA \int |E_k|^2 dA \int |E_l|^2 dA\right)^{1/2}}$, where E is the electric field distribution of the respective mode. As the angular mode numbers for signal, idler and pump are closely spaced, a good approximation is: $A_{eff}^{-1} \approx \frac{\int |E_p|^4 dA}{\int |E_p|^2 dA \int |E_p|^2 dA}$.

both pumping of the resonator as well as collection of oscillator power. This coupling is characterized as over-coupled ($K > 1$), critical ($K = 1$) and under-coupled ($K < 1$) using the standard definitions[96]. Q_0 and Q_{ex} are the intrinsic and the external (coupling related) quality factors, respectively. R is the principal cavity radius, n_{eff} is the effective index and $C(\Gamma)$ is a correction factor in the range of [1..2] taking into account the reduction of circulating power in the presence of modal coupling of the degenerate clockwise and counterclockwise "whispering gallery modes" (WGMs) [27]. Figure 1 shows both parametric and Raman oscillation regimes as a function of the detuning frequency $\Delta\omega$ and the coupling parameter K. The threshold pump power for parametric oscillation is color-coded as indicated.

As stimulated Raman scattering does not depend on the detuning frequency (i.e. it is intrinsically phase-matched), it is the dominant nonlinear mechanism by which light is generated for large detuning values. With decreasing $\Delta\omega$, a transition from stimulated to parametric regimes occurs when the threshold for parametric oscillation falls below that for Raman (The peak parametric gain is larger than the peak Raman gain, $g_{Kerr}^{\max} \approx 2 \cdot g_R^{\max}$[93]). Also note that for increased waveguide loading (and hence correspondingly higher threshold pump powers) the transition can be made to occur for detuning values that are progressively larger.

To bring about the condition $0 < \Delta\omega < \Omega$ a reduction of the toroidal cross-sectional area reduces the modal effective area A_{eff} and produces a two-fold benefit. First, it increases the parametric bandwidth Ω through its dependence on γ [88] and second, it reduces $\Delta\omega$. The latter occurs because of increased modal overlap with the surrounding dielectric medium (air) and hence flattening of the modal dispersion. Finally, numerical finite-element-modeling was used to calculate the dependence of A_{eff} on the toroid principal (D) and minor diameter (d). Figure 2 shows the he calculated modal area for a fundamental toroidal WGM as the dotted and solid lines (TE and TM polarization). Note that the case ($d = D$)corresponds to a spherical microcavity. Thus, the desired transition can be induced with toroidal geometries of high principal-to-minor toroid diameter (high aspect ratio), where the principal diameter (D) denotes the outer cavity diameter and the minor diameter (d) refers to

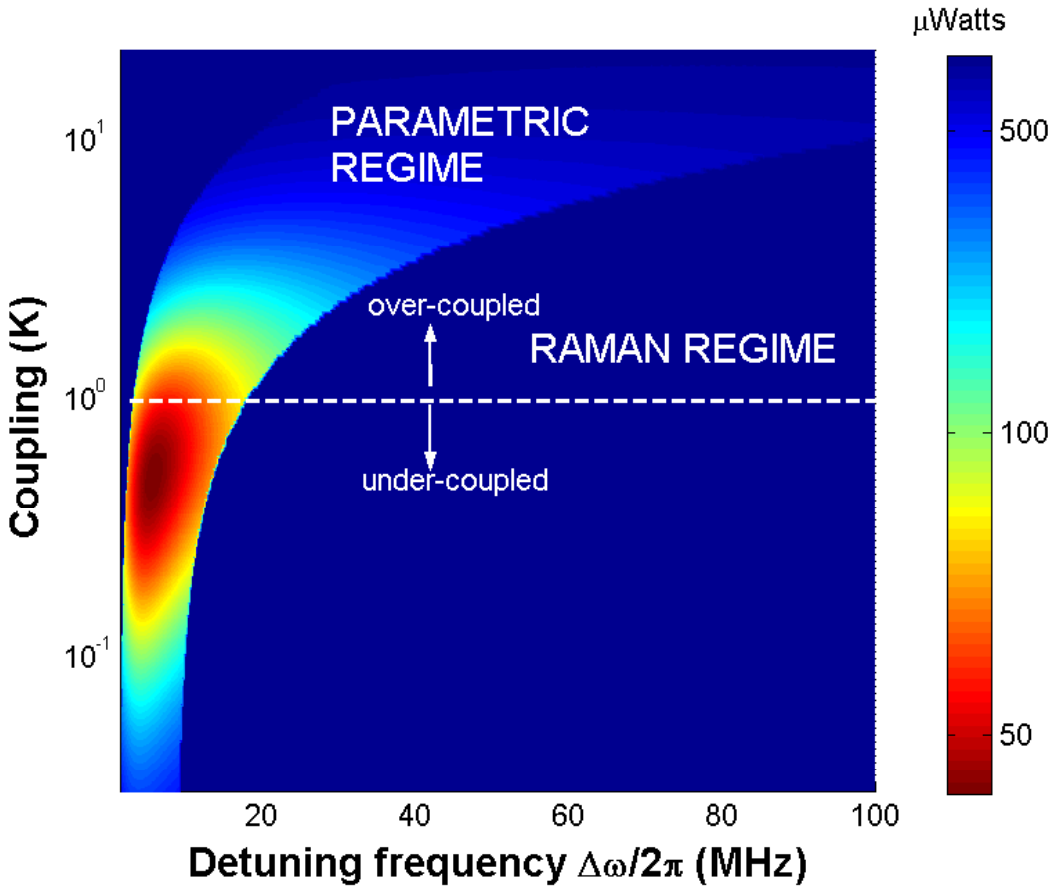

Figure 10.1: Nonlinear processes in a micro-cavity with $D = 50\mu m, d = 4\mu m$ and $Q_0 = 10^8$. The vertical axis denotes coupling strength K of the waveguide-resonator system while the horizontal axis denotes frequency detuning. The dotted line corresponds to the critical coupling point (defined by vanishing waveguide transmission [96, 75]). The dark blue colored part of the spectrum denotes areas where Raman oscillation occurs. The color-coded region corresponds to the parametric oscillation regime (where the parametric threshold is indicated by color in micro-Watts).

the smaller, toroid cross-sectional diameter.

In order to confirm this prediction, toroid micro-cavities with an approximately constant principal diameter (D) and varying minor diameter (d) in the range of 3.8-10 μm were fabricated. Due to the ultra-high-Q of the toroidal whispering-gallery modes (WGMs), ultra-low-threshold, stimulated Raman scattering was consistently observed for toroids having an aspect ratio of ca. $D/d < 15$[97].

For micro-toroids having an aspect ratio (D/d) in excess of ca. 15 a transition (and a subsequent quenching of Raman[66, 98]) to parametric oscillation was observed. Figure 3 shows a parametric oscillation emission spectra for a micro-toroid with d=3.9 μm, D=67 μm and $Q_0 = 0.5 \times 10^8$. In this measurement a single fundamental WGM of a micro-toroid is pumped in the telecommunication window near 1550-nm using tapered optical fiber waveguides[99, 75]. Phase-matching of taper mode and WGM was achieved by varying the taper waist in the coupling region. In this way high ideality of the coupling junction was achieved[31]. The parametric interaction in the micro-cavity causes emission of co-propagating signal and idler modes, which are coupled into the forward direction of the tapered fiber. Some residual signal and idler reflection was detected in the backward direction due to the presence of modal coupling[27], induced by backscattering[5]. The generated signal and idler modes had identical oscillation threshold, within the experimental resolution set primarily by taper coupling variations ($ca. \pm 5\%$).

Figure 4 shows the parametric oscillation threshold as a function of taper-toroid coupling gap for the toroid micro-cavity of figure 3. Analysis of the threshold equation shows that the coupling point of minimum threshold is a function of the detuning frequency. At the optimum frequency detuning (i.e. maximum parametric gain, for $\Delta\omega_{opt} = 3 \cdot \frac{\omega}{Q_0}$), the minimum threshold occurs under-coupled for $K_{\min} = 0.5$ with

[5]The presence of modal coupling randomizes the escape direction of the generated signal and idler photons. If the reflected radiation is not measured, and the remaining part of the detection scheme is ideal, the detection probability is given by:

$$\epsilon = (1 - R(\Gamma_s))(1 - R(\Gamma_i))$$

Therefore the presence of modal coupling decreases the possible noise reduction, unless the reflection is included into the measurement scheme.

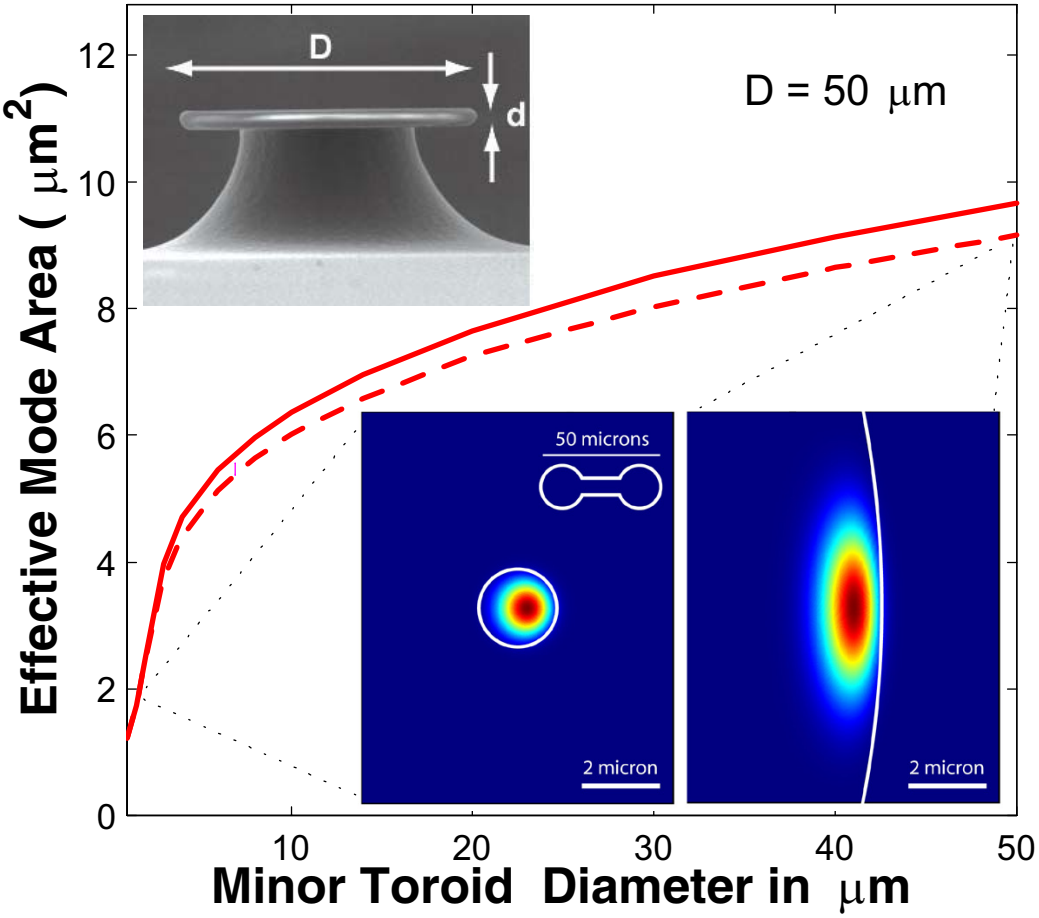

Figure 10.2: Calculated WGM mode area as a function of minor toroid diameter (for a fixed principal diameter $D = 50\mu m$). The solid and dotted lines are the mode area obtained from finite-element modeling of the fundamental toroidal WGM (dotted line: TE polarization, solid line: TM polarization) at a wavelength of 1550 nm. For comparison the inset shows modeled field intensity plots of a fundamental micro-sphere WGM (right panel) and a toroid WGM of equal principal diameter and $d = 2\mu m$ (left panel). Upper inset: Scanning-electron-micrograph of a toroid microcavity with the geometry parameters indicated.

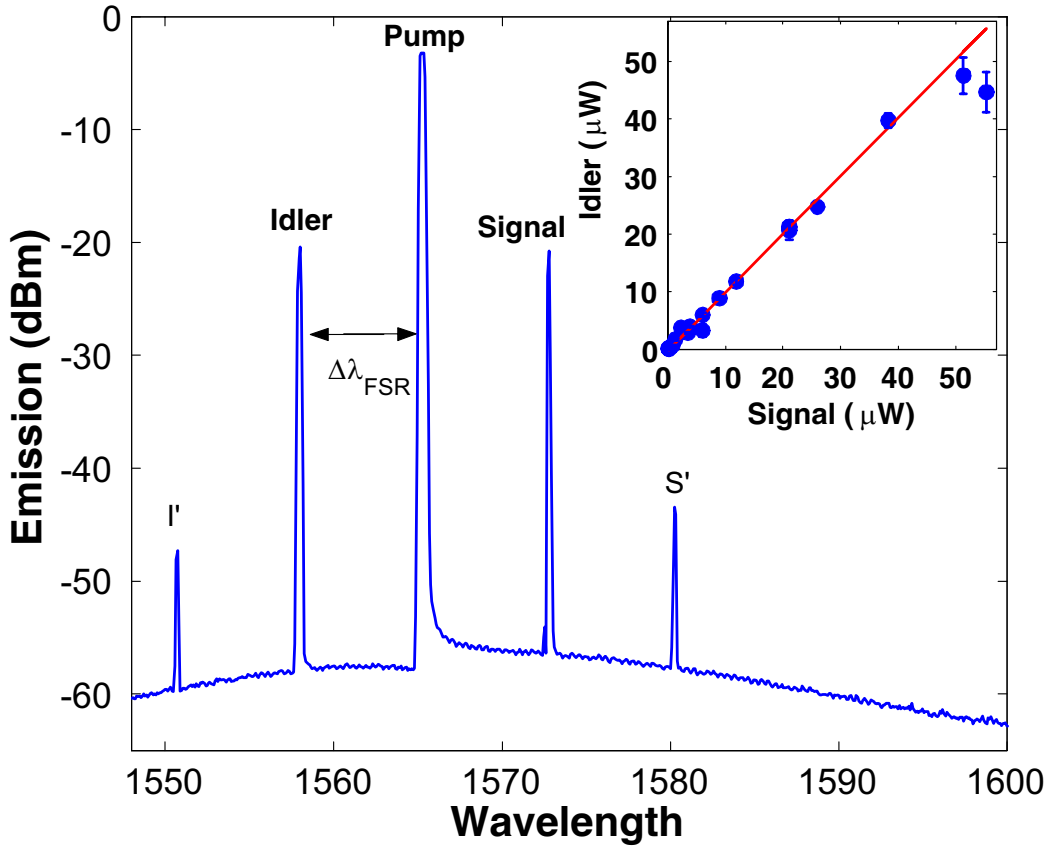

Figure 10.3: Parametric-oscillation spectrum measured for a 67-μm-diameter toroidal micro-cavity. The pump is located at 1565 nm and power levels are far above threshold. The signal and idler are modes with successive angular mode numbers and are spaced by twice the free spectral range (2×7.6 nm). The subsidiary peaks (denoted I',S') only appeared at high pump powers and are due to a combination of nonlinear effects, such as parametric oscillation (of signal and idler) as well as four-wave-mixing involving the idler, pump and signal. Inset: idler emission power plotted versus the signal emission power, recorded for different pump powers. The idler-to-signal power ratio is 0.97 ± 0.03. For higher pump powers deviation is observed due to appearance of secondary oscillation peaks (I',S') (compare main figure).

finite pump transmission ($T_{\min} = 1/9$), whereas for larger detuning the minimum threshold point shifts towards being over-coupled (compare figure 1). The measured minimum threshold in the present case was 339 micro Watts and occurred for the taper displaced by 0.04 microns into the under-coupled regime. The corresponding pump transmission was $T \approx 4\%$ ($K \approx 0.7$), indicating that the frequency detuning is close to being optimum. Above threshold the signal and idler fields increase approximately linearly with pump power (for high pump power P, the emission scales $P_{S,I} \propto \sqrt{\frac{P}{P_t} - 1}$). The inset of figure 3 shows a pump-to-idler conversion characteristic at the point of minimum threshold.

The corresponding differential conversion efficiency was 17% pump-to-idler (The total differential conversion efficiency of pump to both signal and idler fields was 34%). Comparison of the differential conversion efficiency to theory $\eta = 2 \cdot (1 + K^{-1})^{-2}$ is consistent with the minimum threshold occurring under-coupled, as the inferred coupling point is $K = 0.7$ (corresponding to $T = 4\%$ in agreement with the above measured value). Using the minimum threshold data and the cavity ringdown measurements a detuning frequency of $\Delta\omega/2\pi \approx 24\ MHz$ is inferred from the threshold equation, compared with $\Delta\omega_{opt}/2\pi = 11.6\ MHz$ for optimum detuning frequency at the measured Q value. The lowest measured parametric oscillation threshold for the micro-toroids in this study was 170 micro-Watts of launched power in the fiber (for a micro-cavity with $D/d = 16$, $d = 4\mu m$, $Q_0 = 1.25 \times 10^8$ and $\Delta\omega/2\pi \approx 18\ MHz$) and is a factor of 200 lower than for fiber OPOs[100] that utilize the dispersion control provided by photonic crystal fiber [101]. As a further confirmation that parametric oscillation is present, both signal and idler emission were recorded for varying pump power. From theory a signal-to-idler photon creation ratio of unity is expected for parametric oscillation[93]. The inset of figure 4 shows the measured idler emission power plotted versus signal emission power through the optical fiber taper. The recorded data was corrected for modal coupling[27] by measuring the reflected power for all three resonances at the critical point. After correcting for modal coupling the ratio of idler conversion to signal conversion was 0.97 ± 0.03. The observation of near-unity idler-signal emission-power ratio, along with the identical

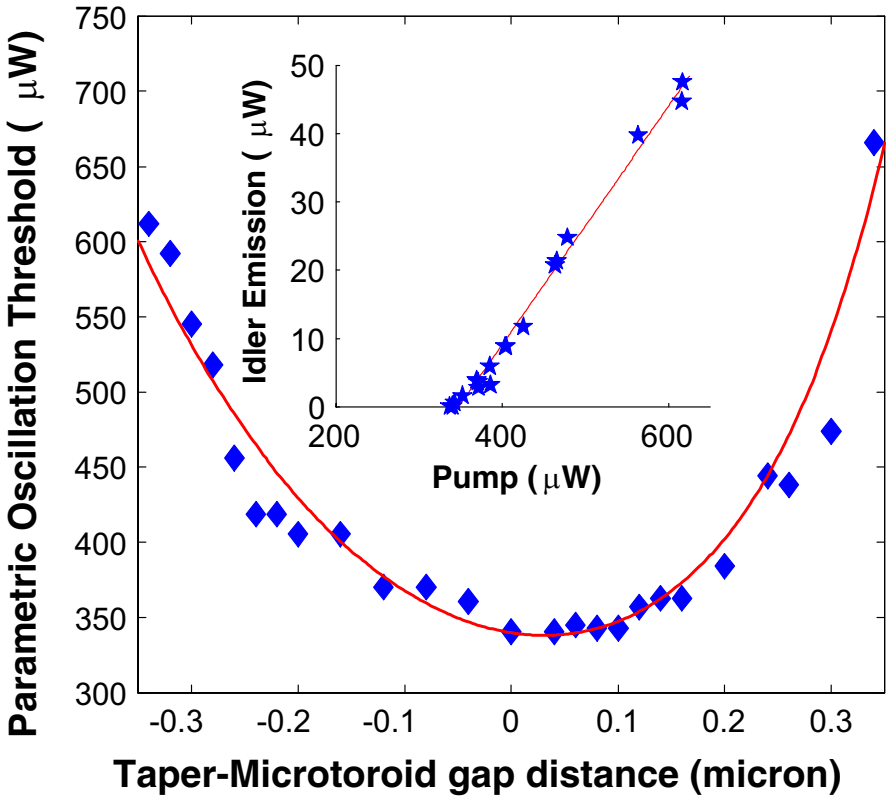

Figure 10.4: The coupling-gap-dependence of the parametric threshold with respect to the critical coupling point measured using a 67-μm-diameter toroid microcavity. The minimum threshold occurs with the tapered optical fiber 0.04 μm under-coupled (with finite transmission of ca. 4%). The solid line is a theoretical fit using the threshold equation. Inset: Idler emission versus pump power. The differential conversion efficiency from pump-to-idler was 17%(and correspondingly 34% for pump to signal and idler).

threshold for signal and idler wave emission, demonstrates that the observed emission bands can solely be attributed to Kerr-induced micro-cavity parametric oscillation. Finally, stimulated Brillouin scattering (SBS), which involves coupling to a acoustic phonon, was not present, despite having a nearly 3 order of magnitude larger gain in comparison to the parametric gain. As noted previously, SBS is unlikely to occur in microcavities[63]. In particular as micro-toroids exhibit strongly reduced mode spectrum due to azimuthal confinement[33, 97], overlap with the gain bandwidth is SBS is unlikely.

10.3 Summary

We have thus observed for the first time (to the authors' knowledge) Kerr-nonlinearity induced optical parametric oscillation in a micro-cavity. Parametric interactions provide a distinct and important class of nonlinearity in both applied and fundamental areas, and as such this result should extend the range of micro-cavity applications into new fields. In addition to the highly advantageous practical aspects of on-chip micro-cavity nonlinear oscillators, (such as wafer-scale integration and control), these oscillators exhibit important properties due to the nature of the underlying nonlinear process within the micro-cavity. Specifically, a phase-sensitive amplification process that can exclude competing Brillouin or Raman processes, as demonstrated here, with a highly ideal coupling junction can provide an excellent candidate system for the generation of non-classical states of light[102, 103, 91, 90, 64, 104, 105, 106] in a micro-cavity. Whereas the work presented here has used the third order nonlinearity of silica itself, it should also be possible to induce second-order nonlinear interaction (such as parametric down-conversion), by using ultraviolet[107] or thermal-electric[108] glass poling techniques. This would be important in quantum information[92] and quantum optical studies[91, 109, 110, 111] as well as for novel bio-imaging schemes based on entanglement[112]. Moreover, the toroid micro-cavities exhibit high modal purity (single mode emission). This property and their nearly lossless coupling junction[31],

are important prerequisites for both applied and quantum optical studies.